TECHNISCHE UNIVERSITÄT WIEN
Vienna | Austria

Master Thesis

Design of a turbulent flow facility and development of an algorithm for PIV

carried out for the purpose of obtaining the degree of Master of Science (MSc), submitted at TU Wien, Faculty of Mechanical and Industrial Engineering, by

Ersah TOPAC

Mat.Nr.: 1129049

under the supervision of

Univ.Prof Dipl.-Ing. Dr. Alfredo Soldati

Institute of Fluid Mechanics and Heat Transfer, E322

reviewed by

Prof. Alfredo Soldati
Fluid Mechanics and Heat Transfer
Getreidemarkt 9, 1060 Vienna

Dr. Marco De Paoli
Fluid Mechanics and Heat Transfer
Getreidemarkt 9, 1060 Vienna

I confirm, that going to press of this thesis needs the confirmation of the examination commitee.

Affidavit

I declare in lieu of oath, that I wrote this thesis and performed the associated research myself, using only literature cited in this volume. If text passages from sources are used literally, they are marked as such.

I confirm that this work is original and has not been submitted elsewhere for any examination, nor is it currently under consideration for a thesis elsewhere.

Vienna, April, 2018 _____

Signature

Abstract

The applications and investigations of anisotropic particles in turbulent flows are very extensive in plenty of industrial and natural processes. Anisotropic particles can vary in shape or rigidity and they exhibit rich and complex behaviours in turbulence, which are not completely understood. Therefore, dynamics of particle laden turbulent flows are extensively investigated. The aim of this work is to design a test section to detect anisotropic particles inside a turbulent channel flow. The channel has to be long enough to obtain a fully developed turbulent flow. The measurement technique to be performed should not be intrusive in order not to influence the flow field. Particle Image Velocimetry (PIV) is a non-intrusive laser optical measurement technique for research and diagnostics into flow, turbulence, microfluidics, spray atomization and combustion processes. Main components of a PIV system are: a test section, a high speed laser, a camera, and a computer to analyse the images obtained from the camera. In this work, optimization of the main tools of a PIV system will be vastly explained and the accuracy of the methods will be crosschecked by reviewing the literature. The optimization procedures substantially contain identification of the thickness of the walls of the optically transparent test section, lens and camera configurations and synchronization between cameras and laser. Different PIV techniques to obtain 3-velocity components will be introduced, a comparison and a discussion will be done in order to choose the most suitable method for our case by considering their advantages and disadvantages. The algorithm to analyse PIV data will be described step by step and the fundamental codes for programming a PIV analyzing algorithm will be given. The performance evaluation of the algorithm will be done by the comparison with direct numerical simulation results. During the comparison different subpixel accuracy methods were considered. Finally, a protocol containing the rules for lab safety, experimental setup, calibration and optimization was given.

Acknowledgements

I would first like to thank my supervisor Prof. Alfredo Soldati and co-supervisor Dr. Marco De Paoli of the Institute of Fluid Mechanics and Heat Transfer at the Technical University of Vienna. Their doors were always open whenever I ran into a trouble spot or had a question about my research or writing. They consistently allowed this paper to be my own work, but steered me in the right the direction whenever they thought I needed it.

I would also like to acknowledge Mobin Alipour of the Institute of Fluid Mechanics and Heat Transfer at the Technical University of Vienna as the third reader of this thesis, and I am gratefully indebted to him for his very valuable comments on this thesis.

Finally, I must express my very profound gratitude to my parents and to my sister for providing me with unfailing support and continuous encouragement throughout my years of study and through the process of researching and writing this thesis. This accomplishment would not have been possible without them. Thank you.

Author

Ersah Topac

Contents

List of Figures

List of Tables

1. Introduction

Multiphase turbulent flows containing anisotropic particles are very widespread case in industrial applications and natural phenomena. Examples to some industrial applications can be listed as,

- pulp and papermaking (Lundell et al., 2011),
- pharmaceutical applications (Erni et al., 2009),
- soot emission from the incomplete combustion process of hydrocarbons (Moffet and Prather, 2009; Omidvarborna et al., 2015).

Some examples for natural phenomena are,

- pollen distribution in air (Sabban and van Hout, 2011),
- kinematic behaviors of ice clouds (Heymsfield, 1977),
- motions of microorganisms in oceans and rivers (Pedley and Kessler, 1992).

The reason of the shapes of diverse particles like ice crystals and soot may vary in specific formation processes, subjects like plankton and pollen in evolutionary selection processes, fibers utilized in textile industry and pulp making in design requirements (Voth and Soldati, 2017). The fibers can be categorized as spheroids with a grand aspect ratio, $\lambda > 1$. Spheres can be classified as, $\lambda = 1$, oblate spheroids or disks as, $\lambda < 1$. The aspect ratio is the ratio of the dimension along the symmetry axis to a perpendicular dimension.

The nature of the interactions between anisotropic particles and turbulent flows is a sophisticated phenomenon. Additional to the interactions between particles with a spherical shape and turbulent flows (Balachandar and Eaton, 2010), one must take account of the torques and forces which is related to the orientation of the particles. To identify a problem as a subject of non-spherical particles in turbulence accurately, it is essential to identify a broad number of factors such as the force and boundary conditions, viscosity and density of the fluid. They have effects on dimension, shape, density and concentration of the particles. In some cases additional parameters like translational and rotational diffusivity, influence of gravitation, deformation of particles, impacts between particles, accumulation or disjunction, non-Newtonian fluid behaviors, and electrostatic forces can also be significant. Some industrial processes frequently contain plenty of the parameters mentioned above all together (Voth and Soldati, 2017).

The fundamentals of particle-fluid interactions will be introduced in the following section.

1.1 Nature of the particle-fluid interactions in turbulent boundary layer

The behaviors of particles interacting with turbulence is a complex phenomenon and we lack the complete understanding of the mechanisms dominating the phenomenon. For instance, it was mentioned by Rashidi et al. (1990) that the mean partitions of the particle volumes guide the turbulence to major modifications. This influence was reported to emerge from the interaction of the particles possessing a size of few wall units (nondimensionalization of the wall units was achieved by friction velocity and kinematic viscosity) with the coherent wall structures in the wall region. The coherent wall structures can be categorized as the following:

1. high velocity regions and low speed streaks in the near wall region,

2. vortices in the streamwise and quasistreamwise directions,

3. "bursts" comprising of series of ejections off the wall layer through the outer flow, and "sweeps" off the outer flow through the wall.

The region referred as "outer flow" is where the velocity gradient reaches to small values. The space between the outer flow and the wall is more than 30-50 wall units.

Later, Kaftori et al. (1994a,b) proposed that those three models of coherent wall structures were the different aspects of just one structure in large scales, which is called the funnel vortices. A funnel vortice occurs in the streamwise direction and outgrows through the external regions of the wall. The vortex consists of a spiral form (figure 1.1.1).

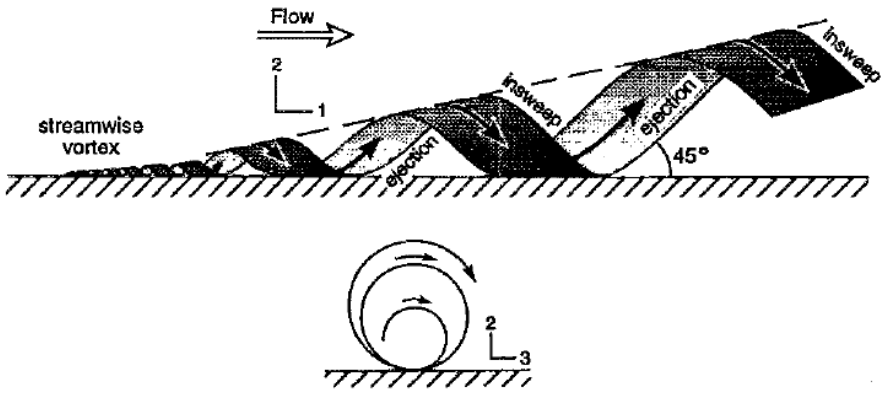

Figure 1.1.1: A funnel vortex. The three types of coherent wall structures are considered to be the manifestations of a funnel vortex suggested by Kaftori et al. (1994a).

Hetsroni and Rozenblit (1994) discovered an analogous invention in a horizontal conduit, where smaller particles of about 10 wall units piled in the low velocity streaks, in the meanwhile particles larger than 30 wall units had a random propagation on the bottom of the conduit. Cleaver and Yates (1973) were the first ones to find a linkage between the bursts and number of particles entraining from the wall. Sumer and Oguz (1978) studied the behavior of particles throughout bursts by utilizing photographic investigations, and measurements of particles solely inside of an opened channel. The influences of coherent wall structures on particle behaviour and at the near wall regions in a horizontal channel flow were analyzed by Kaftori et al. (1995a). It was reported that on the lower wall of the channel particles composed streaks in the streamwise direction. Particle dimensions and Reynolds number had a major effect on the streak forms. The Reynolds number was given as $Re_h = U_m h/\nu$. Here U_m indicates the mean velocity, h the level of water inside the channel, ν the kinematic viscosity.

Referring to the figure 1.1.2 particles form longer streaks at lower shear rates, conversely streaks are shorter at higher shear rates. It was seen that the streaks were formed in the low speed fluid domains. This conclusion is in accordance with the results obtained by Rashidi et al. (1990); Pedinotti et al. (1992); Hetsroni and Rozenblit (1994). In the high speed fluid domains, the funnel vortices sweep throughout the wall and shove particles faraway. In this way light particles were entrained, contrarily heavy particles formed streaks by being pushed aside.

In Kaftori et al. (1995b), the studies of Kaftori et al. (1995a) were extended to add the influence of funnel vortices on the particle dynamics in the distant wall regions. The empirical consequences of the work proposed a major influence of the coherent wall structures on particle dynamics. It was observed that those mechanisms also had an influence on the particles away from the wall. The velocity of the particles were approximately the same with the circumambient fluid velocities (figure 1.1.3). But the particle velocities were lower than the fluid velocity in average owing to the entrainment mechanism (figure 1.1.4). Entrained particles were sucked up by the flow and moved away from the wall.

When the structures spread and scatter the particles located in the outer flow, they rapidly speed up in order to catch up the velocity of the circumambient fluid. Nevertheless, in the near wall region the particles frequently lag even the circumambient fluid.

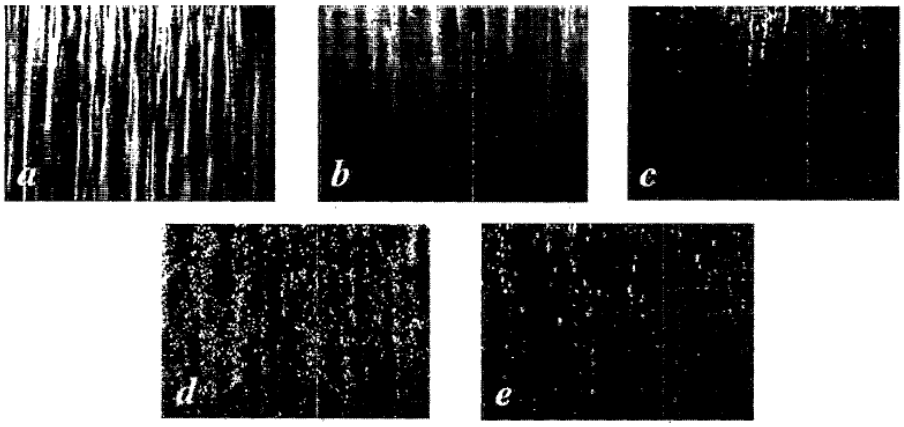

Figure 1.1.2: Particle dispersion on the lower wall of the channel. Streak forms change with the particle dimensions and Reynolds number: a) $100\mu m$, $Re_h \approx 5000$, b) $275\mu m$, $Re_h \approx 5000$, c) $275\mu m$, $Re_h \approx 9000$, d) $900\mu m$, $Re_h \approx 5000$, e) $900\mu m$, $Re_h \approx 9000$ (Kaftori et al., 1995a).

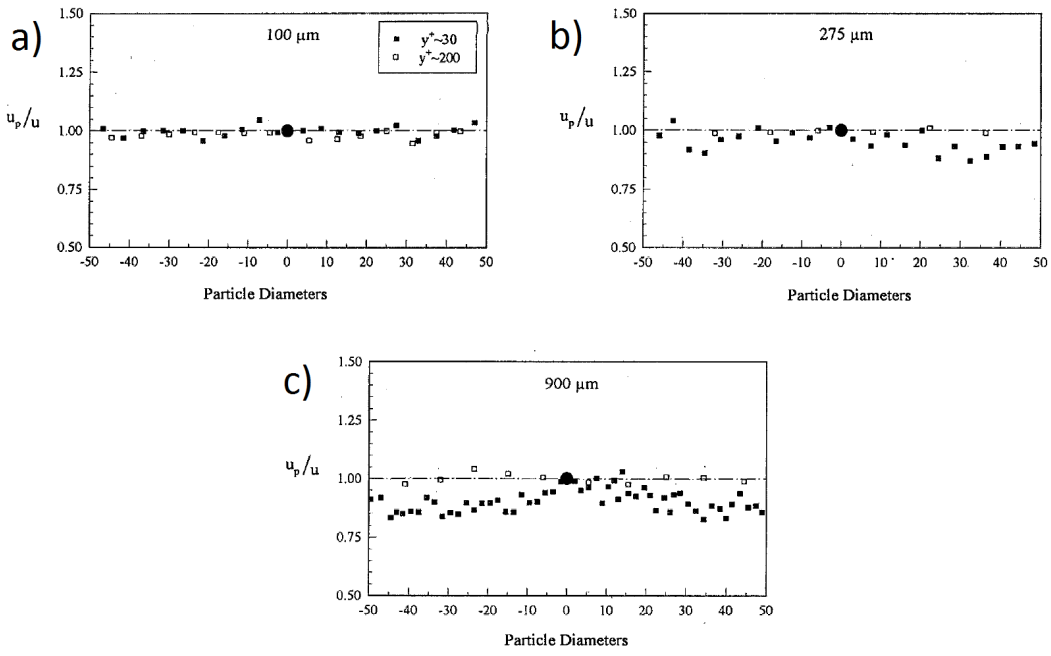

Figure 1.1.3: Velocity ratios of the particles and the circumambient fluid in average. Black circles indicate the particles. Negative values of particle diameter indicate fluid data points before the particles. Positive values indicate data points behind the particles. a) particle diameter $100\mu m$, b) particle diameter $275\mu m$, c) particle diameter $900\mu m$ (Kaftori et al., 1995b).

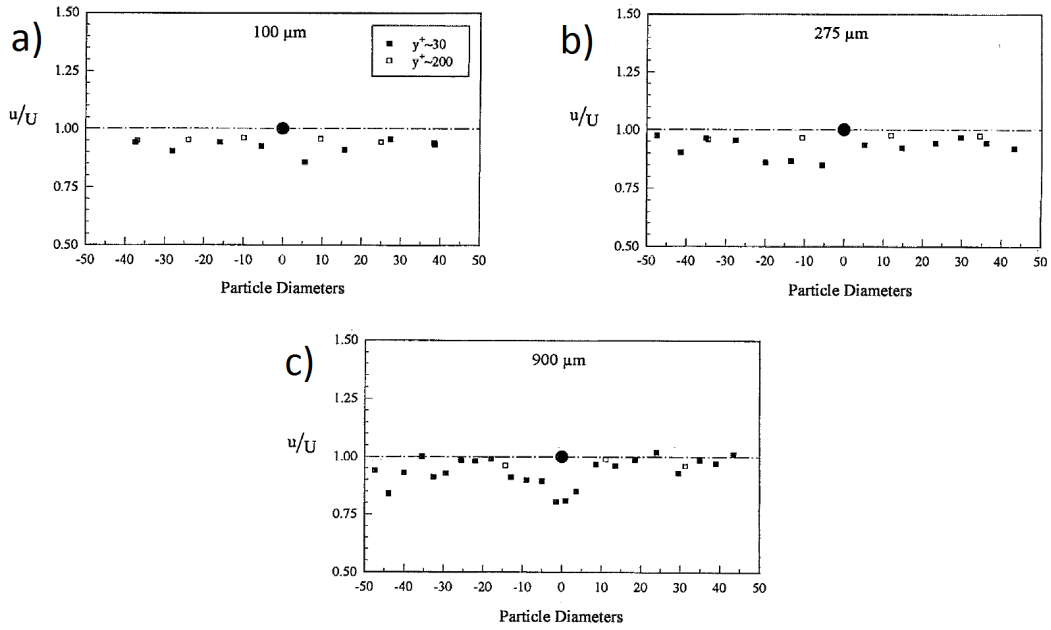

Figure 1.1.4: Average fluid velocity ratio in the surrounding of ascendant particles and the average velocity in the flow direction at the given height. Directional convention as in figure 1.1.3 a) particle diameter $100\mu m$, b) particle diameter $275\mu m$, c) particle diameter $900\mu m$ (Kaftori et al., 1995b).

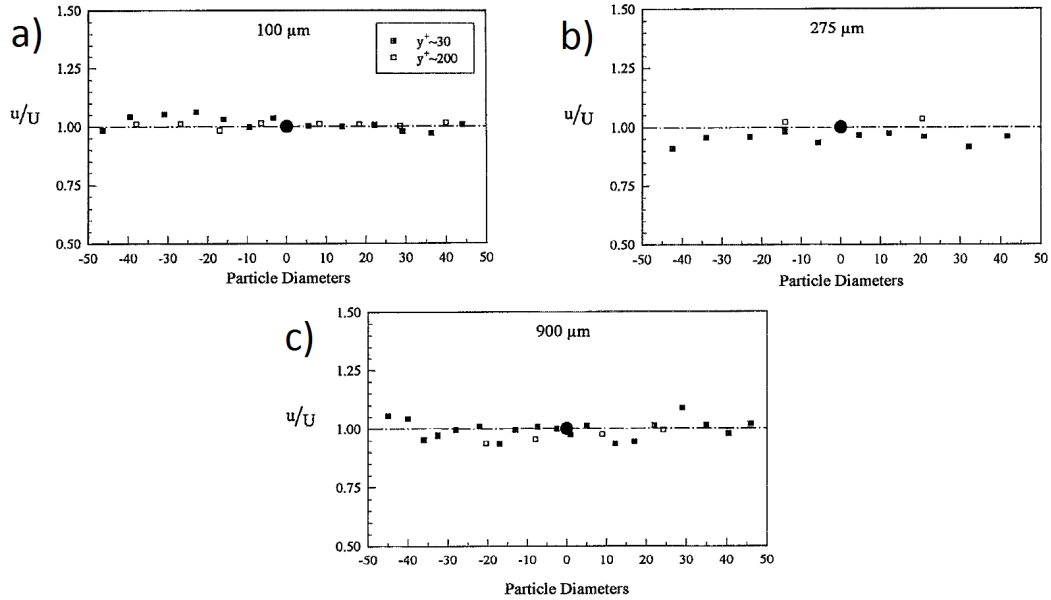

Figure 1.1.5: Fluid velocity ratio near the falling particles and the velocity in the flow direction at the mentioned height in average. Directional convention as in figure 1.1.3 a) particle diameter $100\mu m$, b) particle diameter $275\mu m$, c) particle diameter $900\mu m$ (Kaftori et al., 1995b).

Kaftori et al. (1998) examined the particle influences on wall turbulence. Three main effects of particles on turbulence regulation were concluded as the following:

1. particle existence at the wall, where the influence of the particles is quite analogous to inert roughness elements,
2. particles existence and their interplay with the wall structures, like the vortices in the quasi-streamwise direction, bursts and sweeps,
3. the influence of the existence of particles in suspension and their interplay in the distant wall regions.

It was seen that the particle existence at the wall and their interplay with the wall structures decreased the generation of the wall structures. This degradation was related to the non-dimensionless relaxion time and the size of the particles. Despite the degradation in generation of the wall structures, no major alteration in the average Reynolds stress and turbulent kinetic energy was detected. The reason was the wall structures emerging in the existence of particles contained more energy than the wall structures emerging in a unladen flow.

1.2 Introduction to particle image velocimetry (PIV) systems

In the previous section an overview of the interactions between particles and turbulent wall structures was made. The early experiments to observe those phenomena were performed under intrusive techniques, such as thermal anemometry or laser doppler anemometry (LDA). Intrusive means, the local flow field is affected by the velocity measurement techniques. Later, with the new technological developments on non-intrusive techniques, such as particle tracking velocimetry (PTV) and particle image velocimetry (PIV), became triend in flow measurements. Table 1.1 summarizes the advantages and disadvantages of some flow measurement techniques.

	Hotwire	LDA	PIV	PTV
Spatial resolution	low	low	very high	high
Temporal resolution	high	very high	very low	low
Velocity range	high	very high	very high	low
Dimensions of observation volume	-	-	2 - 3	2 - 3
Dimensions of velocity field	1 - 3	1 - 3	2 - 3	2 - 3
Result	vectors	vectors	vectors	trajectories

Table 1.1: Performance comparisons of some flow measurement techniques. A vector field is obtained by means of the analysis of hotwire, LDA and PIV techniques. Particles trajectories in a fluid is obtained by means of a PTV analysis (Maas et al., 1993).

PTV and PIV are considered to be similar techniques. In a PTV analysis one is able to get trajectories of discrete particles inside a 3-dimensional detection volume. One main restriction of the PTV technique is that it allows only low seeding densities. At this point PIV is a more advantageous technique because it allows relatively higher seeding densities (for more information about seeding particles refer to subsection 3.3.2). Further developments in the technology allowed time resolved PIV (TR-PIV) methods by means of CMOS (complementary metal-oxide-semiconductor) camera sensors. Now besides a high spatial resolution, one is also able to obtain a high temporal resolution in the measurements by means of a PIV technique. In most of the cases the quality in the temporal resolution will decrease the quality of the spatial resolution and vice versa, but this issue is trivial for the industrial type CMOS cameras (for more information about cameras and sensors refer to subsection 3.3.5). Additional developments to PIV systems contain the usage of multi-cameras for detecting the region of interest from different angles. This allowed to determine the 3-component (3C) velocity vectors of a flow field (for more information about 3C-PIV/PTV methods refer to section 3.2). Later on, volume observations became possible by using high power pulsed lasers (for more information about lasers refer to subsection 3.3.3, and about volumetric-PIV methods subsections 3.2.4, 3.2.5, 3.2.6, 3.2.7). One remarkable feature of PIV and PTV methods is that it allows the phase separation in multi-phase flows (for more

information about phase seperation methods refer to section 3.6). With this feature, one is able to seed the flow with tracer and inertial particles simultaneously and observe the interactions between the particles and the flow field. PIV technique became a trend in the flow visualization applications owing to the developments mentioned above.

The focus of this work is to design a test section to observe the kinematics of fibers in a fully developed turbulent channel flow. We consider that the PIV is the most suitable technique for the accurate observations of particle-flow interactions. In chapter 2 a brief overview of the experimental setup will be given. In chapter 3 optical measurement methods for PIV applications will be considered. In chapter 4 suitable PIV techniques for the proposed experiment will be considered. In chapter 5 the algorithms to analyse the data obtained from recording devices will be explained. In chapter 6 general rules for safety, setup, calibration and optimization issues will be defined.

2. General scheme of the experiment

The main aim of the experiment is to investigate the interactions between particles and turbulence and obtain 3-component velocity data of the fibers in a fully developed turbulent flow. A discussion about obtaining 3-component velocity data will be given within the section 3.2 in details. The interplay between turbulence and particles are complicated and they count on diverse parameters, as the rate of diameter of particle to a typical length scale of the flow, Stokes number and the concentration of particles. A combination of those parameters indicates the coupling nature between the turbulence and particles (Van Hout, 2011). Elghobashi (1994) categorized the interactions between particles and turbulence into one-way, two-way and four-way coupling. One-way coupling takes place if the particles are dragged but do not have any effect on the fluid. Two-way coupling happens when there is a momentum exchange from particles to the fluid. Four-way coupling is taken into account when an impact occurs just between the particles. All of these phenomena are within the interest of our study. To prevent a mass to be caused, we seperate the design of the experimental setup into two main sections: the hydraulic setup and the test section.

In the following subsections we will briefly discuss about those two major subjects of the experiment design.

2.1 Hydraulic setup

Since we want to perform an experiment with an anisotropic fully developed turbulence, we consider to obtain it with a flow inside a long channel. The channel has to be long enough to obtain a fully developed turbulence (see appendix A). We consider a channel of 10 meters for the Reynolds number, $Re = 100000$ to obtain a fully developed turbulence (figure 2.1.1). The reason of a channel flow rather than a pipe flow is to neglect the influence of the sidewalls. Therefore a channel with a cross sectional area of $30 \times 10\ cm^2$ is considered to be suitable for our case. Here, 30 cm is the width and 10 cm is the height of the cross sectional area of the channel.

There are mainly two methods to drive the flow inside a channel. First, one can drive the flow by means of a pump, as in the figure 2.1.2. The shortcoming of this method is that the vibrations of the pump will be delivered to the flow inside the channel, which in return will cause anomalies during the experiment. Second method is to drive the flow by gravity. The overwhelming feature of this method is that the vibrations delivered from the pump are negligible. In this case, water is pumped to a water tower. Since the water level inside the water tower is proportional to the Reynolds number, the Reynolds number of the flow can be controlled by adjusting the water level inside the tower. The pipe coming from the water tower is mounted to the channel by means of a diffuser, which allows a uniform velocity distribution at the inlet section of the channel. The test section is located way at the end of the channel to ensure that the flow is already fully developed. The outlet section of the channel is connected to a downstream pipe by means of a nozzle to deliver the water to the water reservoir, which is located below the water tower.

In the next section, general features of the test section will be discussed.

2.2 Test section

Test section is the other major part of the experimental design. The test section is located at the end of the channel, so the flow is already fully developed at that point. The material of the test

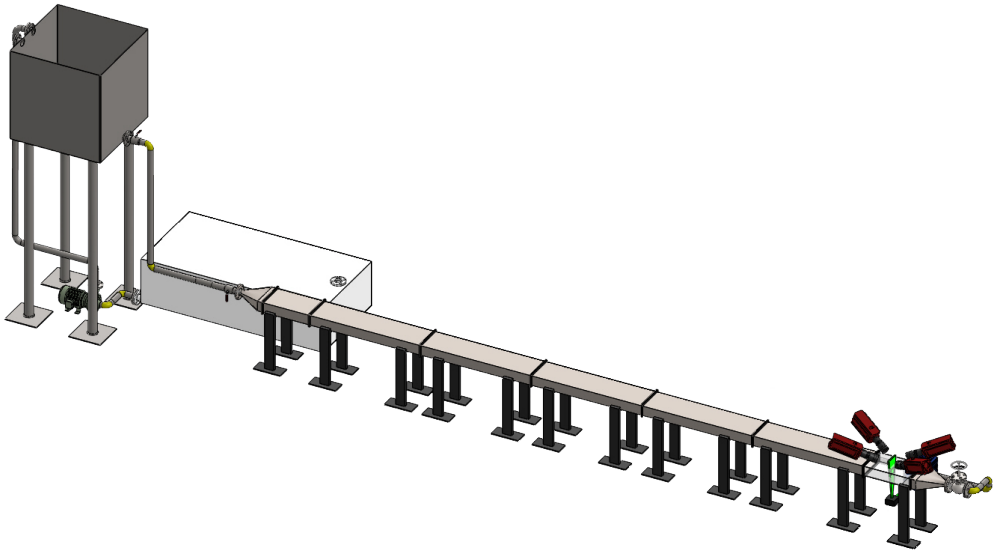

Figure 2.1.1: Hydraulic setup of the experiment and the test section at the end of the channel. Flow is driven by gravity by using a water tower. The flow is already fully developed at the location of the test section.

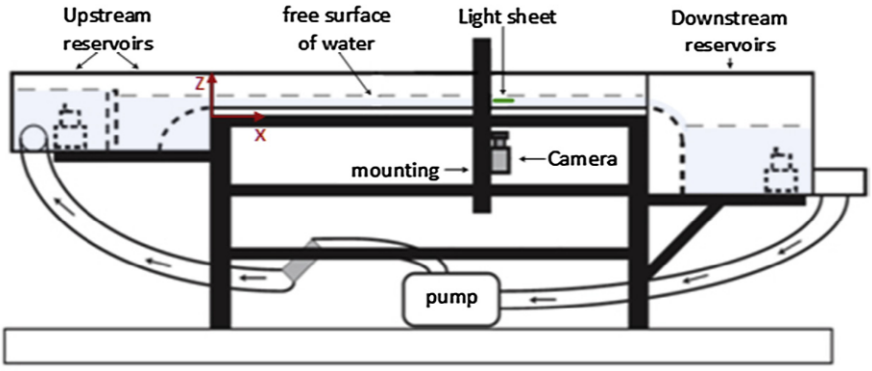

Figure 2.1.2: A pump driven hydraulic setup. The upstream reservoir was used to minimize the vibrations delivered from the pump, and the downstream reservoir is connected to an outlet pipe which delivers the water back to the pump (Hoseini et al., 2015).

section is considered to be plexiglass because of its high optical transmission and easy mounting capabilities. A high power, high speed laser is used to illuminate the region of interest (figure 2.2.1). The light-sheet was generated by means of laser-sheet optics. The cameras equipped with lenses were used to detect the rotational and translational kinematics of the particles occupying the region of interest.

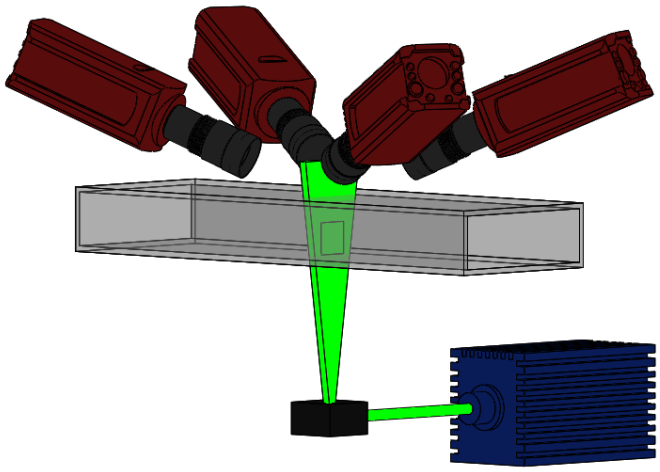

Figure 2.2.1: A schematic of the test section. The test section is transparent to ensure the optical access. A high speed class 4 laser is used to illuminate the region of interest. All of the cameras arranged to detect the region of interest from different directions.

Since the test section is the subject of this work, the instruments used in the test section will be broadly discussed in the following chapters. A detailed discussion about the PIV techniques to obtain 3-velocity components is made in the section 3.2. The general features of the components of the test section are discussed in the section 3.3. The optimal parameters for the transparent test section are derived in the subsection 3.3.1. The particles to represent the flow field are the subject of the subsection 3.3.2. A comprehensive discussion about the lasers are given in the subsection 3.3.3. The properties of the light sheet optics are explained in the subsection 3.3.4. A detailed discussion and a comparison of the camera sensors are given in the subsection 3.3.5. Considerations of the camera lenses and their optimization prosedures are vastly detailed in the section 3.4. Creation of a light-sheet is the subject of the subsection 3.4.3. Optimizing the pulse seperation of the laser is discussed in the subsection 3.4.4. The computations to design the test section are given in the chapter 4.

3. Optical measurement method

In chapter 2, general considerations of the proposed experiment were discussed. In this chapter, fundamentals of PIV metod and different PIV configurations will be discussed in detail. Furthermore, the rules for optimizing a PIV system will be given at the end of the chapter.

3.1 Classification of PIV systems

According to Hinsch and Hinrichs (1996), PIV systems were classified with the label (k, l, m). Here k = 1, 2, 3 is the number of velocity components detected by PIV system, l = 0, 1, 2, 3 is the number of spatial dimensions of the measured region, and m = 0, 1 is respectively the indication of instantaneous or continuous recording. Continuous recording indicates the high-speed PIV applications, with an obtained data frequency approximately an hundred times of an instantaneous recording (Jahanmiri, 2011). Pointwise techniques can be labelled as (3, 0, 1). Planar PIV technique is in the category of (2, 2, 0), which supplies 2D velocity information on an area at discrete recording times. Most of the PIV applications are classified in this category. On the other hand, holographic PIV belongs in the (3, 3, 1) category. Despite their high costs and complicated applications, holographic PIV systems with the label (3, 3, 0) were performed by some groups. Contrarily, stereoscopic PIV methods (3, 2, 1) maintain 3D velocity vectors on planar regions and they are being popular nowadays owing to their affordable costs.

Figure 3.1.1 gives a brief summary of diverse PIV systems with the belonging spatial and temporal resolutions.

In the section 3.3 basic components of PIV systems will be described.

3.2 PIV techniques

After introducing different PIV techniques, the optimization procedures for a basic planar PIV system will be considered in the section 3.4. Those procedures can still be applied to other PIV techniques but a planar PIV system with a single camera is not capable of supplying 3-velocity components of the flow field. Therefore some special considerations have to be made and some sophisticated techniques must be applied in the test section. In the following subsections, planar PIV will be briefly described and then suitable techniques to obtain 3-velocity components will be reviewed.

3.2.1 Planar PIV

A planar PIV is the simplest form of the PIV configurations. It consists of an optically transparent test section, one laser, one camera, a trigger, and a computer. The camera is faced perpendicularly to the generated light sheet (figure 3.3.1) and is able to obtain the 2-velocity components of the observed flow field. The trigger allows the synchronization between the laser and the camera. A PIV software is used to process the images obtained by the camera and estimate the displacement vector. The fundamentals of the algorithm used in the software will be described in chapter 5 for 2-dimensional case.

In the following subsections, more complex PIV systems will be explained in detail. Those systems are suitable to obtain 3-velocity components of the observed flow field.

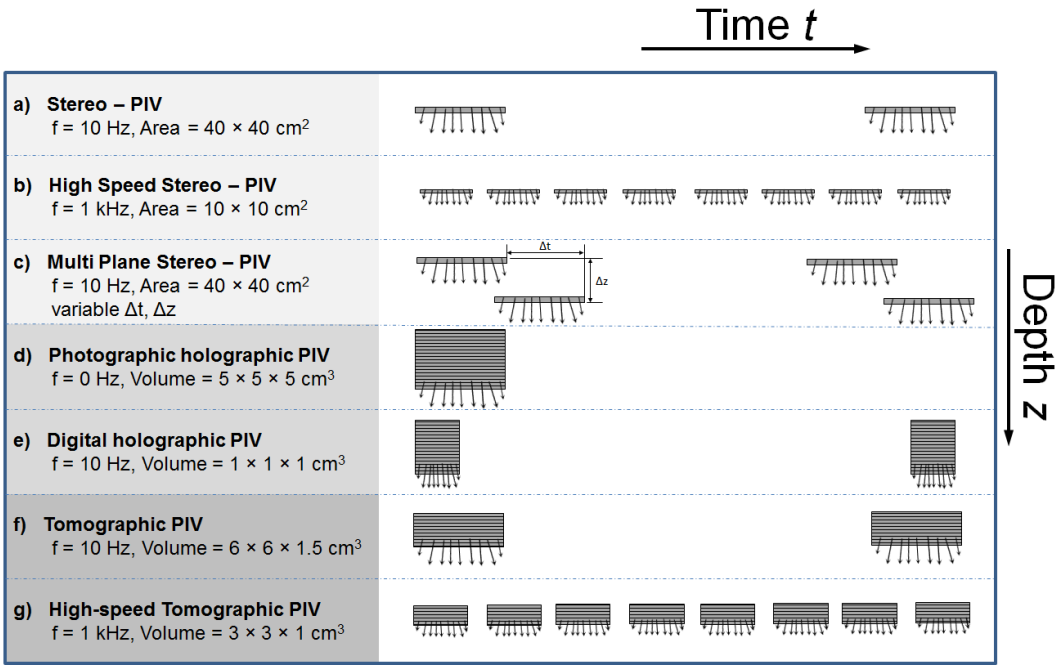

Figure 3.1.1: A schematic summary of diverse PIV systems with the belonging spatial and temporal resolutions. High-speed applications of PIV methods have a greater frequency rate in comparison with PIV methods with instantaneous recording. f refers to the frequency of the obtained data. Area and volume refer to the region of interest. Figure adopted from Jahanmiri (2011).

3.2.2 Stereoscopic PIV (SPIV)

It is important to understand the working principle of human eye in order to understand the concept of stereoscopic PIV (SPIV). Two camera techniques were improved to mimic the binocular vision of human eye, which allows the depth perception (Prasad, 2000b). This explanation is not satisfactory enough to present the advantages of stereoscopic systems. Therefore one should examine into the world of living things. The existence of two types of animals in the Kingdom Animalia was pointed out by Kaku (1995): predators and preys. Predators were evolved to have two eyes in front of their faces, so they can stereoscopically focus on their targets. Preys have eyes on both side of their faces, so they obtain a wide view of sight in order to look around for the predators (figure 3.2.1). That gives them a reduced focusing and 3D vision abilities. Yet, it is not possible to generalize 3D vision abilities of animals just depending on their monocular and binocular view of sight. Some animals might not have needed to develop 3D vision based on the optimization between evolutionary economics and environmental selection pressures (Dawkins, 2006).

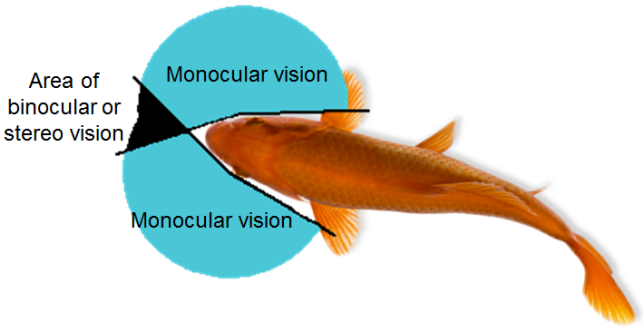

Figure 3.2.1: Monocular and binocular view of fish as a prey. Preys have narrow binocular view of sight compared to predators.

Also, the predators are characteristically more intelligent then their preys. It is no surprise that humans as predators have developed complex brain structures and algorithms in their evolutionary process. Complex brain algorithms act like a software to create illusions from the signals coming form our sense organs (Dawkins, 1976).

The relation between the camera and the computer in a PIV system is analogous to the relation between the eye and brain. Images obtained from the camera are being processed by the algorithms of a PIV software program (e.g. LaVision DaVis) and a representation of the observed flow domain is reconstructed in a virtual environment. In this sense, more complex PIV techniques use more advanced algorithms in the software.

SPIV operates with two cameras and one planar laser sheet. The cameras with diverse viewing angles are able to obtain the displacement in the z-axis. The cameras must be well calibrated in order to have the same focus point.

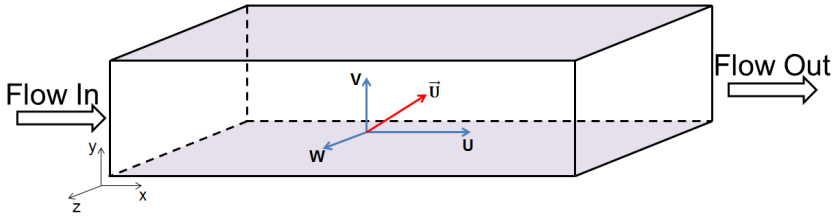

Figure 3.2.2: In fluid mechanics, components of the velocity field in the x, y and z directions are defined by variables U, V and W. x is the normal direction to the side walls, y is the normal direction to the bottom and top walls, z is the main flow direction.

With the planar PIV, one is able to obtain the U, V displacements of the in plane x and y directions (figure 3.2.2). That makes it possible to compute the U_y, V_y, U_z and V_z velocity gradients. It is possible to obtain the W component of the velocity field with the SPIV technique. Two additional velocity gradients W_y and W_z can be determined in this way. But it is not possible to obtain the velocity gradient components U_x, V_x and W_x with the SPIV (Ganapathisubramani et al., 2005). The components of the velocity gradient tensor are shown as:

$$\begin{bmatrix} U_x & U_y & U_z \\ V_x & V_y & V_z \\ W_x & W_y & W_z \end{bmatrix}.$$

This technique does not give the whole information of either the strain rate tensor or the vorticity vector, in consequence of the lack of x-components of velocity gradient tensor (Mullin and Dahm, 2005).

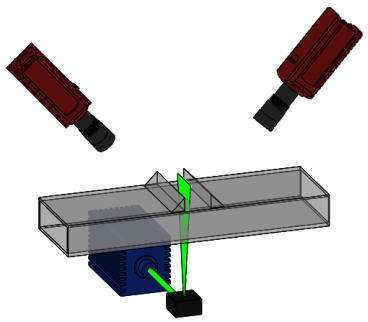

Figure 3.2.3: A typical setup of a SPIV system. Two water filled prisms were used for minimizing the refraction effects of light. No Scheimpflug condition was applied in this configuration in order to keep the lens magnification constant.

Figure 3.2.3 depicts a schematic of a SPIV model. The aberrations of particle images due to the refraction effect of optically transparent test section were reported by Prasad (2000b).Those effect can be minimized by using water filled prisms. The inclined wall of the prism must be parallel to the lens plane in this case. An other reported fact is the non-uniformity in

magnification due to the Scheimpflug condition. Scheimpflug condition provides the particles in the region of interest to be in focus across the object plane. This is provided by tilting the lens plane relative to the image plane. But, this condition exacerbates the non-uniformity in magnification. In figure 3.2.4, left and right cameras detect the 3-dimensional red vector in the object plane as different lengths, due to their different line of sights. The differentiation in the detected length of the vector obtained by each camera, is utilized to estimate the out-of-plane velocity component.

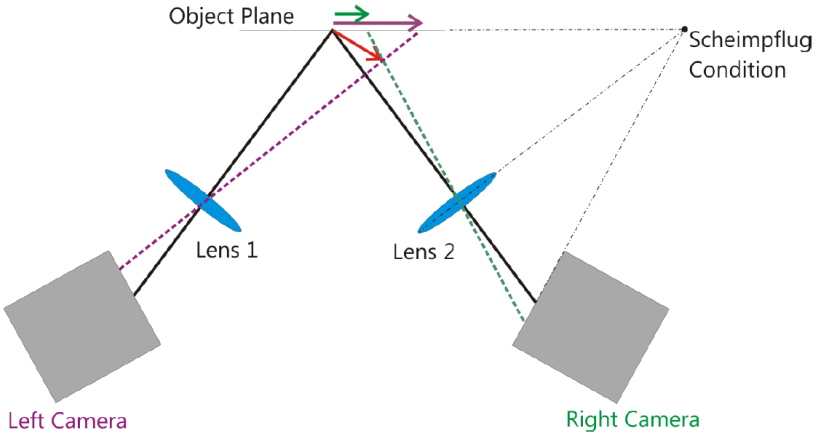

Figure 3.2.4: An illustration of the Scheimpflug configuration of the camera, lens and object plane in order to keep all points in focus across the object plane (Wernet, 2017).

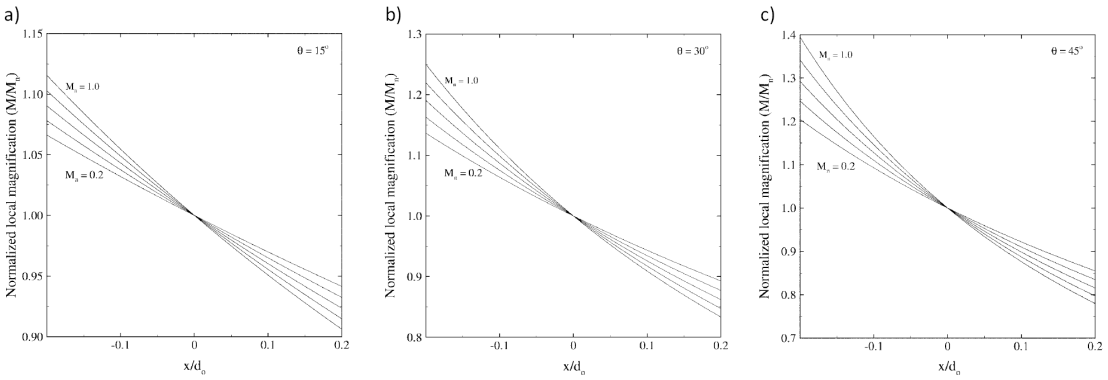

Figure 3.2.5: Alteration in magnification by utilizing the Scheimpflug condition. a) $\theta = 15^o$, b) $\theta = 30^o$, c) $\theta = 45^o$. θ represents the angle between lens plane and the object plane.

Figure 3.2.5 shows the alteration in magnification for the Scheimpflug condition for a) $\theta = 15^o$, b) $\theta = 30^o$, c) $\theta = 45^o$, where θ is the angle between lens plane and the object plane. The distance on the object plane, x, is normalized by the nominal object distance, d_o. The local magnification M_n is normalized by the nominal magnification (at $x/d_o = 0$). $M_n = \tan\alpha / \tan\theta$, where α is the angle between image plane and the lens plane. It is appereant that, the variations in the distance along horizontal axis causes non-uniformities in the normalized local magnification. However, decreasing the θ reduces the rate of non-uniformity. It is probable to set α to zero, without applying the Scheimpflug condition, and minimize the non-unformity in magnification. This application of SPIV was expressed by Gauthier and Riethmuller (1988).

3.2.3 Dual-plane stereoscopic PIV (DSPIV)

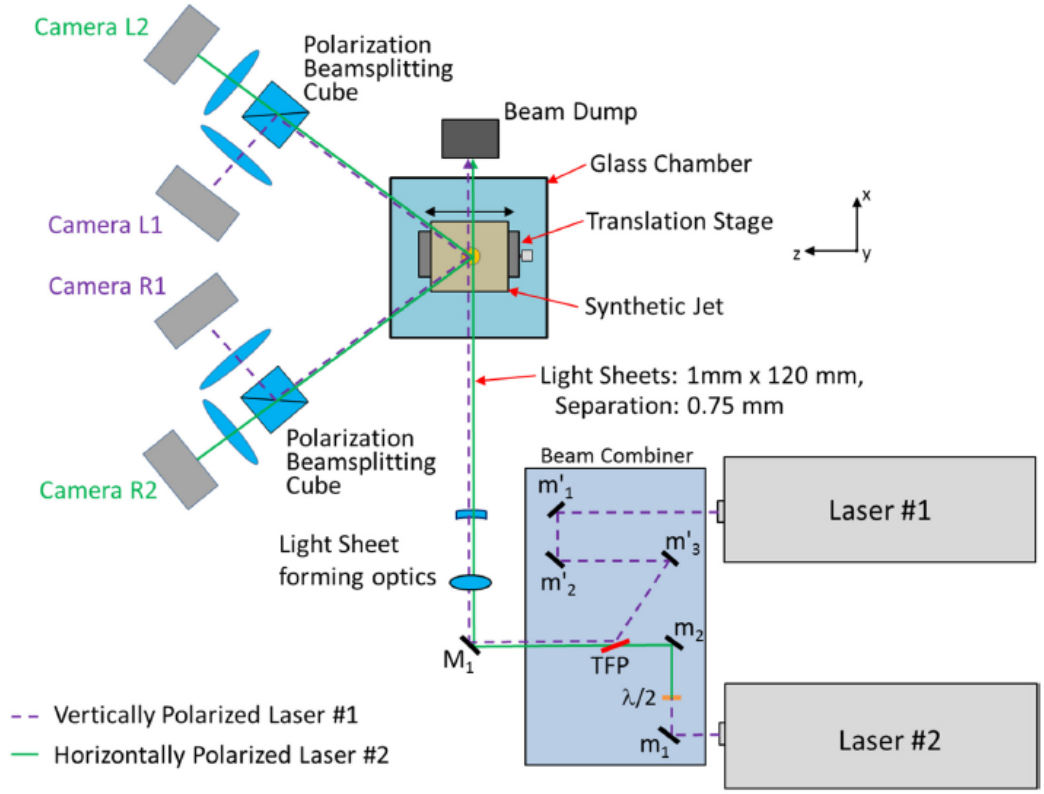

Figure 3.2.6: A schematic of a DSPIV system. In this case, both lasers emit the same wavelength of light. The purple colored laser beam depicts the vertically polarized beam paths. The green colored laser beam depicts the horizontally polarized beam paths. The vertically polarized laser beam is reflected by the beam-splitting cube and the horizontally polarized laser beam passes straight through the cube (Wernet, 2017).

This technique can be considered as an extension of SPIV. Dual Plane SPIV operates with 4 cameras and 2 offset light sheets. Two separated light sheets are generated by splitting the laser light with a beam splitter. Two light sheets can be obtained by the polarization of the laser beams from one Nd:YAG laser. Four cameras are paired into two groups. Each pair of camera are equipped with a polarizing filter to detect the scattered light from the related light sheet. Though, the utilization of two double-pulse lasers in some experiments were reported in the literature. Two laser systems have the both advantages of high power per light sheet and time flexibility, which allows the measurement of acceleration (Arroyo and Hinsch, 2007).

This technique makes it possible to determine all of the nine components of the velocity gradient tensor on a 2-dimensional region of interest (Mullin and Dahm, 2005).

The dual-plane PIV is a well developed measurement technique and no significant further development is expected (Arroyo and Hinsch, 2007).

3.2.4 Multi-plane stereoscopic PIV (XPIV)

Multi-plane stereoscopic PIV is an extension of dual-plane stereoscopic PIV. The main concept of XPIV is the combination of creating several offset light sheets and using stereoscopic viewing techniques. This technique maintains 3-dimensional and statistically significant data of velocity fields. XPIV was reported by Liberzon et al. (2004) as a suitable measurement method to obtain 3-dimensional velocity fields in the research of turbulence and coherent structures. High experimental effort is the main trouble of this technique. For each plane of light sheet an entire SPIV system must be set up with the elements to obtain optical isolation for each camera pair (Jahanmiri, 2011).

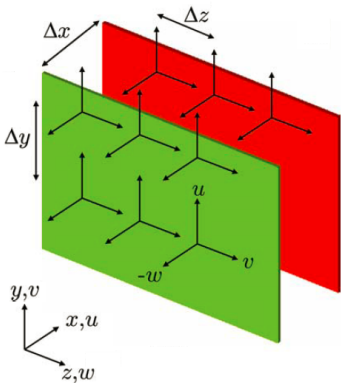

Figure 3.2.7: Basic principle for a dual plane stereoscopic PIV technique consists of two separate parallel light sheets. This measurement technique allows the determination of the whole velocity field (Mullin and Dahm, 2005).

3.2.5 Holographic PIV (HPIV)

Holographic PIV is the key to measure a 3D-domain and obtain the whole spatial components of the velocity field (Jahanmiri, 2011). HPIV covers a range of experimental methods that use the principle of the interference of scattered radiance from a particle and a reference beam to codify the amplitude data and phase of the scattered radiance incident on a sensor. The codified data is known as hologram and it can be utilized for the reconstruction of the primary intensity field by illuminating the hologram with the primary reference beam by means of optical techniques or digital estimations (Arroyo and Hinsch, 2007).

The holographic method is predominant to the most of the PIV techniques since it maintains an instantaneous 3D flow field inside a big volume of interest. HPIV will surely be one of the main tools for analyzing the turbulent flows. Yet, current holography techniques are limited with simpler flow configurations with the lack of ability to collect statistical data (Liberzon et al., 2004).

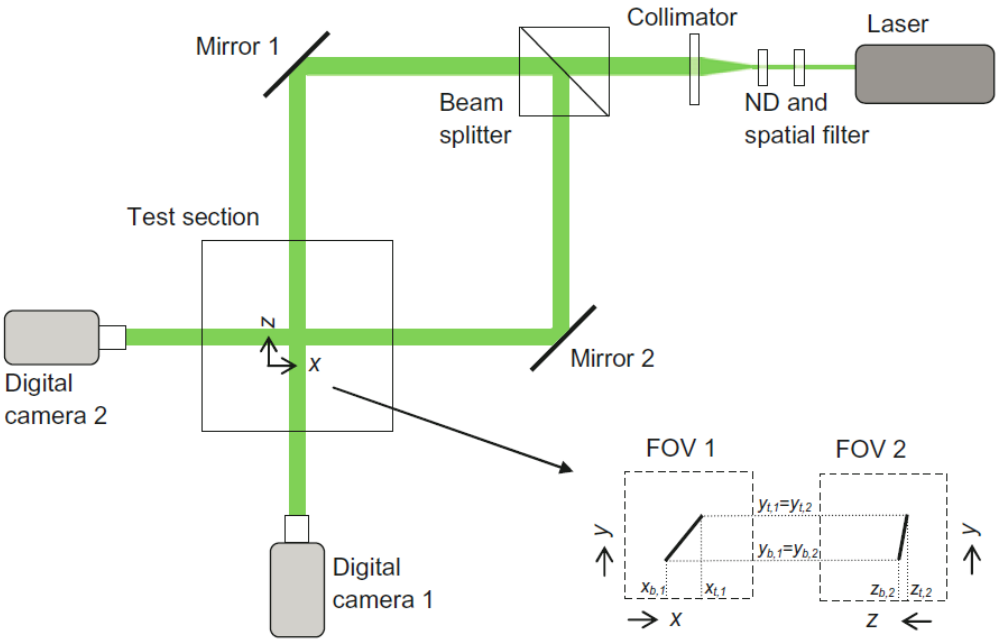

Figure 3.2.8: A schematic of a HPIV system. The laser beam is splitted by means of a beam splitter and oriented by the mirrors. In the middle of the test section a volume of interest is generated. At the bottom right, field of views of the two cameras were depicted.

3.2.6 Tomographic PIV (TPIV)

A complete comprehension of complex flows mostly necessitates the utilization of 3D measurement techniques. The utilization of planar methods to investigate vortex dynamics in complex flows is still left impaired with the 2D approach. 2-dimensional methods are not sufficient enough to investigate the whole details of 3-dimensional vortex structures and their temporal evolution (Scarano, 2012). TPIV uses the advantages of both SPIV and 3D-PTV. High speed applications of TPIV allows a statistically significant depiction of coherent motions in turbulent boundary layers. Figure 4.2.1 depicts the spatial and temporal measurement domains of diverse laser velocimetry techniques.

Typically 4 high resolution cameras simultaneously record the scattered light from the illuminated tracer particles by a high power pulsed laser within the detection volume (figure 3.2.9). Tomographic reconstruction algorithm (Multiplicative Algebraic Reconstruction Technique, MART) provides a 3- dimensional reconstruction of the illuminated particles by means of their light intensity distribution. Displacement vectors in an interrogation volume are obtained by 3D cross-correlation of the reconstruction of particle distribution at double laser exposures with a seperation of Δt utilizing advanced iterative multi-grid algorithms.

The main restrictions of TPIV systems are; the scope of the depth of the measurement volume (typically depth/width = 0.25, different depth/width ratios were also reported in the literature), high power laser requirement to illuminate the volume (typically 5$\times$ of a SPIV), long duration of digital evaluation of recordings (days, weeks, even months), size of the stored data (typically 10$\times$ of a simple PIV) (Jahanmiri, 2011).

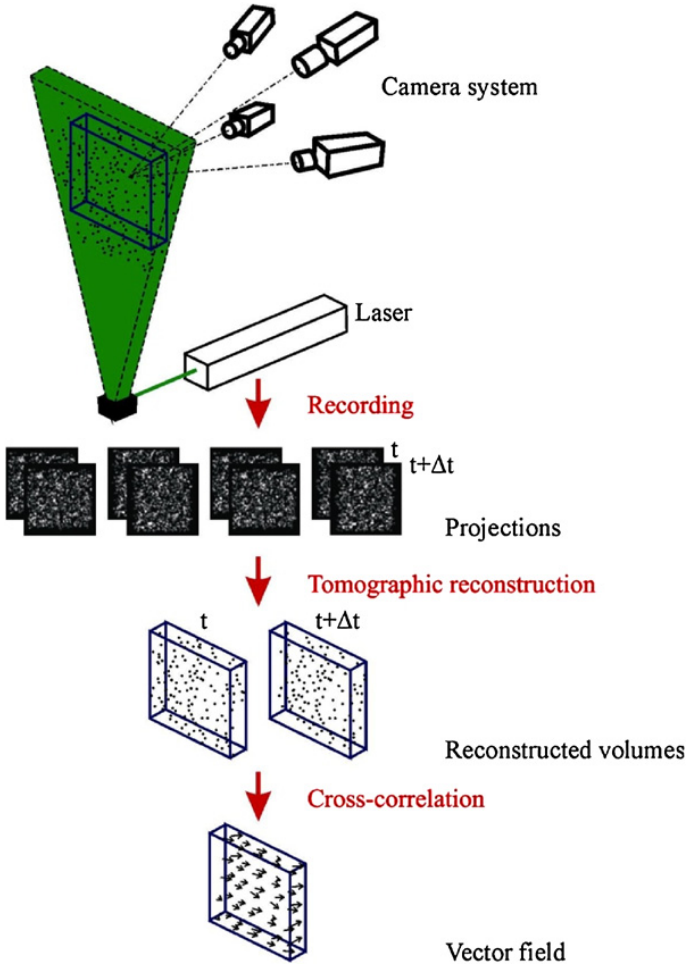

Figure 3.2.9: Principle of TPIV. The particles are illuminated by a high power pulsed laser in the flow within a 3D domain. Images of particles are recorded from different viewing directions (Elsinga et al., 2007).

3.2.7 Volumetric three-component velocimetry (V3V)

Volumetric three-component velocimetry (V3V) is another 3-dimensional measurement technique. Main application field of V3V is water and liquid flows (Pothos et al., 2009). Three high resolution CCD camera with one body, three aperture is used for 3-dimensional image shooting. One Nd:YAG laser is used for a volume (up to $14 \times 14 \times 10 cm^3$)illumination (see figure 3.2.10). Typical frequency of double-exposure data acquisition is approximately 7.25 Hz. Fast data processing (1 - 5 minutes per capture) is one of the unique features of V3V operation.

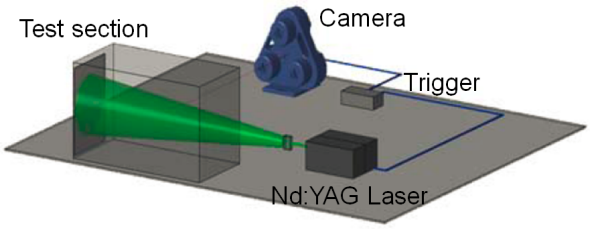

Figure 3.2.10: Experimental setup of V3V technique. One body, three aperture CCD camera and a Nd:YAG laser are the main instruments of a V3V system (Pothos et al., 2009).

Three CCD sensors constructed into one faceplate in a coplanar triangular pattern. The intersection of field of views of the sensors shapes the mapping field of the camera. Particles inside the region of interest are captured by the camera from three distinct perspectives generating a multiview vision. The particle images on each sensor are formed in a triangular shape as in the figure 3.2.11. The depth position of a particle is determined by the size of the triangle. The particles closer to the image plane will have a bigger size of the triangle.

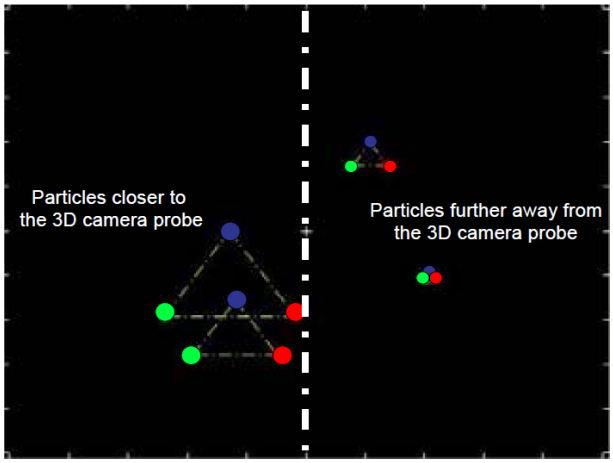

Figure 3.2.11: Operation principle of V3V system. Particles are detected by distinct perspectives of the camera. Red, blue and green dots represent the appearances of a particle from different viewing angles. Different particle images form a trianglular shape. The closer the particle is to the image plane, the larger the size of the triangle (Pothos et al., 2009).

3.3 Basic components

The basic components of a planar PIV system indicated by (Prasad, 2000a) as follows:

1. A transparent test-section containing the flow with tracer particles (section 3.3.1),
2. A laser to illuminate the detection area or volume (section 3.3.3),
3. A CCD or CMOS camera as a recording hardware (section 3.3.5),

4. A computer with a software, which is able to process the recorded images and compute the velocity field of the flow (figure 3.3.1).

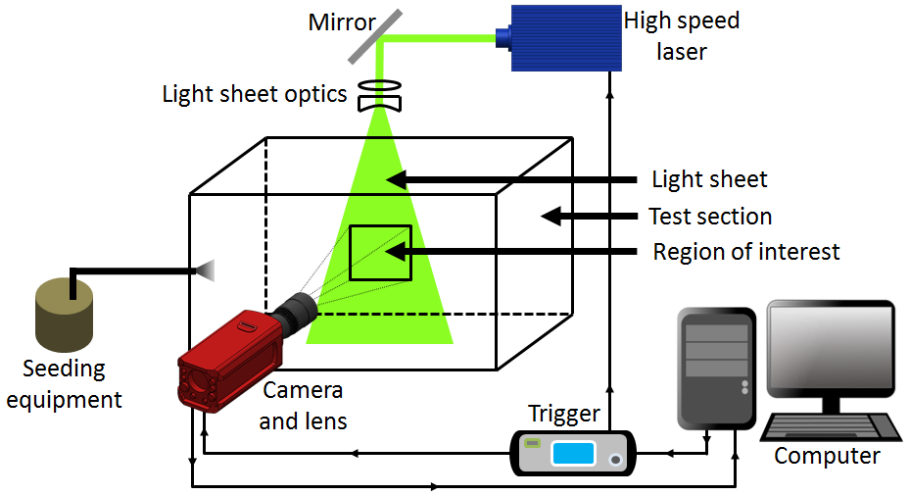

Figure 3.3.1: Basic requirements of a PIV system consist of a test section, laser, camera and a computer with suitable software to process the recorded images. Trigger allows the synchronization between laser and camera. Figure inspired by (Prasad, 2000a).

In the following subsections, the mentioned components of a PIV system will be discussed in details.

3.3.1 Optically transparent test-section

The test section is made of transparent material in order to allow optical access. Different materials may have different optical properties, e.g. plexiglas has %8 less transmission capability than a window glass. However, due to the construction issues (e.g. drilling holes, mountings) plexiglas is generally considered in most of the applications. In order to prevent high refraction values, thickness of the glass must be kept as thin as possible. The optimum thickness of the material of the test section will be examined with the following expressions.

An electric planewave impinging normally upon a thin slab of glass of thickness d is considered. Upon deploying a round trip on the sheet, the plane wave obtains a phase δ defined as

$$\delta = 2nk_0 d \ . \tag{3.3.1}$$

Here, n is the refractive index of glass and k_0 is the wavenumber in vacuum (Born and Wolf, 1970). r and t are the reflection and transmission coefficients from the incidence medium (air or vacuum) to the glass. r', t' are the coefficients of reflection and transmission from the glass back to the incidence medium.

When the electric field of incidence medium has an amplitude E_i at the boundary of air-glass, it is easy to figure it out that the amplitude of the wave reflected devoid of propagating inside the glass is rE_i. The amplitude of the wave turned back by the glass ("reflected") afterwards one round trip is $tt'r\exp(i\delta)E_i$. The one tuned back afterwards double round trips is $tt'(r')3\exp(2i\delta)$. The one turned back afterwards n round trips is $tt'(r')^{2n-1}\exp(in\delta)E_i$. Therefore, in order to discover the entire amplitude of the reflected wave E_r, we require to sum each of the contributions. Hereby,

$$\begin{aligned} E_r &= E_i \left(r + tt' \sum_{n=1}^{\infty} (r')^{2n-1} \exp(in\delta) \right) \\ &= E_i \left(r + \frac{tt'r' \exp(i\delta)}{1 - r'^2 \exp(i\delta)} \right) \ . \end{aligned} \tag{3.3.2}$$

The last portion utilized the famous equation for an infinite geometric series. With the Frensel's equation, we obtain

$$\begin{aligned} r &= -r' \ , \\ r^2 = r'^2 &= R \ , \\ tt' &= T \ , \\ R + T &= 1 \ , \end{aligned} \tag{3.3.3}$$

for a sheet of a dielectric material, e.g. glass. Hereby, the reflected amplitude shall be simplified as

$$E_r = E_i \frac{1 - \exp(i\delta)\sqrt{R}}{1 - R\exp(i\delta)} \ . \tag{3.3.4}$$

In order to obtain an equation for the reflected intensity, we use $I \propto \mid E \mid^2$ and find

$$I_r = \frac{2R\sin^2\left(\frac{\delta}{2}\right)}{(1-R)^2 + 4R\sin^2\left(\frac{\delta}{2}\right)} I_i \ . \tag{3.3.5}$$

Hereby, the reflected intensity is zero if $\delta/2$ is one of the zeros of the sinus function. The thickness can be computed easily by replacing the k_0 with $2\pi/\lambda$ and introducing x as an integer to make the sin-function zero:

$$\frac{\delta}{2} = \frac{2\pi}{\lambda} nd = x\pi \ \Rightarrow \ d = \frac{x\lambda}{2n} \ . \tag{3.3.6}$$

A list of the thicknesses of different materials to obtain transparency for a given wavelength, λ, under an optimal value of "x" can be found in the table 3.1.

	x	λ $[nm]$	n @ $20°C$	d $[mm]$
Plexiglas	56499	532	1.495	10
Crown Glass	56499	532	1.519	9.8
Plate Glass	56499	532	1.520	9.8
Flint Glass	56499	532	1.670	8.9

Table 3.1: Thickness, d, of different type of glasses for $\lambda = 532\ nm$. x is the optimal value of the integer obtained from equation (3.3.6), n is the refractive index of glass at $20°C$.

Shariati et al. (2000) used 12 mm thick plexiglas sheets to facilitate measurements with an Argon Ion Laser Doppler Velocimeter (LDV). Gürlek (2017) used 10 mm thick plexiglas sheets in a PIV experiment with a double pulsed Nd:YAG laser source (120 mJ, 532 nm). In the subsection 3.3.2, the properties of seeding particles will be described.

3.3.2 Seeding particles

PIV images of the flow field are obtained by the detection of the seeding particles. Particles are released in the flow with an optimal size, distribution and concentration. For convenience, the seeding particles should not be toxic, corrosive or chemically instable. They must be small enough to follow the flow faithfully, yet large enough to scatter the light with a sufficient intensity to detect them. The account for the particle motion related to the motion of the fluid can be estimated by the step response velocity. The step response of the tracer particle velocity, U_p, is expressed as the following exponential law,

$$U_p(t) = U\left[1 - \exp\left(-\frac{t}{\tau_p}\right)\right] \ , \tag{3.3.7}$$

where, τ_p is the relaxation time of the tracer particle and defined as,

$$\tau_p = d_p^2 \frac{\rho_p}{18\mu} \ . \tag{3.3.8}$$

ρ_p is the density of the tracer particle, d_p is the diameter of the tracer particle, and μ is the fluid dynamic viscosity. Tracer particle will faithfully follow the flow if the smallest time scale of the fluid is greater than the relaxation time of the tracer particle. In this way, the local fluid velocity can be accurately mimicked (Dabiri, 2006).

Next, we will be discussing about the general features of the light sources used in PIV experiments.

3.3.3 Light sources

Lasers are very advantageous in PIV applications, because they are able to emit monochromatic light with high light intensity proportional to their operation power. The light obtained from a laser can be easily splitted and formed into light sheets to illuminate the region of interest. Pulsed lasers have more advantages compared to continuous wave lasers. Pulsed laser can emit a bundle of light with high energy, in return the particles in the illuminated area can reflect light with high intensity, therefore it is easier to detect them. The pulse duration of pulsed lasers are characteristically a few to several nanoseconds. Therefore, particles moving with high speeds will be frozen during the laser exposures (for instance, a particle moving at 100 m/s will shift only 0.06 mm during a 6 nanosecond pulse (Jahanmiri, 2011)). This feature minimizes the blurring effect obtained in the PIV pictures. Frequency-doubled Nd : YAG (neodymium : yttrium aluminum garnet) pulsed lasers are commonly used in PIV systems, which are capable of generating 0.1 to 0.3 joules/pulse, at a instauration rate of tens of kHz. Two cavity Nd : YAG lasers, which can produce two independent laser pulses with 532 nm wavelength are provided by most of the companies nowadays.

Only the class 4 lasers are used for PIV applications, which cause eye hazard if directly, reflected, or diffusely-reflected beam is viewed. Skin and fire hazard can take place in direct beam. Therefore class 4 lasers are only used in research and industry applications.

Motivation: Light and its properties

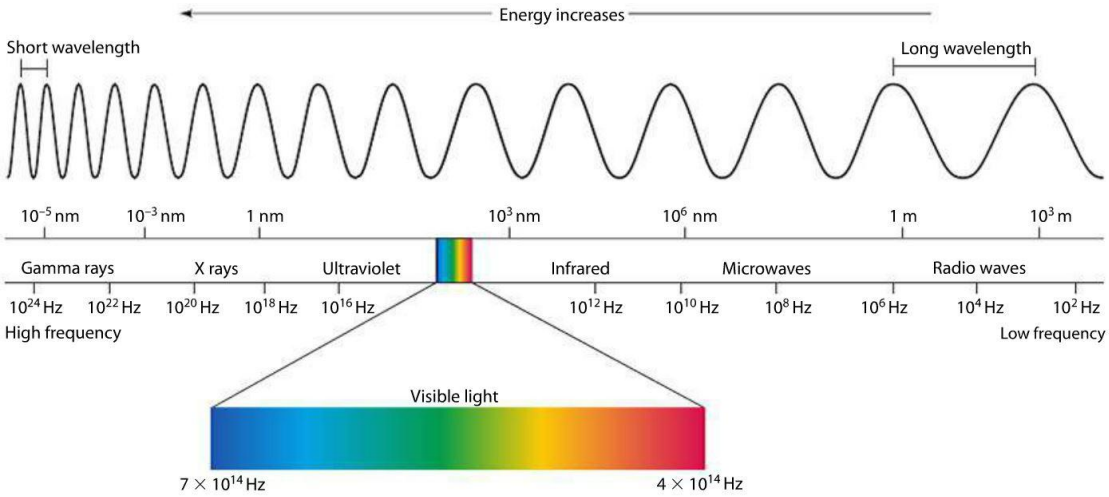

Figure 3.3.2: The Electromagnetic Spectrum. Light shifts towards red in the electromagnetic spectrum as the wavelength increases. Conversely, light shifts towards blue as the wavelength decreases (Junior, 2017).

Light is a sinusoidal periodic oscillation in an electromagnetic field achieved by the exchange of photons between electrically charged particles. Photon, the quantum of the electromagnetic field, is one of the elementary particles, to which the Bose–Einstein statistics apply. A photon, as being a subatomic particle, is emitted and absorbed as a point-like particle but in between it is propagated through an optically transparent medium as a wave. This phenomenon is called the wave-particle duality of photons. Electromagnetic oscillations are governed by Maxwell's four equations and the distance between two local maxima or local minima in the electromagnetic oscillation is called the wavelength of light, which encodes the color of a photon. Light shifts

towards red in the electromagnetic spectrum as the wavelength increases. Conversely, light shifts towards blue as the wavelength decreases (see figure 3.3.2).

Another important parameter of light is the frequency. Frequency is the number of the local maxima or local minimas detected by an observer per unit time. It is easy to summarize the relation between the wavelength and frequency in a simple algebraic equation:

$$c = \lambda\nu \ . \tag{3.3.9}$$

Here "c" is the speed of light, "λ" is the wavelength and "ν" is the frequency of light.

In the subsection 3.3.4 the operation principles of light sheet optics will be discussed.

3.3.4 Light sheet optics

The curt period high power beams of pulsed Nd:YAG lasers shall directly harm optical fibers. Hereby, the most canonical techniques create a light sheet by utilizing laser optics. The variants to control in creating the laser sheet in intercourse to the laser position in accordance with the empirical setup are the widening angle, thickness, or waist of the beam. There exist different methods to attain suitable control which contain a diversity of combinations of spherical and/or cylindrical lenses. A common setup utilizing three cylindrical lenses, is indicated in figure 3.3.3. In this example, the primary lens is a divergent cylindrical lens which is employed to widen the laser beam to a light sheet. The following lenses are employed to control the position of the waist of the beam. To achieve that, following lenses are utilized and they are 90 degrees rotated with respect to the primary lens. Subsequently, changing the gap between the following lenses will let the regulation of the location of beam waist (Dabiri, 2006).

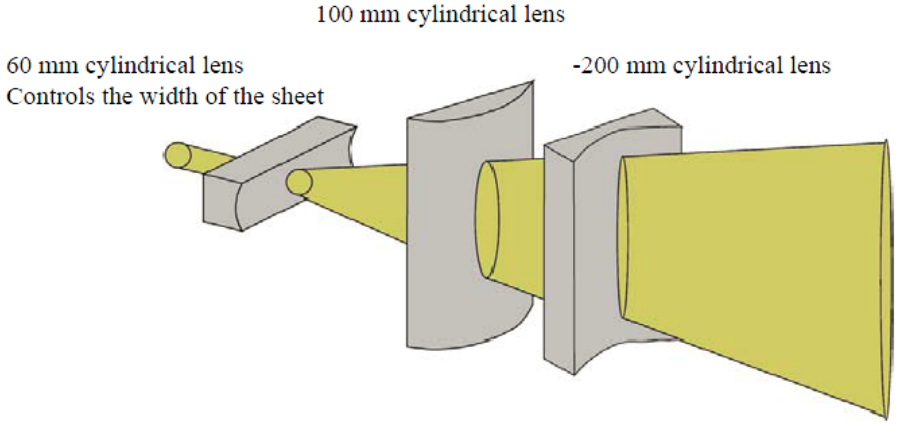

Figure 3.3.3: Illustration of a typical laser sheet propagating optical setup.
The focal lengths of the lenses are respectively 60 mm, 100 mm, -200 mm (Maheo, 1999)

Laser sheet with 1 mm thickness is widely used in 2D-PIV applications for flow measurements (see experimental setups: Sabban et al. (2017); Bordoloi and Variano (2017); Sabban and van Hout (2011); Hoseini et al. (2014)).

In the following subsection general characteristics of camera sensors will be discussed.

3.3.5 Recording hardware

There exist a diversity of camera sensors available at the present time, but solid state sensors are usually in trend. Even though electronic imaging related to vidicon tubes has attained a high status of improvement onwards their promotion fifty years ago, their significance to characteristical imaging implementations has reduced strikingly in favor of the solid state sensors (Jahanmiri, 2011). The most widespread ones are CCD (charge coupled devices), CID (charge injection devices) and CMOS (complementary metaloxide semiconductor devices). In the last two decades, the CCD has met the most extensive utilization. Yet, the steep improvement of chip technology in the beginning of 90s, let the production of CMOS sensors with a healed resolution and signal-to-noise ratio. After several years they are even more frequently utilized in digital photography, machine visualization and in time resolved PIV applications (Raffel et al., 2007).

CCD and CMOS sensors basically convert photons to electrons by means of a voltage exerted between metal conductors of a pixel sensor (Raffel et al., 2007). The operation principle of a pixel sensor is based on the photoelectric effect. That is, an electron is emitted when electromagnetic radiation with a proper wavelength is absorbed by matter. In case of camera sensors, the proper wavelength of electromagnetic radiation is within the range of visible light (see figure 3.3.2). The amount of electrons emitted will be proportional to the intensity of light, which is proportional to the amount of photons. In CMOS cameras, electron to voltage conversion takes place within each pixel sensor. Then the voltage signals from each array of pixel sensors are integrated as an output signal. In CCD cameras, the output signal of each pixel is an electric field consists of electrons. As shown in figure 3.3.4 electron to voltage conversion occurs before the voltage signal output section of a CCD sensor.

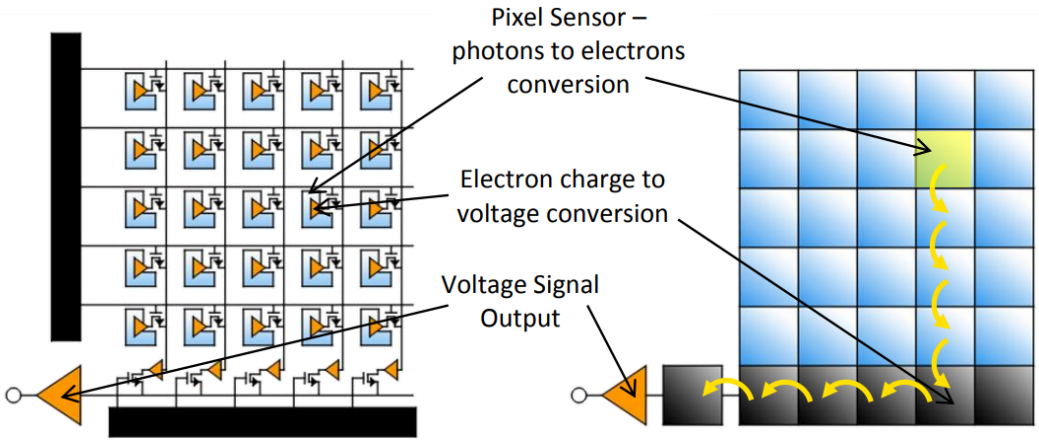

Figure 3.3.4: Working principles of CCD and CMOS sensors. Output signal of a CCD pixel is an electric field, contrarily the output signal of a CMOS pixel is voltage (Litwiller, 2001).

Comparison of the camera sensors

In this section a general discussion of the camera sensors and main differences between them is given.

The "rolling-shutter effect" is a general issue on CMOS sensors, and it's a problem when you're recording a video, trying to seize a fast moving object, or panning the camera when shooting. Each pixel of the CMOS sensors view what is in front of the lens, as if they are reading a book; every pixel row capture what it detects line by line, in a fast series. As a consequence, each pixel is not detecting the same thing at the same moment, and sometimes you might see strange artifacts in video or images captured with a CMOS sensor: tilted vertical lines, distorted moving objects, and horizontal bands of light. Conversely, CCD sensors capture the whole frame at the same moment, utilizing what is named a global shutter. But companies have developed CMOS sensors which utilize a global shutter, it shall take time till the technology is established in consumer-level cameras.

Conventionally CMOS chips have been collaborated with cheaper manufacturing costs, much better energy efficiency, faster data transfer speeds, and the on-sensor circuit copes with some processing tasks when the data comes off from each pixel and the sensor. The image processor of a camera has a lot to do with the ultimate image, and those are becoming powerful day by day. CMOS cameras are not suitable for a usage of long periods of time, because they begin to heat-up extremely and that may burn the sensor of the camera. Therefore CMOS sensors are not employed in cameras for long time operations, e.g. security cameras. The companies claim to provide a warranty for a CMOS camera, but it will be out of warranty when the CMOS sensor burns.

Table 3.3 summarizes the main properties of cameras employed in some of the previous PIV experiments. CCD and CMOS cameras have a broad range of resolution but CCD cameras aren't capable of high speed shooting with a high resolution. A camera with a smaller pixel size will have a better spatial resolution, which will provide images with a better quality. A shorter

	CCD	CMOS
Shutter	Global shutter	Rolling shutter effect
Light sensitivity	Good	Bad
Noise level	Low	High
Image quality when heats-up	Increases	Decreases
High speed shooting	At low resolution	At high resolution
Data transfer	Slow	Fast
Production costs	High	Low
Energy consumption	High	Low
Warranty	Yes	No

Table 3.2: Comparison of sensor types.

exposure time is prefered in PIV applications, because we want the particles to be frozen during the exposure.

PIV Camera	Sensor	Resolution [pixels × pixels]	Frame Rate [Hz]	Pixel Size [μm]	Exposure Time	Lens Mount
Ultima APX Fastcam (Sabban et al., 2017)	CMOS	1024×1024	2000	17	$4[\mu s] - 16.7[ms]$	F-Mount C-Mount
Imager Pro-X (Bordoloi and Variano, 2017)	CCD	1600×1200	30	7.4	$500[ns] - 49[d]$	
Basler A504k (Cole et al., 2016)	CMOS	1280×1024	500	12		F-Mount
Mikrotron EoSens MC-1362 (Cole et al., 2016)	CMOS	1280×1024	500	14		F-Mount C-Mount
PCO Sensicam QE (Dearing et al., 2013)	CCD	1376×1040	10	6.45	$500[ns] - 3600[s]$	
Imager Pro HS 4M (Hoseini et al., 2015)	CMOS	2016×2016	1300	11		F-Mount

Table 3.3: Cameras employed in some previous PIV experiments. CMOS and CCD cameras may have a vast range of resolution. CMOS cameras are major when high speed shooting.

3.4 Optimization considerations

In order to obtain sharp images of the particles inside a flow, some considerations have to be made. Considerations of the lens magnification, focal length, aperture size and depth of field are required to obtain high quality images without any blurring effects. Considerations of light-sheet creation are essential to generate an appropriate light-sheet thickness for a suitable PIV technique. Considerations on pulse separation are crucial in order to prevent high saturation levels reflected from the particles. Optimization considerations taken into account by Prasad (2000a) as follows:

3.4.1 Particle image diameter

Referencing to figure 3.4.1 a couple of handy equations can be composed for image distance d_i and the object distance d_o.

$$\begin{aligned} d_0 &= (1 + M^{-1})f \ , \\ d_i &= (1 + M)f \ , \\ M &= \frac{d_i}{d_0} \ , \end{aligned} \tag{3.4.1}$$

where M is the magnification of the image and f is the focal length of lens. For determining the image diameter of the particle on the image plane, we have to consider both diffraction and geometric influences. It is indicated by the geometric grounds so that the image diameter should be Md_p. Here d_p is the diameter of the particle on the object plane. For general recording

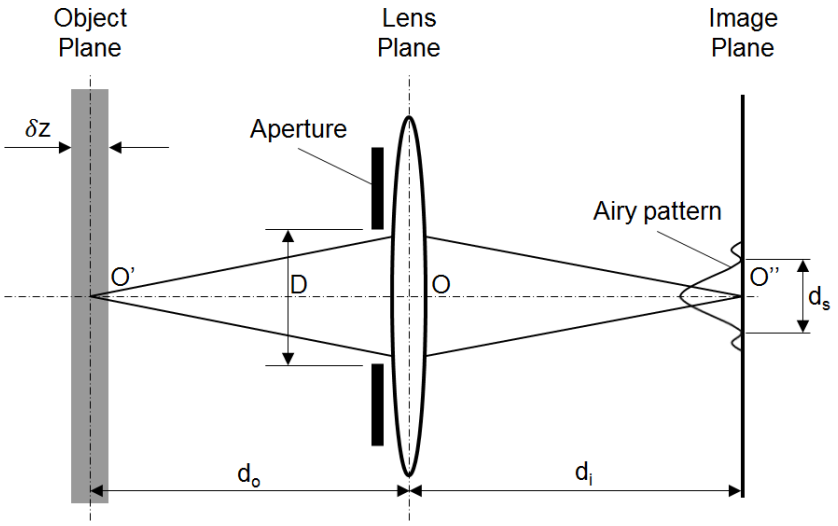

Figure 3.4.1: Diffraction effects throughout particle image recording. δz is the depth of field (section 3.4.2) , d_o is the object distance, d_i is the image distance, d_s is the diffraction limited spot-size, magnification is the ratio of *image distance* to the *object distance*. Figure inspired by Prasad (2000a).

conditions, diffraction is significant. Because of diffraction, in the object field a point source at O' will outstretch into an airy pattern on the image plane centralized at O". Here, d_s which is the diffraction limited spot size, is related to the diameter of the aperture of the lens D, lens focal length f and the wavelength of the laser l (figure 3.4.1):

$$d_s = 2.44(1+M)\frac{f}{D}\lambda \ . \tag{3.4.2}$$

F-number of the lens is equal to the ratio of focal length and diameter of aperture, f/D. If we combine those two effects, the effective particle image diameter d_e is identified as

$$d_e = (M^2 d_p^2 + d_s^2)^{1/2} \ . \tag{3.4.3}$$

In some cases if $Md_p >> d_s$, $d_e \approx Md_p$; contrarily, if $Md_p << d_s$, $d_e \approx d_s$.

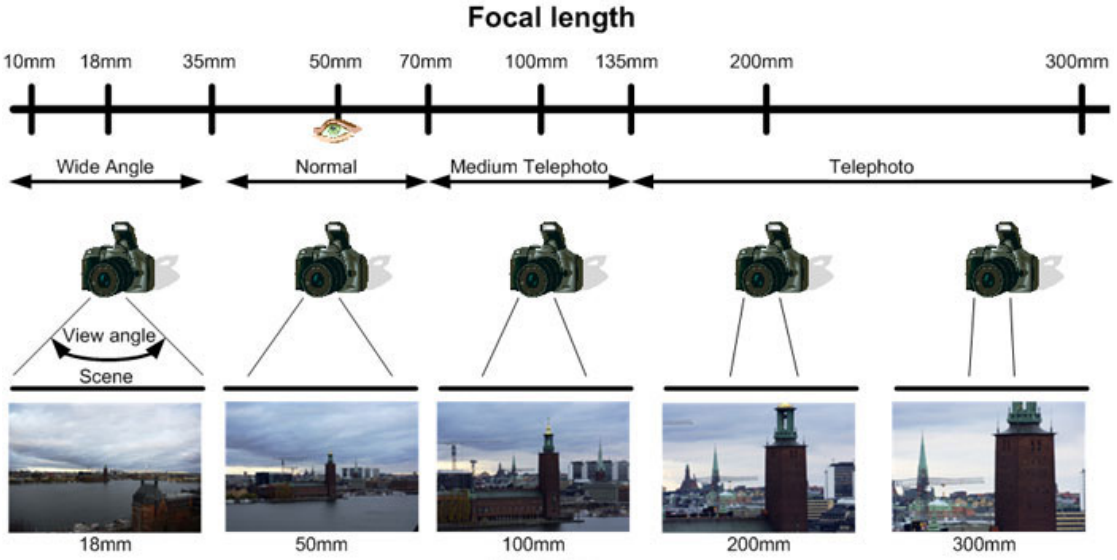

Figure 3.4.2: Influence of the focal length of the lens. The focal length of the lens determines the zoom ratio of photos. A lens with a bigger focal length is able to achieve a bigger zoom ratio (Wibowo, 2016).

Influences of focal length and f-number of a lens

The focal length of the lens fundamentally specifies how "zoomed in" the photos are; the bigger the number, the more zoomed the lens will be (figure 3.4.2). It is frequently taken amiss that the focal length is evaluated from the front of the lens. Actually it is the distance between the point of convergency in the lens to the sensor (figure 3.4.3).

The ideal method to figure out the aperture (f-number), is to imagine it as a handling for the eye pupil – the broader it becomes, the more light it takes in. The alteration in aperture diameter allows more or less light onto the sensor. Broader apertures allow more light and narrower apertures allow less light (figure 3.4.4). F-number is indicated by $f^{\#}$ and expressed as,

$$f^{\#} = \frac{f}{D} \ . \tag{3.4.4}$$

"A" is the area of the aperture and is computed by,

$$A = \pi \left(\frac{D}{2}\right)^2 \ . \tag{3.4.5}$$

It is easy to see that, the aperture area reduces by rising the f-number (figure 3.4.4).

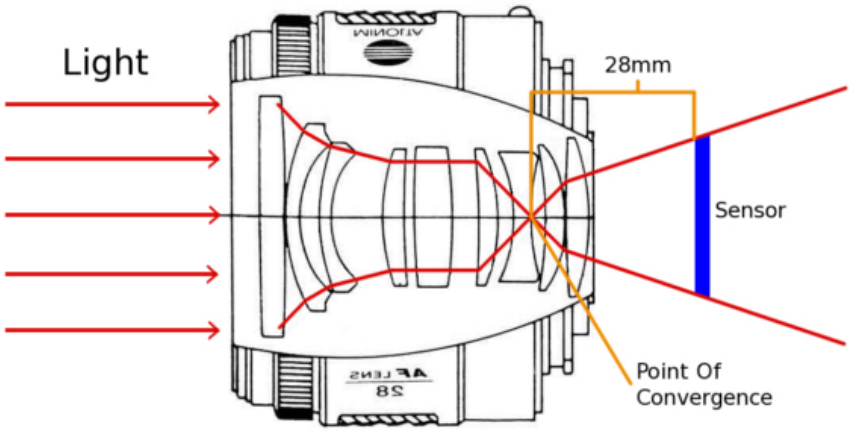

Figure 3.4.3: Lens configuration representing a focal length equal to $f = 28$ mm (Gauthier, 2017).

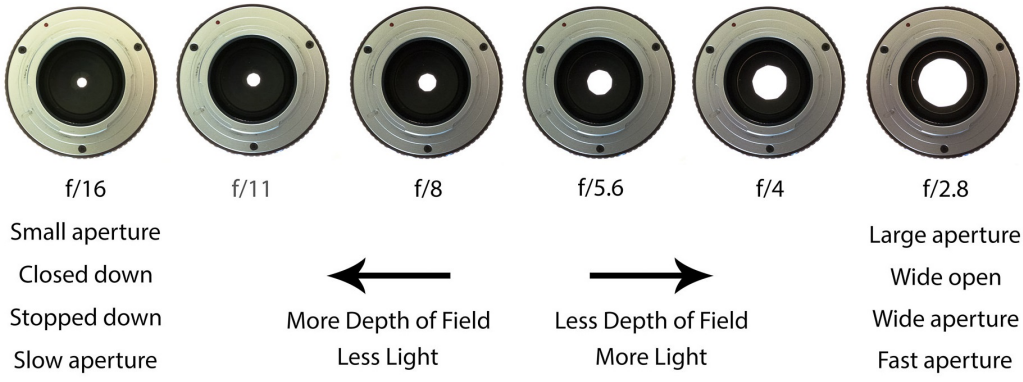

Figure 3.4.4: Aperture scale - some widespread terminology. Broader apertures let more light and narrower apertures let less light (Subratachak, 2018).

The size of a variance in aperture associates with the exposure: the broader the aperture, the more exposed the photo will be. One method to show this point could be achieved by shooting a series of photos in which aperture size is changing, while other parameters are fixed (figure 3.4.5).

In the next subsection we will give the rule to compute the depth of field.

Figure 3.4.5: The influence of the f-number. The broader the aperture, the more exposed the photo will be. Exposure increases with the increasing f-number (Amir, 2017).

3.4.2 Depth of field

A secondary significant relation covers the depth of field δz of the recording optics. The depth of field is the thickness of the field over which particles will be in appropriate focus (see figure 3.4.1) and expressed as,

$$\delta z = 4(1 + M^{-1})^2 \left(\frac{f}{D}\right)^2 \lambda \, . \tag{3.4.6}$$

Favorably, δz should not be lesser than the thickness of the laser sheet in order to prevent detecting out of focus particles.

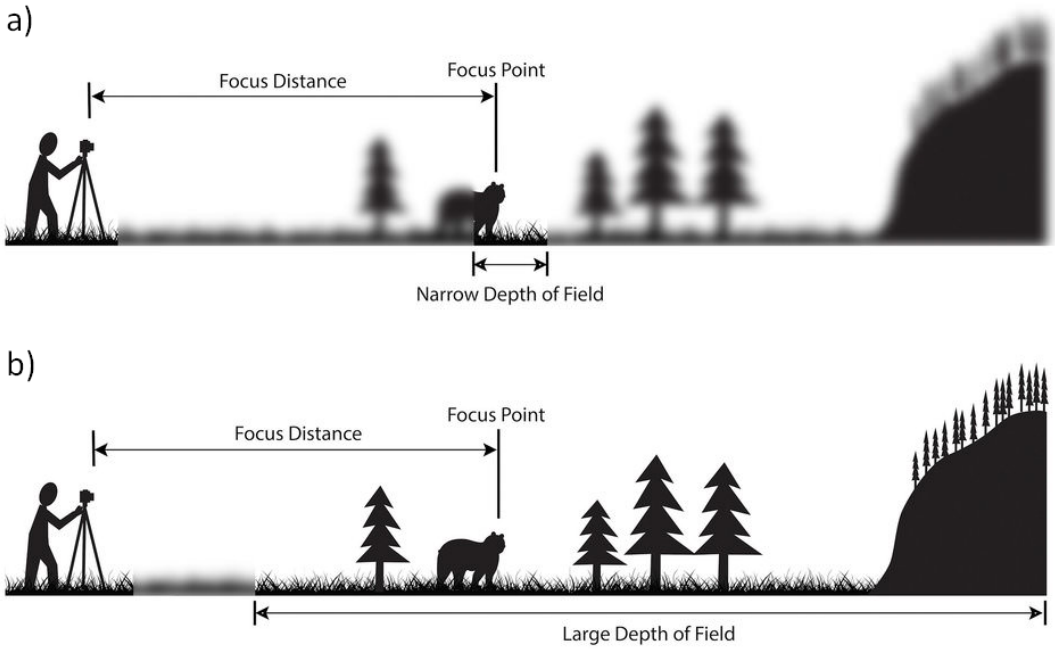

Figure 3.4.6: The effect of "depth of field". a) Only a small segment of the image is in focus with a narrow depth of field, b) Contrarily, with a grand depth of field, more of the scenery is sharp (Pajser, 2017).

Next, the creation of a light sheet will be discussed.

3.4.3 Creation of a light-sheet

The easiest technique to generate a light-sheet is to employ a cylindrical lens by combining with a spherical lens (figure 3.4.7). The cylindrical lens gives rise to the laser light to be widen in a single direction. The spherical lens gives rise to the widening light in order to focus throughout the normal direction. It is apparent in the figure 3.4.7 that the light-sheet keeps widening with a decreased ratio, in the downstream direction of the spherical lens; it is feasible with a reasonable selection of focal lengths to acquire a collimated light-sheet, e.g. the one which proceeds with a fixed height of beam H. That prohibits a rarefaction of the intensity of the beam with distance. The intensity of laser sheet is proportional to the power of laser and inversely proportional to H and Δz_0.

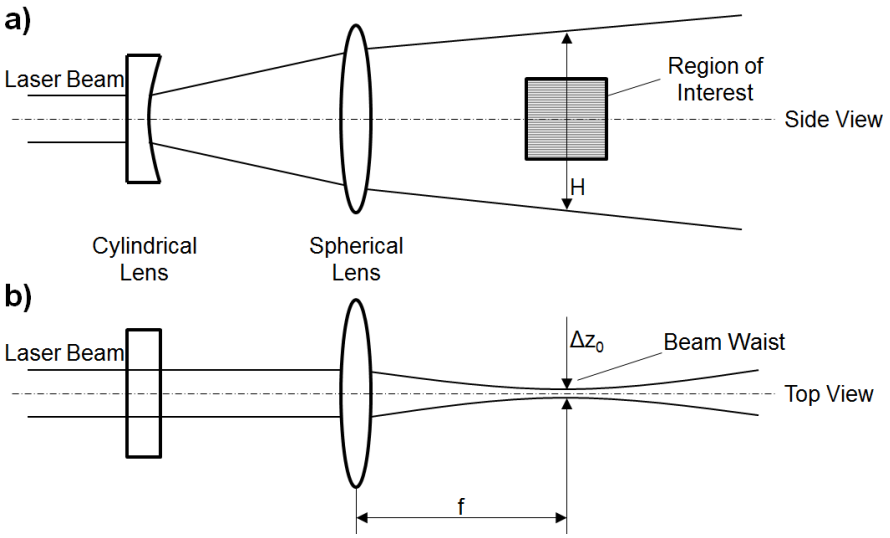

Figure 3.4.7: A diagram of a basic sheet forming module. a) side view, b) top view. Where Δz_o is the beam waist and f is the focal length of the spherical lens. Figure inspired by Prasad (2000a).

Optimizing the pulse separation is the subject of the next subsection.

3.4.4 Pulse separation

The particle image luminosity on the recording medium attains a saturation level when the particle moves more than a diameter throughout the exposure, because scattered light is transmitted over a bigger surface on the sensor. Therefore, it is not handy to raise the pulse period over a limit determined by the speed of the flow. When the pulse separation of the laser Δt is larger, the particle displacement ΔX is larger too. Then the difference between the measured velocity and the actual velocity is greater. The mentioned point proposes that the magnitude of Δt should be decreased. Nonetheless, if we decrease Δt so much, the measurement of ΔX gets rough; for very small values of Δt, it shall be impossible to set apart ΔX from a random error. The optimal pulse separation was derived by Boillot and Prasad (1996) as,

$$\Delta t_{opt} = \sqrt{\frac{2\sigma_{random}}{Ma}} = \sqrt{\frac{2cd_e}{Ma}} \ . \tag{3.4.7}$$

Here, d_e is the effective particle image diameter, and c is a constant value between 0.05 and 0.10 depending on empirical circumstances. The local acceleration of the particle, a, can not be known till the flow is measured. Consequently, a two step measurement may be necessary, where the initial measurement is handled with an estimated Δt for determining the value of a, subsequent to a secondary measurement with an optimized Δt. It should be mentioned that not all domains of a flow field have the same value of a, therefore, a further optimization could be essential.

3.5 Image capturing

The PIV recording techniques are categorized into two primary groups (Adrian, 1991):

1. single frame / multi exposure PIV,
2. multi frame / single exposure PIV.

The first method, with no further struggle, does not maintain any information on the temporal sequence of the laser pulse causing to an uncertainty in the displacement vector. Contrary, "multi frame / single exposure PIV" method naturally maintains the temporal sequence of the images of particles and therefore is the technique of preference if the technological necessities shall be provided (Jahanmiri, 2011).

3.6 Phase discrimination for PIV in multiphase flows

PIV is a useful tool for the visualization of flow problems. The classical approach in PIV techniques is seeding the flow with tracer particles, which faithfully follow the flow. One is able to map the flow velocity field by detecting the tracer particles with the help of PIV instruments.

Stokes number of a particle in a flow is defined by

$$St = \frac{\tau_p}{\tau_\eta} \ , \tag{3.6.1}$$

where τ_p is the relaxion time of the particle and τ_η is the kolmogorov time scale (Sabban et al., 2017). The definition of τ_p was given in the equation (3.3.8).

Particles having small Stokes number tracks the flow streamlines. Particles with large Stokes number are dominated by their inertia and proceed throughout their initial trajectories.

The main interest of PIV in multiphase flows is observing the interactions between the fluid and the inertial particles. Therefore inertial and tracer particles must be distinguished by using some advanced techniques in PIV. Two main techniques were emphasized by Merzkirch et al. (1997) as the following.

3.6.1 Seperation of scattered light from different objects

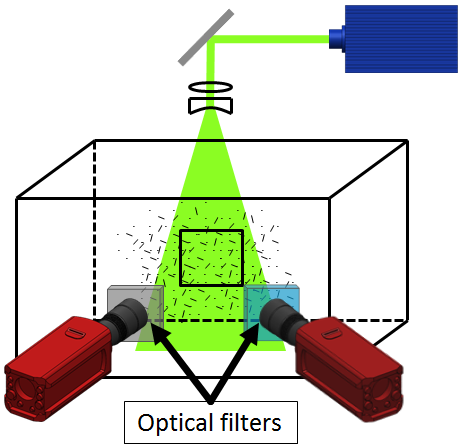

Figure 3.6.1: Depiction of an optical filter. Different wavelengths of light scattered by different particles can be distinguished by using optical filters in front of a camera. Figure inspired by Lindken and Merzkirch (2002).

This technique focuses on the wavelength properties scattered from different objects. Wavelength of the light scattered from the fluorescent tracer particles are different from the inertial particles. In this method one can use color coding for the cameras during the recording and be able to distinguish the light scatterd from different objects. Another option is to use optical filters selected in accordance with the fluorescence wavelength and employ it before a black and white camera (figure 3.6.1).

3.6.2 Digital mask technique

Another method to distinguish the scattered light was mentioned in Gui and Merzkirch (1996). This method uses a technique called digital masking and it is feasible when different particles have a remarkable variation in the size dispersion.

Digital Mask Technique was applied on the analysis of single-camera, double-pulse PIV experiment by Dearing et al. (2013). Scanning of the fibers and flow was obtained with an visualization system including a pulsed Nd: Yag laser with a wavelength of $\lambda = 524$ nm. Thickness of the laser sheet was set to 1 mm by means of laser sheet optics. A Nikon lens with $f = 504$ mm and $f^{\#} = 1.4$ was mounted on a PCO Sensicam camera with a $1,280 \times 1,024$ resolution with a frame catcher and a computer to store and analyze the obtained images. The experimental efforts were performed with the bulk Reynolds number equal to $Re = 8043$. The diameter of the tracers (hollow glass spheres) were 20 μm, mean length and diameter of fibers were respectively 320 μm and 24 μm.

In the pre-processing background noise of the images were removed by applying the following process: initially the intensity of the images was calibrated so that 1 percentage of the pixels were saturated at the bottom and peak intensities of the raw image. The contrast of the processed images were incremented in this way and the inertial particles show up more luminous. Secondly, by means of a 3×3 pixels median filter the high frequency noise was removed. Bigger sized filters offer a filtering on the images of the tracer particles with the lack of pronounced benefits to clear noise. Last step is the binarization of the images. In this step, each pixel with an intensity level above 230 was regulated to maximal value of 255. Contrary, the pixels beneath this level were regulated to zero. When binarization of the images was completed, phase separation was able to be accomplished.

During the phase separation, a threshold for the aspect ratio was set to eliminate the particles with the aspect ratio beneath 1.5 to detect the inertial particles. The particles with the length, l, above a threshold $l^* > 1/7\ l$ were identified as fibers.

Some figures showing the preprocessing and phase separation process are demonstrated in figure 3.6.2. Figure 3.6.2.a demonstrates an original image of 140×200 pixels. The tracers and inertial particles are observable. Figure 3.6.2.b is the consequence of the binarization and filtering process exerted on the original image. Figure 3.6.2.c depicts inertial particles (fibers) based on the described criterion about size and aspect ratio. In order to measure the velocity field of tracer particles, images of fibers were subtracted from the intensity adjusted images (figure 3.6.2.d). That leaded the analysis of velocity field with discarded vectors as in the figure 3.6.2.e. By adjusting the correlation peak ratio, the whole velocity field of the measured domain was obtained (figure 3.6.2.f).

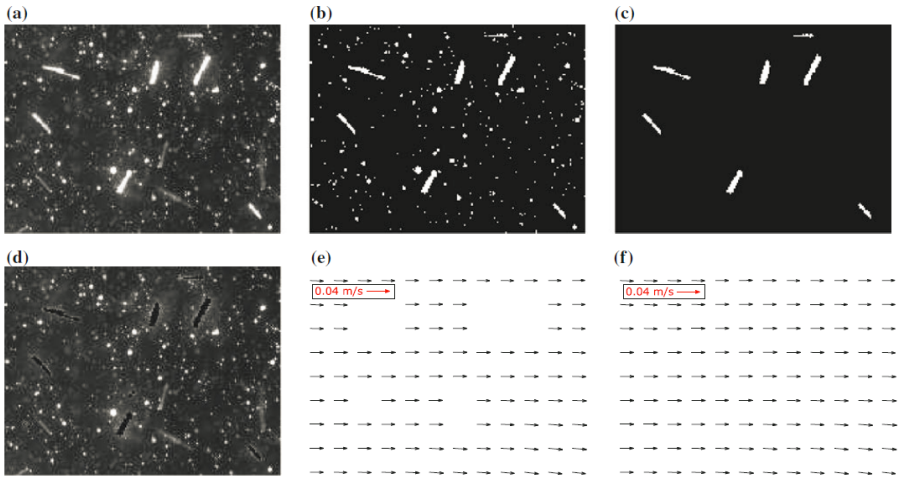

Figure 3.6.2: Steps of image-processing algorithm: a) a raw image of 140×200 pixels, b) binarization and filtering application on the raw image, c) discrimination of fibers from the seeding particles, d) only the seeding particles, e) PIV analysis of only seeding particles when the correlation peak ratio is below 4, f) obtained vector field when the correlation peak ratio is 3 (Dearing et al., 2013).

4. Design of the test section

In this chapter, required information for designing the proposed test section will be considered. First, the optimization procedures provided in the section 3.4 will be checked up by reviewing the literature. Second, a comparison of PIV techniques, explained in section 3.2, will be done in order to choose the most suitable PIV technique for the experiment. Third, the necessary computations will be given in detail for the data optimization of the test section. Finally, a discussion about the optimal PIV setup will be done and a flowchart will be suggested in order to perform the experiments time efficiently.

4.1 Literature review

In this section, different experimental setups exist in the literature will be analyzed in order to examine the structure of the test section. Optimization rules in section 3.4 were considered during the reconstruction of the test sections.

4.1.1 Configuration 1: Cole et al. (2016)

In this experiment, orientation and rotation rates of 3D-printed anisotropic particles were examined by a 3D-PTV technique. An octagonal tank was considered as a test section (figure 4.1.1.a). Two oscillating grids were employed to generate turbulence inside the tank. A volume was illuminated inside the tank by splitting the laser beam by means of a beam splitter. Right and bottom mirrors were used for the orientation of the laser beam, left and top mirrors were used for the amplification of the light intensity (see figure 4.1.1.b). Four cameras were used to detect the illuminated volume and get 3D data of the anisotropic particles.

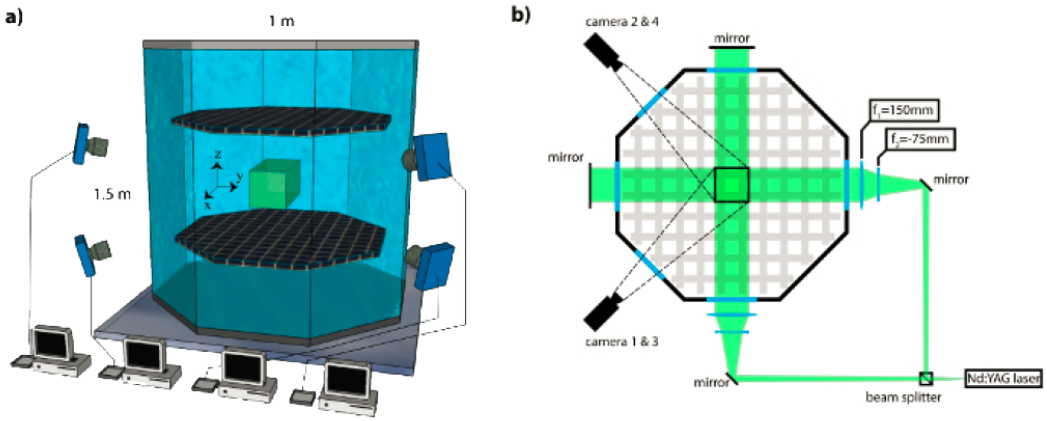

Figure 4.1.1: The experimental setup of Cole et al. (2016). Two oscillating grids were used to create turbulence inside of the tank. The central volume represents the volume of interest illuminated by the laser. a) Side view of the test section showing the positions of the cameras and the connections between the computers. b) Top view of the test section showing the configuration of the mirrors, laser and lenses mounted to the cameras.

The parameters from Cole et al. (2016) were used to obtain the experimental configuration. Particle size is given as, $d_c = 0.3$ mm, $l_c = 3$ mm. The volume-equivalent spherical diameter

was given by Bordoloi and Variano (2017) as the following:

$$d_{eq} = (d_c^2 l_c)^{1/3} \ . \tag{4.1.1}$$

The equivalent diameter was computed as, $d_{eq} = 0.52$ mm. Object distance and focal length were given as $d_o = 500$ mm, $f = 200$ mm respectively. From equation (3.4.1) the magnification was found as, $M = 0.67$. Lens aperture was given as, $f^{\#} = 11$. The wavelength of laser light was assumed to be, $\lambda \approx 532$ nm in the computations. By using equations (3.4.2) and (3.4.3), $d_s = 1.73 \times 10^{-5}$ m, $d_e = 4.3 \times 10^{-4}$ m. In this case $Md_p \approx d_e$, which is consistent with the optimization procedures. A big lens aperture was used to detect the whole illuminated volume ($3 \times 3 \times 3\ cm^3$) with a cost of blurry pictures.

Cameras are capable of at least 1 megapixel resolution at 450 frames per second. Under given optical considerations it can be suggested that, a camera with 1 megapixel is sufficiently enough to resolve particles with $d_{eq} \approx 0.52$ mm. Pulse frequency of the laser is 900 Hz, which is 2x of the frequency of the camera.

4.1.2 Configuration 2: Bordoloi and Variano (2017)

Rotational kinematics of large cylindrical particles in homogeneous isotropic turbulence were examined in this experiment. Two 8×8 pump arrays were used for creating homogeneous isotropic turbulence inside the test section. A stereoscopic camera arrangement were considered as the PIV technique to obtain 3D velocity data. Thickness of the light sheet is 1 mm, lenses were mounted on both cameras using a Scheimpflug adapter in order to keep the region of interest in focus for both cameras. Two prisms were used to minimize the refraction effects (figure 4.1.2).

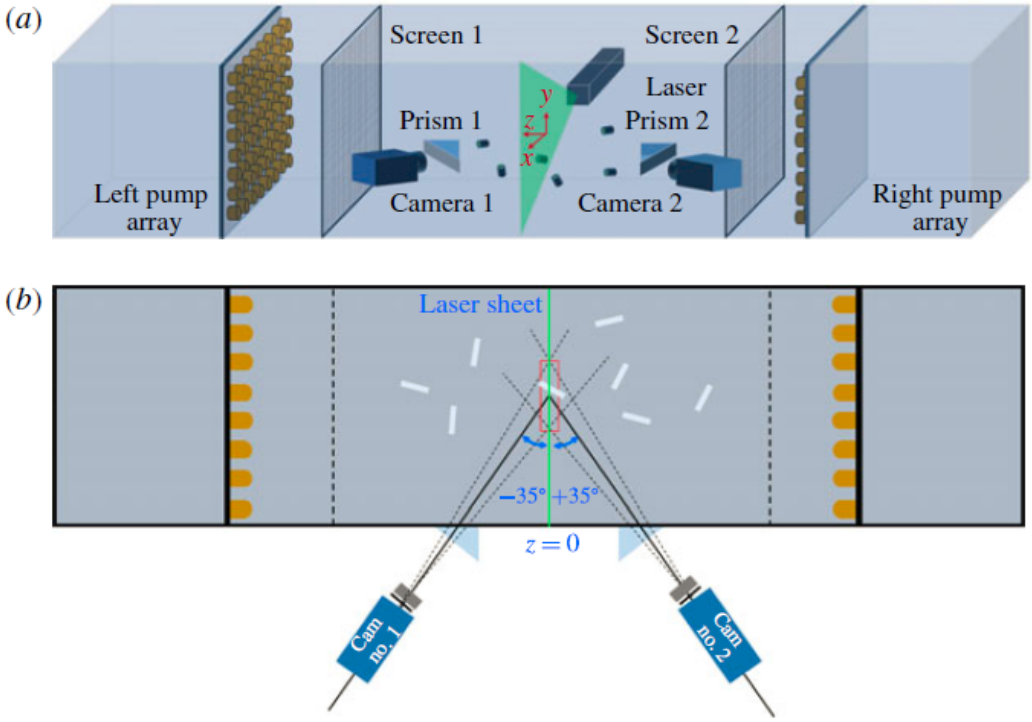

Figure 4.1.2: The experimental setup of Bordoloi and Variano (2017). a) 3D sight indicating the tank, two jet arrays, light-sheet, cameras and prisms; b) Top view indicating the SPIV setting.

The parameters from Bordoloi and Variano (2017) were used to obtain the experimental configuration. Particles with different sizes were used during the experiments. The smallest particle, $d_{eq} = 16\eta = 4.8$ mm (η is given as 0.03 x 10^{-2} m) was considered for the reconstruction of the experiment.

Two CCD cameras with 1600 pixels x 1200 pixels were used in the experiment. The image pairs were collected at a frame rate of 14 Hz, with a pulse seperation of 6 ms. A "multi frame / single exposure PIV" method is sufficient for the given frequency (figure 4.1.3).

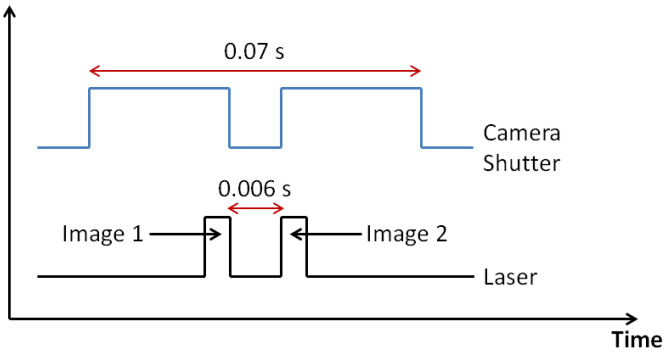

Figure 4.1.3: A schematic of a "multi-frame/single exposure PIV", with the values used in the PIV experiment by Bordoloi and Variano (2017).

For the given pulse frequency (167 Hz) and lateral velocity scale (0.0191 m/s) a tracer particle (13-44 μm) will horizontally travel 0.114 mm in a light sheet with 1 mm thickness, which is respectively 8.8 and 2.6 times the given diameters of the tracer particles.

Focal length, f, of the lens is 85 mm. Assuming that the working distance is 200 mm, from equation (3.4.1) it is found that the magnification is 0.74. By using equations (3.4.2) and (3.4.3), magnification was found as, $Md_p \approx d_e = 0.481$ mm. From equation (3.4.6) the light sheet thickness was found as $\delta z = 1.4\ mm > 1\ mm$, which agrees with the optimization procedures.

4.1.3 Configuration 3: Sabban et al. (2017)

Planar time resolved PIV measurements were exerted in order to classify the flow characteristics, perceive the turbulence kinetic energy dissipation rate and examine fibre alignment with the flow. An octagonal tank was considered as a test section. Homogeneous isotropic air turbulence was generated by means of four woofers attached to the walls of the tank (figure 4.1.4). A high speed Nd:YLF laser and a CMOS camera were equipped in the experimental setting.

The parameters from Sabban et al. (2017) were used to obtain the experimental configuration. Field of view (FOV) is given as 6.3 x 12.6 mm^2(aspect ratio 1:2). A CMOS camera with 512 x 1024 pixels (aspect ratio 1:2) at 3 kHz and a high speed laser (NewWave Pegasus, 527 nm, 10 mJ $pulse^{-1}$) were used during the experiments. In this case, the frequency of the laser is given as 1 kHz in the catalog of the laser, which is a typical data frequency proposed by Raffel et al. (2007). A long-distance microscopic lens was mounted to the camera but no data about the lens were given in the paper. Therefore it is not possible to consider the optimization procedures for the lens.

4.1.4 Configuration 4: Sabban et al. (2017)

In this setup, 3-dimensional translational and rotational kinematics of the fibers were observed from two perpendicular directions by digital holographic cinematography at an acquisition rate roughly five times of the frequency of the Kolmogorov time scale. The test section is identical to the configuration 3 discussed above. The laser beam was splitted by means of a beam splitter for illuminating a volume of interest (VOI) in the middle of the test section (figure 4.1.5). Two CMOS cameras obtained the 3D velocity data from the illuminated volume.

The parameters from Sabban et al. (2017) were used to obtain the experimental canfiguration. The volume of interest, i.e. the intersection of the two orthogonal views, was approximately 17 x 17 x 17 mm^3 located at the centre of the turbulence chamber. The dimensions of the fibers are. l_c = 0.5 mm, d_c = 13.7 and 19.1 μm. No lens for the cameras were used. The spatial measurement resolution of the camera was given as 17μm, which is equal to the square pixel size. Therefore it was insufficient to resolve d_c but sufficient to resolve l_c. Two high speed CMOS cameras (1024 x 1024 pixels at 2 kHz) were used in the experiment. In total 8 data sets were acquired for each $dtex$ value (fibres were characterized by their mass density in units of $dtex = \pi\rho D^2/4 \times 10^{-7}$ g per 10000 m) at an acquisition frequency of f = 2 kHz, resulting in 4096 holograms (2048 for each camera) per data set. The high speed lazer, which is capable of working at 10 kHz (10 μJ $pulse^{-1}$) is sufficiently enough to keep up with the frequency of data obtained.

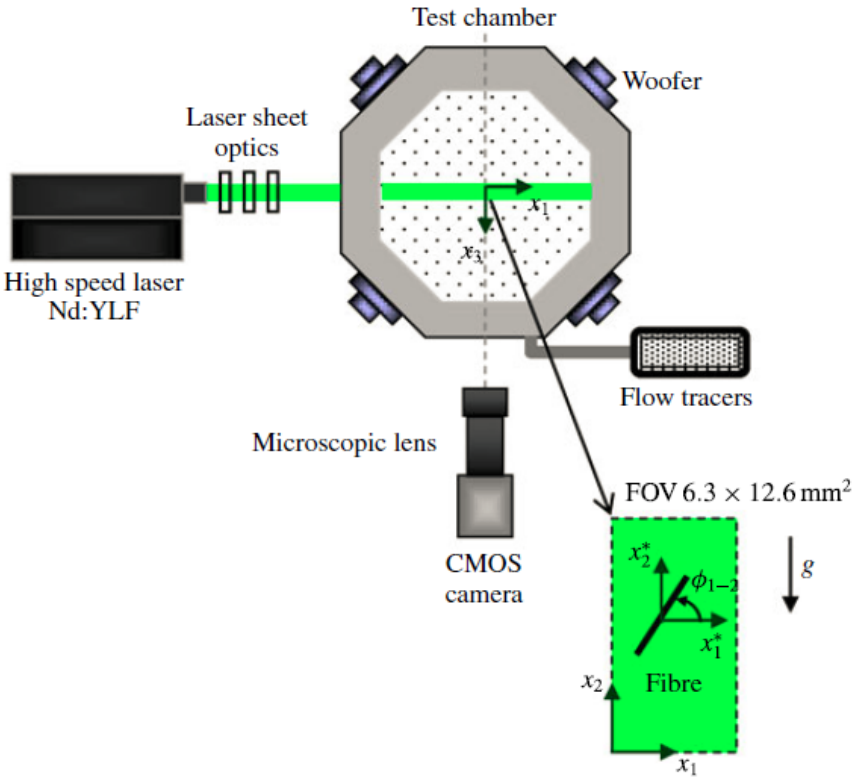

Figure 4.1.4: The experimental setup of Sabban et al. (2017). The schematic indicates the time resolved PIV setup of the experiment.

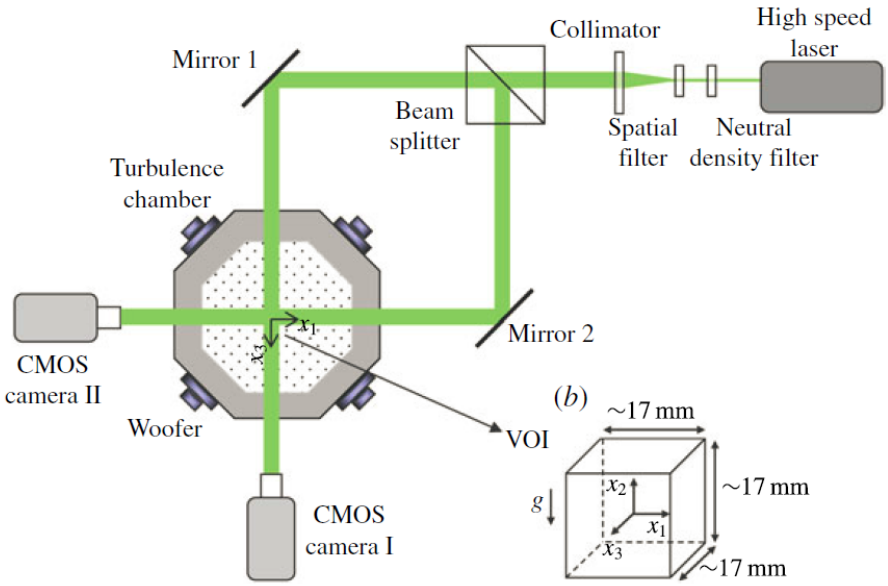

Figure 4.1.5: The holographic setup of Sabban et al. (2017). The schematic indicates the HPIV setup of the experiment. The laser beam is splitted by means of a beam splitter in order to illuminate $17 \times 17 \times 17mm$ volume in the middle of the test section.

The data discussed above are summarized in the table 4.1.

Experiments	**Config. 1**	**Config. 2**	**Config. 3**	**Config. 4**
d_c	0.3 mm			13.7 and 19.1 μm
l_c	3 mm			0.5 mm
d_{eq} eq. (4.1.1)	0.65 mm	4.8 mm		
d_p		13 -14 μm		
d_o	500 mm	200 mm (assumption)		
f	200 mm	85 mm		No lens
$f^{\#}$	11			No lens
M eq. (3.4.1)	0.67	0.74		No lens
λ	532 nm		527 nm	
d_s eq. (3.4.2)	2.38×10^{-5} m			
d_e eq. (3.4.3)	3.49×10^{-4} m	0.481 mm		
Md_p	3.48×10^{-4} m	0.481 mm		
δz eq. (3.4.6)		1.4 mm		
Δz_o		1 mm		
Lateral Velocity		0.0191 m/s		
FOV	$3 \times 3 \times 3$ mm^3		6.3×12.6 mm^2	$17 \times 17 \times 17$ mm^3
Type of Cameras			CMOS	CMOS
Camera Resolution	1024×1024	1600×1200	512×1024	1024×1024
Camera Frequency	450 Hz	28 Hz	3 kHz	2 kHz
Laser Frequency	900 Hz	167 Hz	1 kHz	10 kHz
Laser Energy per Pulse			10 mJ	10 μJ

Table 4.1: Summary data of the PIV experiments.

4.2 Comparison of PIV techniques

PIV technique was introduced as a high spatial measurement technique. But the technological improvements allowed additional temporal resolution to PIV systems. As seen in the figure 4.2.1 TPIV and SPIV techniques are suitable for high speed PIV applications.

As mentioned in section 3.2, SPIV and DSPIV systems perform the measurement on a plain, TPIV on a volume. Therefore, a complete topological information of a 3-dimensional volume can be obtained by a TPIV system. TPIV is a defocus technique therefore ghost particles are one of the main problems of TPIV systems. Typical camera number for a TPIV system is considered to be four (see table 4.2) but increasing the camera number to six will decrease the number of ghost particles and possible measurement errors in return.

Table 4.3 depicts the possible errors for different PIV techniques. The accuracy of the measurements is restricted by diverse origins of systematic and random errors. Systematic errors are mostly minor, in the order of a few tenth of a pixel (Michaelis and Wieneke, 2008). The errors may have a significant effect on the velocity range of the measurements. TPIV maintains the third dimension additionally and it is not affected by most of the systematic errors. Nevertheless ghost particles are specific errors for TPIV systems.

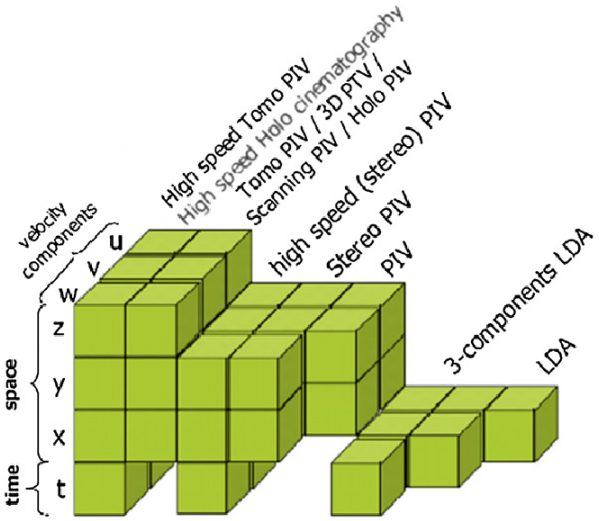

Figure 4.2.1: Measurement domain and measured components of laser velocimetry methods. Temporal resolution is possible with high speed applications of TPIV and SPIV techniques (Scarano, 2012).

	2D PIV	SPIV	DSPIV	TPIV
Measurement domain	2D planar	2D planar	2 × 2D 2 × planar	3D volumetric
Measured velocity components	2C	3C	3C	3C
Cameras	1	2	4	4 (3-6)
Double pulse laser	1	1	1-2	1

Table 4.2: Properties of different PIV systems. SPIV, DSPIV and TPIV are able to get 3-velocity components. TPIV is able to detect a 3-dimensional volumetric domain (Michaelis and Wieneke, 2008).

	2D PIV	SPIV	DSPIV	TPIV
Loss of particles	yes	yes	yes	no
Stereo error: different particles in interrogation windows of camera 1 and 2	-	yes	yes	-
Particle intensity variation due to laser sheet profile	yes	yes	yes	no
Sensivity to background noise and contamination of optical components	very high	high	high	low
Smearing of correlation,peak by out of plane velocity gradients	yes	yes	yes	no
Specific errors	Only 'projection' of vectors		Misalignment of laser planes	Ghost particles

Table 4.3: Systematic errors of PIV systems. Number of ghost particles effect the accuracy of measurements. Misalignment of the laser sheets may cause some specific errors in DSPIV measurements. Most of the errors for planar measurement techniques can be hindered by following the optimization rules (Michaelis and Wieneke, 2008).

Despite the sophisticated calibration procedures of TPIV (Geisler et al., 2014), setup of a TPIV system is very easy, quality checks shall be instantly made. High spatial resolution and time-resolved measurements put TPIV forward as a method capable of measuring 3-dimensional structures in small scales in turbulence (Schäfer and Schröder, 2011).

	CONS	PROS
SPIV	Lack of x-axis components of the velocity gradient tensor Complete visualization of vortex structures isn't possible 2D measurement domain	Low experimental complexity Low costs High speed application is possible
DSPIV	Medium experimental complexity Medium costs Complete visualization of vortex structures isn't possible Low temporal resolution 2D measurement domain	Whole components of the velocity gradient tensor
XPIV	High experimental complexity High costs Complete visualization of vortex structures isn't possible Low temporal resolution	Whole components of the velocity gradient tensor 3D measurement domain
HPIV	Medium experimental complexity Relatively small detection volume Medium costs Low temporal resolution Suitable just for simple flow configurations	Whole components of the velocity gradient tensor 3D measurement domain
TPIV	Medium experimental complexity Medium costs Long duration of digital processing Big size of the stored data	Whole components of the velocity gradient tensor Complete visualization of vortex structures is possible 3D measurement domain High speed application is possible
V3V	No flexibility in the camera configuration Low temporal resolution Not enough information in the literature	Whole components of the velocity gradient tensor Complete visualization of vortex structures is possible 3D measurement domain Possibility of relatively higher seeding concentrations

Table 4.4: Comparison of suitable PIV techniques to obtain 3-velocity components (Schroeder and Willert, 2008; Pothos et al., 2009).

4.3 Data for the design of the test section

A turbulent flow in a rectangular channel is the main subject of the proposed experiment. Dimensions of the rectangular section of the channel are given as $a = 0.3\ m$ and $b = 0.1\ m$. By using the data in table A.1 in "Appendix A", we obtain the hydraulic diameter $D_H = 0.15\ m$.

Reynolds number of the flow is given as $Re = 100000$. Velocity of the flow can be computed from

$$u = \frac{Re\ \nu}{D_H}\ . \tag{4.3.1}$$

The velocity is computed as $u = 0.6682\ m/s$. The region of interest is considered to be approximately $6 \times 6\ cm^2$. Typical seeding materials for liquid flows are listed below.

Type	Material	Mean diameter [μm]
Solid	Polystyrene	10 - 100
	Aluminum	2 - 7
	Glass spheres	10 - 100
	Granules for synthetic coatings	10 - 500
Liquid	Different oils	50 - 500
Gaseous	Oxygen bubbles	50 - 1000

Table 4.5: Seeding materials for liquid flows (Raffel et al., 2007).

Following calculations were performed under the assumption of seeding particles as glass spheres with $20\mu m$ diameter.

Sabban et al. (2017) used flow tracers of Glycerine BP/purified water mixture with $0.2-0.3\mu m$ diameter in an air flow. Bordoloi and Variano (2017) used glass spheres with $13-44\mu m$ diameter to visualize the flow seeded with inertial particles having the size $d_{eq} = 16\eta, 27\eta$ and 67η. Here d_{eq} is the diameter of a sphere whose volume is equal to that of the particle (see equation (4.1.1)) and η is the Kolmogorov length scale. Flow seeding was attained by Dearing et al. (2013) with $20\mu m$ diameter hollow glass spheres in a pipe flow with Reynolds number equal to $Re = 8.043$.

A seeding particle with 20 μm diameter and $\rho_p \approx 1003\ kg/m^3$ will have a relaxion time equal to $\tau_p = 2.2 \times 10^{-5}\ s$ (see equation (3.3.8)). In this case, Stokes number of the particle is $St \ll 1$ by means of the equation (3.6.1). It is mentioned by Raffel et al. (2007) so that, the diameter of the particles should be very small in order to ensure good tracking of the fluid motion. On the other hand, the particle diameter should not be too small as light scattering properties have also to be taken into account.

In the images, the luminosity of particles on the camera attains a saturated level if the travelling of particles exceeds one diameter throughout the exposure. Accordingly, one should not raise the pulse period past a restriction specified by the speed of the flow (Prasad, 2000a). Therefore the pulse duration of the laser is computed as $d_p/u = 20^{-5}/0.6682 = 2.99 \times 10^{-5}\ s$.

Pulse seperation of the laser shall be computed by the equation (3.4.7), but because of the unknown experiment parameters it is not possible to compute the necessary frequency of the laser with this equation. Another rule to estimate the frequency of the laser is given by Lu and Sick (2013). One particle should not travel more than 8 pixels in an interrogation window of 32×32 pixels. Therefore by using a camera with a pixel size of $20\mu m$, one can estimate the corresponding laser frequency approximately 1025 Hz for the given flow conditions.

Lasers with wavelength of $\lambda = 532\ nm$, light sheet thickness of $\Delta z_0 = 1mm$ and CMOS cameras with 1024×1024 pixels are very common in PIV applications.

The required magnification can be determined by the following equation (Lu and Sick, 2013):

$$\text{Magnification (M)} = \frac{\text{Length of the camera chip}}{\text{Corresponding length of the region of interest}}\ . \tag{4.3.2}$$

Therefore corresponding magnification will be computed as $M = 20.48/60 = 0.341$. The object distance can be computed for a 50mm lens by using the equation (3.4.1) as $d_o = 196.6$ mm. Setting a small aperture $f^{\#} = 2.8$ will keep the particles in the field of interest in focus.

Name	Value
D_H	0.15 m
Re	100000
u	0.6682 m/s
d_p	20 μm
τ_p	2.2×10^{-5} s
St	$\ll 1$
d_o	196.6 mm
f	50 mm

Name	Value
$f^{\#}$	2.8
M	0.341
λ	532 nm
Δz_0	1 mm
Pulse duration of laser	2.99×10^{-5} s
Frequency of laser	$\approx$ 1025 Hz
Type of camera	CMOS with 1MP res.
Frequency of cams	$\approx$ 3 kHz

Table 4.6: Data list for the design of the test section of the present experiment.

4.4 Identification of optimal PIV setup

Detecting the behaviour of anisotropic particles in a fully developed turbulence (Re = 100000), inside a channel with a rectangular cross section (30 mm $\times$ 10 mm) is the main goal of this experiment. Once a fully developed turbulence is obtained, a change in the velocity profile in the main flow direction is not expected (see figure 4.4.1). Therefore, the velocity gradient in the mean flow direction will be zero in theory. And practically, the velocity gradient in the main flow direction will be rather negligibly small.

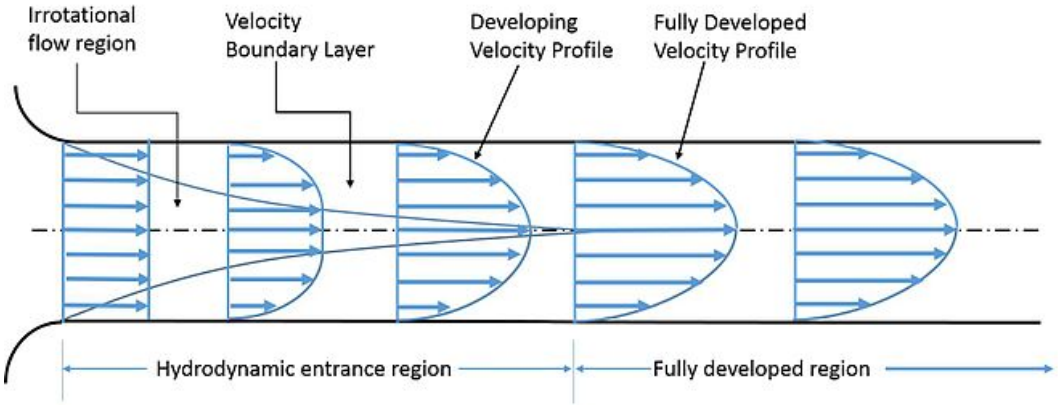

Figure 4.4.1: Evolution of the velocity profile inside a channel. Once a fully developed turbulence is obtained, a change in the velocity profile in the main flow direction is not expected (Yunus and Cimbala, 2006).

High velocity gradients occur in the high speed jet flows (Michaelis and Wieneke, 2008; Wernet, 2017) and the lack of determination of whole velocity gradient components may lead to big measurement errors in such conditions. Most of the data comparisons of different PIV techniques in the literature were implemented to evoke the systematic errors of the measurement techniques. Those errors are not related to the proposed experiment.

Another desired condition in the proposed experiment is to neglect the influence of the side walls. Neglecting the influence of the walls means, reducing the problem to a 2-dimensional flow under the assumption of having an infinite width of the rectangular cross section of the channel. One can align the light sheet in the main flow direction to achieve that condition as in the figure 4.4.2.

Obtaining the 3-velocity components with the complete nine components of the velocity gradient tensor is possible with HPIV, DSPIV, XPIV, TPIV and V3V. To the best of author's knowledge, an experimental application of the kinematics of anisotropic particles for DSPIV, XPIV, TPIV and V3V techniques does not exist in the literature. XPIV will not be considered because of the hard experimental efforts and high costs (Schroeder and Willert, 2008).

HPIV allows big obvervation volumes by constricting the experimental conditions in a serious way such as; particle concentration, reynolds number, flow complexity, temporal resolution, spatial resolution and laser light intensity (Schäfer and Schröder, 2011). Temporally resolved measurements of fibre kinematics in homogeneous isotropic turbulence within a small volume of

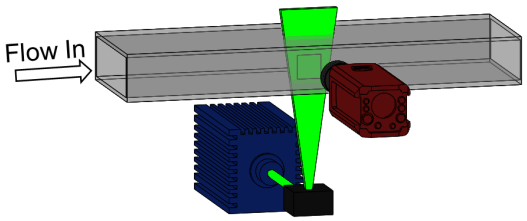

Figure 4.4.2: The best way to neglect the influence of the side walls. The light sheet should be alligned in the main flow direction in this way.

interest ($17 \times 17 \times 17\ mm^3$) were performed by Sabban et al. (2017). Limited experimental conditions maintained by HPIV technique don't meet the demands of the propsed experiment. Therefore it is not considerable.

TPIV and V3V are also suitable for volume detections. V3V offers a bigger ratio of "depth / width $\approx$ 0.75" (Pothos et al., 2009), while TPIV offers a typical ratio of "depth / width $\approx$ 0.25" (Jahanmiri, 2011). Short digital processing times for V3V technique were claimed by Pothos et al. (2009). Contrarily, a digital processing of a TPIV may even take weeks to months (Wernet, 2017).

DSPIV is convenient to obtain nine velocity gradient components but it is a planar measurement technique and complete visualization of 3-dimensional phenomena in a turbulent flow is not possible. DSPIV applications with one or two lasers are feasible. Polarization of light sheets and polarization tools for the cameras are required in case of one laser applications. The size of the particles inside the water is so crucial in this case. Big particles cause depolarization of the scattered light, which leads to big errors in the measurements (Wernet, 2017). This problem can be hindered by using smaller tracer particles but there is nothing to do with the inertial particles. Therefore a DSPIV setup with one laser is not suitable. At this point, an hypothesis to make a DSPIV system work for detecting anisotropic particles in turbulence will be offered. The reader should be warned about the fact that no such application exists in the literature, at least to the best of author's knowledge. The hypothetical setup is as the following: two distinct lasers with different wave lengths will be used to illuminate two region of interest inside the channel. Two pair of cameras will receive information from each region of interest by using color coding in the cameras or by using optical filters as explained in section 3.6.1. Separation of inertial particles and tracer particles will be obtained by digital mask technique (see section 3.6.2). This kind of setup will increase the costs and the experimental efforts will be rough. Any misalignment of the two laser sheets will cause significant errors (Michaelis and Wieneke, 2008).

SPIV is also another option to obtain 3-velocity components but with the lack of 3 components of velocity gradient tensor (see section 3.2.2). High velocity gradients will increase the measurement errors for a SPIV system (Michaelis and Wieneke, 2008). Such systematic errors in the proposed experiment are not expected due to the the low velocity gradients (see figure 4.4.1). DSPIV and TPIV systems are straight upgraded verisons of a SPIV system. Therefore a money spent to build a good quality SPIV system is never wasted.

It should be considered as an opinion to build a SPIV setup with the best quality instruments. As mentioned by Geisler et al. (2014), DSPIV and TPIV techniques are quite sophisticated and co-workers must gain some experience with simpler PIV setups in order to handle such advanced PIV techniques. Sophisticated calibration methods and hard experimental efforts of such advanced PIV techniques might lead inexperienced co-workers to come up with inaccurate experimental results. It is also a reality that advanced PIV techniques require more manpower. It would be wise not to waste too much money to build up an advanced PIV setup for the first stage. Here, in order to be able to obtain good experimental results, a time map is introduced:

1. First stage, duration: 2 months
    1.1. Build the hydraulic setup.
    1.2. Obtain the necessary instruments to build up a SPIV system.
2. Second stage, duration: 2 months

2.1. Reduce the problem to a 2-dimensional flow and set up a planar 2D2C PIV system (as in the figure 4.4.2).

2.2. Try to get comfortable with calibration techniques, PIV software program and laser-camera triggering systems.

2.3. Perform planar 2D2C PIV experiments for anisotropic particles and obtain statistical data.

3. Third stage, duration: 2 months

3.1. Set up a SPIV system and spend some time to calibrate two cameras properly.

3.2. Perform 2D3C PIV experiments for anisotropic particles and obtain statistical data.

3.3. Co-workers will gain enough experience to be able to operate advanced PIV techniques from this point on. It is possible to switch to a DSPIV or TPIV system by adding necessary additional components. It is optional to execute the same experiments further with an advanced PIV technique.

4. Fourth stage (optional), duration: 6 - 12 months

4.1. Switch the SPIV system to a DSPIV or TPIV configuration.

4.2. Now the co-workers should have enough experience to setup a DSPIV system and calibrate it properly. In case of a TPIV system, co-workers should spend some time to execute a volumetric calibration.

4.3. Perform the experiments with DSPIV or TPIV system and obtain statistical data for anisotropic particles.

4.4. Data analysis of a DSPIV will be much faster than a TPIV. Executing an experiment with TPIV will increase the data processing dramatically.

4.5. To make a good comparison of different PIV systems, all of the experimental conditions, except PIV techniques, must be kept constant.

5. All of those efforts can be completed within 12-18 months.

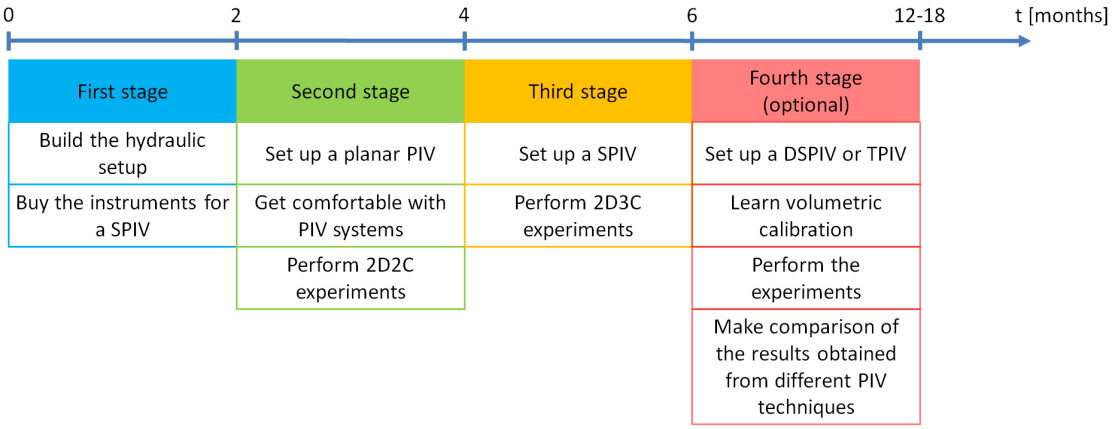

Figure 4.4.3: A flowchart suggestion for experimental progress. In the first two months requirements to perform the experiments must be met. After two months planar PIV technique should be applied. In the following two months SPIV technique should be applied. At the last stage, optionally, DSPIV or TPIV techniques can be applied.

5. Algorithm for the analysis of turbulent flows with PIV technique

In chapter 3 we have discussed about the main components of a PIV system, optimizing a PIV system, designing a test section and chosing an appropriate PIV technique for the test section. The cameras are responsible to obtain high quality images of the illuminated region of interest and transfer the obtained images to a computer, in order to analyse the velocity field of the flow by means of a PIV algorithm. The fundamentals of a PIV analysis is based on the correlation of the images provided by the cameras. The correlation methods will be described in the next section.

5.1 Correlation of the images

Auto-correlation and cross-correlation are the two correlation types used in PIV analysis (Bastiaans, 2000). The former type requires a "single frame / multi exposure" recording technique (for detailed information refer to section 3.5). In this technique, the particles are illuminated multiple times (mostly twice) during one shutter time (Prasad, 2000a). Consequently, in estimation of a auto-correlation, multiple peaks of the correlation of the displacements emerge, which leads to an uncertainty in the displacement directions. Besides, a centric self-correlation peak shows up. The self-correlation peak shall contain the displacement peaks for minor displacements. Those sequels create an issue to measure velocity fields, that lack an ascendant main direction of the flow.

The essentials of the correlation technique depend on maximizing the location of the peak value of the intensity levels of two discrete exposures. Therefore, it can be defined as a technique that measures the similarity between two images. For one dimensional case the value of the correlation function is computed as:

$$R(s_x) = \int I(x)I(x+s_x)dx \ , \tag{5.1.1}$$

where $I(x)$ refers to the intensity level of an image as a function of location and s_x is the displacement of the secondary image relative to the initial one. In case of auto-correlation method, the peak value of two identical exposures will be located at $dx = 0,\ dy = 0$. As seen from the figure 5.1.1, the peak value of the auto-correlation function can be found by sliding one of the images to left and right relative to the other one. As mentioned before, the peak value of the correlation function will be found at $dx = 0$ for two identical images for one dimensional case.

The latter type requires a "multi frame / single exposure" recording technique. In this technique, particles are illuminated just once for each shutter time. Therefore, image pairs are required in order to estimate the cross-correlation. No self-correlation is encountered in this technique and it lacks uncertainty in the displacement directions owing to the temporal sequence of the images. The advantages and disadvantages of both methods can be summarized as in the table 5.1. Usually the cross-correlation is a more common technique owing to the easy and effectual estimation method in benchmark with the auto-correlation technique. Besides as mentioned in table 5.1, auto-correlation has a decreased spatial resolution. The reason is that the image pairs possess larger information contents in contrast with single images. The only

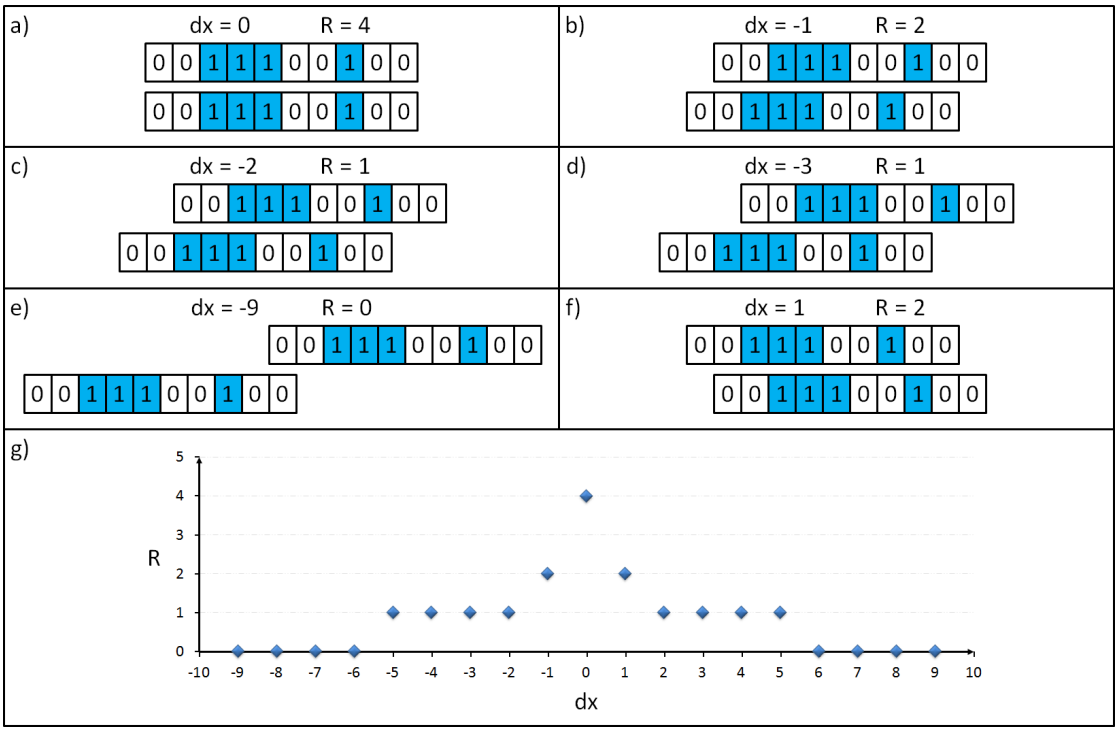

Figure 5.1.1: An auto-correlation process for 1D case. a-f) Values of the correlation function R are reported as a function of the displacement dx of the second image. The peak value of the correlation function is 4 and located at $dx = 0$ for the two identical images. g) The plot of displacements dx vs. corresponding correlation function values R.

Auto-correlation	Cross-correlation
Single frame	Multi frame
Multi exporuse	Single exposure
Directional uncertainty	Not
Problems with zero velocity	Not
Decreased spatial resolution	Not

Table 5.1: PIV analysis techniques. Auto-correlation requires a "single frame / multi exposure" recording technique but there arises an uncertainty in the direction of the displacement vectors. Cross-correlation requires a "multi frame / single exposure" recording technique. Uncertainty issues are irrelevant for this method (Bastiaans, 2000).

disadvantage of the cross-correlation is the requirement to obtain double images in too short temporal intervals. But the current CCD and CMOS cameras have too short shuttering times and with the double-pulsed high frequency lasers, this problem is not relevant anymore. The value of the cross-correlation function of an image pair for one dimensional case is defined as (Bastiaans, 2000),

$$R(s_x) = \int I_1(x) I_2(x + s_x) dx \tag{5.1.2}$$

where, I_1 and I_2 refer to the intensity levels of two distinct images. The cross-correlation acquires its maximal value when the two distinct images are lined up so that they possess the best similarity of their intensity levels. An illustration of a cross-correlation process was given in figure 5.1.2. The cross-correlation function gains its maximal value at $dx = -2$ by lining them up as in the figure 5.1.2.c.

In the following section we will discuss the main steps required to perform a PIV analysis.

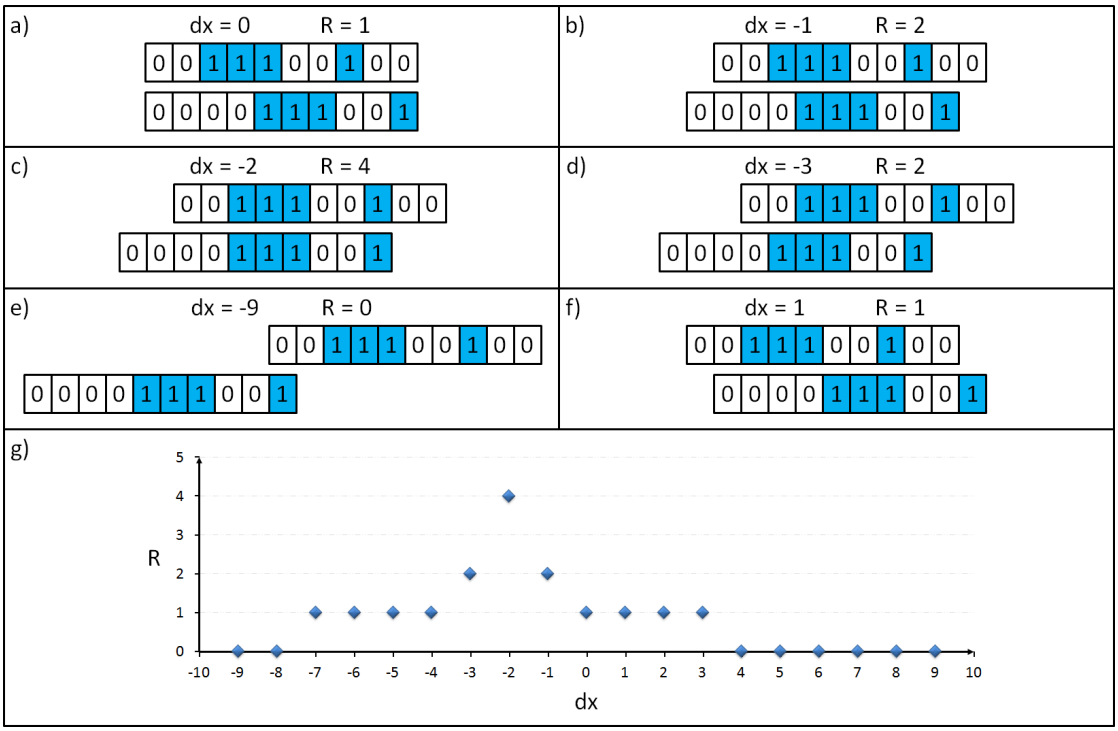

Figure 5.1.2: A cross-correlation process for 1D case. a-f) Values of the correlation function R are reported as a function of the displacement dx of the second image. The peak value of the correlation function is 4 and located at $dx = -2$ for the two distinct images. g) The plot of displacements dx vs. corresponding correlation function values R.

5.2 Flowchart of the algorithm

The course of an PIV algorithm is sketched in figure 5.2.1 in a generalized way. At least one pair of images is necessary in order to run the algorithm. We will explain the the process in detail in the following subsections.

5.2.1 Input data

This section of the algorithm includes reading the images and data information. Mainly, the information that have to be processed will be specified in the PIV programm by the user.

Read image files

Image pairs obtained by the cameras are transfered to a computer to perform a PIV analysis. The relevant information contained in the image are the resolution (number of pixels in each direction) and the intensity associated to each pixel. In order to obtain a single value of the intensity of each pixel, whether the image is grayscale-based or not, further operations may be required and will be described later.

Data information

Once an image pair is read by the PIV software, intensity level of each pixel is decoded for each image in order to apply the cross-correlation method. The simplest form of decoding the intensity levels is as in the figure 5.1.2. In this one dimensional example, the intensity distribution of each pixel was given as $I_1(x) = [0\ 0\ 1\ 1\ 1\ 0\ 0\ 1\ 0\ 0]$ for the first image and $I_2(x) = [0\ 0\ 0\ 0\ 1\ 1\ 1\ 0\ 0\ 1]$ for the second image. The pixels with ones can be considered as the intensity level of light scattered by the particles. The pixels with zeroes are considered to be dark. For real images, intensity is defined by three values, RGB, where R refers to the intensity level of red, G green, and B blue colors respectively. Those three intensity values should then be gathered in only one value in order to process the intensity distribution of images.

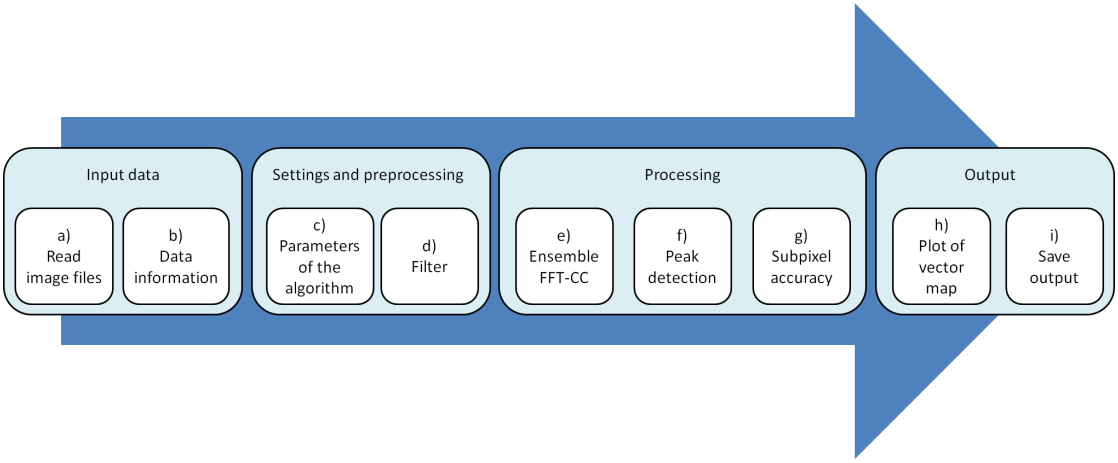

Figure 5.2.1: Flowchart of a PIV algorithm. a) A pair of images is read by the computer software, b) intensity levels of the images are identified by the software), c) the interrogation window size and the amount of overlap is identified, d) background is removed by filtering, e) Fast Fourier Transform (FFT) is applied for cross-correlation, f) Peak value of the correlation function is computed, g) An interpolation is applied for subpixel accuracy, h,i) output data are saved.

5.2.2 Settings and preprocessing

The second main section of the algorithm includes the choice of the parameters of the algorithm and filtering sections. Interrogation window size, overlap ratio and removing the background will be executed here.

Parameters of the algorithm

The parameters of the algorithm include the interrogation window size and overlap ratio in x and y directions. Before the PIV analysis each image is divided into subwindows. Those subwindows are called interrogation windows (figure 5.2.2). Each interrogation window at $t = t_0$ will be correlated with its equivalent window at $t = t_0 + dt$. In most of the PIV analyses an interrogation window size of 32×32 pixels is used (Prasad, 2000a).

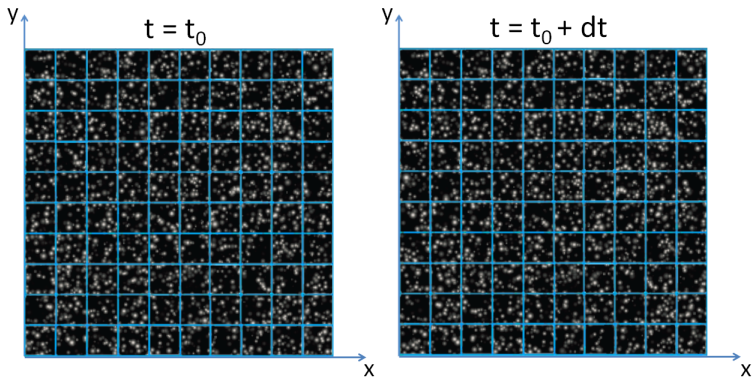

Figure 5.2.2: Interrogation windows. Each interrogation window at $t = t_0$ will be correlated with its equivalent window at $t = t_0 + dt$. An interrogation window size of 32×32 pixels is very common in PIV analyses.

Another parameter defined in PIV analyses is the overlap ratio. Consider the interrogation window highlighted by a blue transparent square at $t = t_0$ as in figure 5.2.3. According to the speed of the particles, the ones located close to the boundaries of the interrogation window might be found in an adjacent interrogation window at $t = t_0 + dt$. Therefore some particles might be lost in this case. To fix the problem, we expand the boundaries of the search area at the instant $t = t_0 + dt$ by means of an overlap ratio. In figure 5.2.3 an overlap ratio of 0.5 was chosen. This

ratio is very common in most of the PIV analyses (Prasad, 2000a).

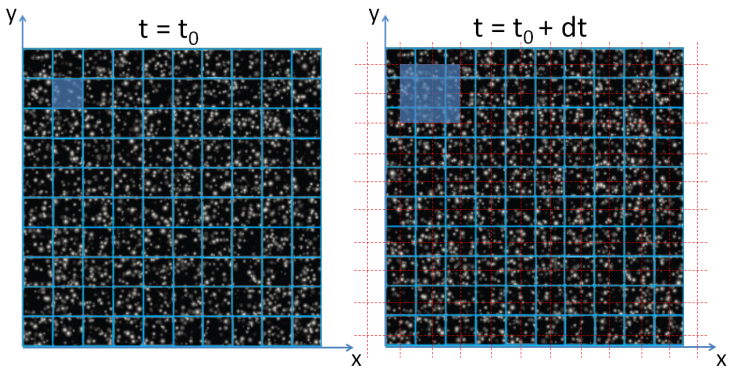

Figure 5.2.3: A presentation of overlapping. In order to prevent the loss of particles at an instant $t = t_0$ an overlap ratio is applied to the image at $t = t_0 + dt$. The boundaries of the search area is expanded by means of an overlap ratio.

Filter

Now let's consider a pair of images of the selected interrogetion window. When there is no particle motion, the correlation function will have an obvious peak in the auto-correlation map as in the figure 5.2.4. This reason can be exemplified with the figure 5.1.1. The correlation function of two identical images gains its peak value at the center point of the image.

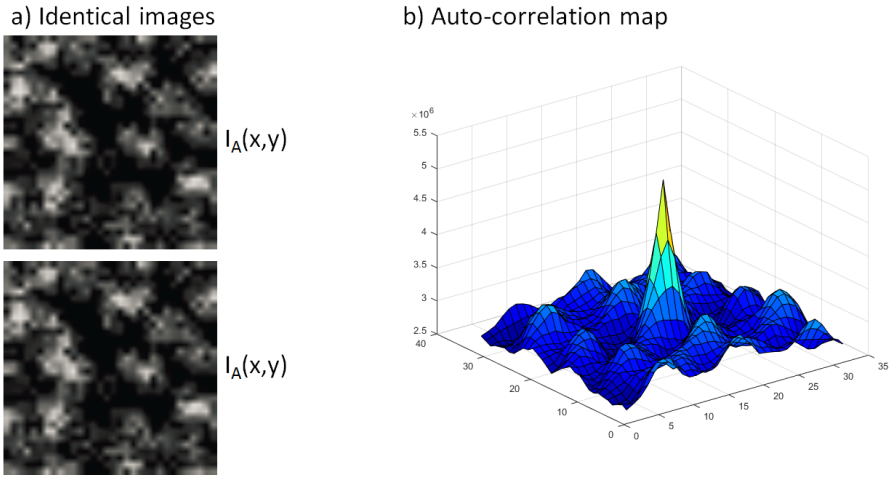

Figure 5.2.4: Representation of an auto-correlation process when there is no particle motion. a) Two identical interrogation windows, b) The correlation function gains its peak value at the center of the interrogation windows in this case.

However, we encounter a problem when particles have a motion. In figure 5.2.5.a we have two distinct interrogation windows with different intensity distributions, $I_A(x, y)$ and $I_B(x, y)$. When we apply the cross-correlation process, we obtain an unclear peak value of the correlarion function as in the figure 5.2.5.b. This problem is due to the noises we obtain in the cross-correlation map.

If we consider an image pair of a selected interrogation window as in the figure 5.2.6, we will obtain noises in the auto-correlation map due to the fact above mentioned. In order to minimize the noises, we apply a filter to the images before correlating the image pairs. The intensity distributions of the images can be divided into two sub-functions as the mean and fluctuating intensities as the following,

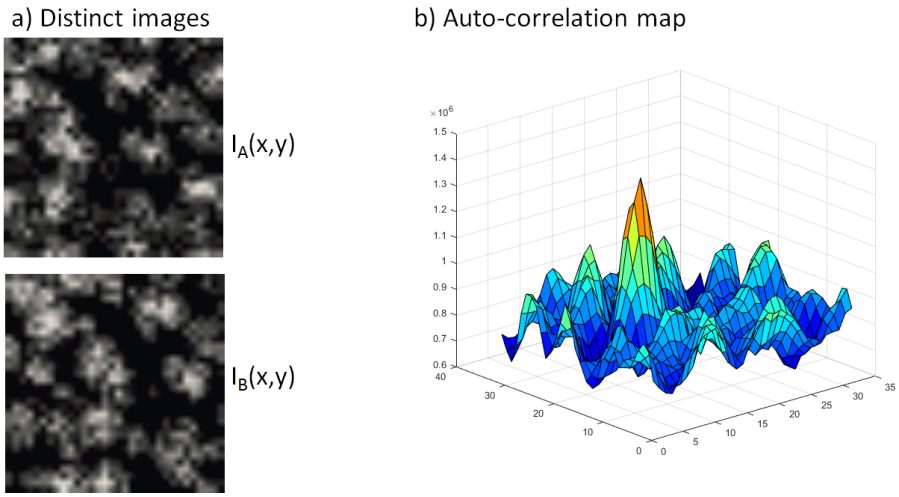

Figure 5.2.5: Representation of an cross-correlation process when particles have any motion. a) Two distinct interrogation windows, b) We see some noise when particles move.

$$\begin{aligned} I_A &=< I_A > + I'_A \ , \\ I_B &=< I_B > + I'_B \end{aligned} \tag{5.2.1}$$

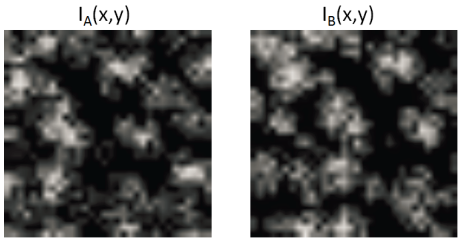

Figure 5.2.6: An image pair of a selected interrogation window of 32×32 pixels. The intensity distributions are $I_A(x, y)$ and $I_B(x, y)$ respectively.

where $< I_A >$ and $< I_B >$ are the mean intensities inside the window, I'_A and I'_B are the fluctuating intensity values. The value of the correlation function for two-dimensional case

$$R(s_x, s_y) = \int I_A(x, y) I_B(x + s_x, y + s_y) dxdy \tag{5.2.2}$$

becomes as the following by substituting the equation (5.2.1) into the equation (5.2.2):

$$\begin{aligned} R(s_x, s_y) = \int [&I'_A(x, y) < I_B(x + dx, y + dy) > + < I_A(x, y) > I'_B(x + dx, y + dy) \\ &+ < I_A(x, y) >< I_B(x + dx, y + dy) > + I'_A(x, y) I'_B(x + dx, y + dy)] \ dxdy \ . \end{aligned} \tag{5.2.3}$$

If we eliminate the mean intensity distributions from the equation (5.2.3), we will be left with the fluctuating intensity distributions

$$I'(x, y) = I'_A(x, y) I'_B(x + dx, y + dy) \ . \tag{5.2.4}$$

The image pairs in the figure 5.2.6 will look like in the figure 5.2.8 by filtering the mean intensity.

The value of the correlation function for the image pair in figure 5.2.8 can be defined as,

$$R(s_x, s_y) = \int I'_A(x, y) I'_B(x + s_x, y + s_y) dxdy \tag{5.2.5}$$

and the cross-correlation map of the image pair will have a clear peak as in the figure 5.2.7.

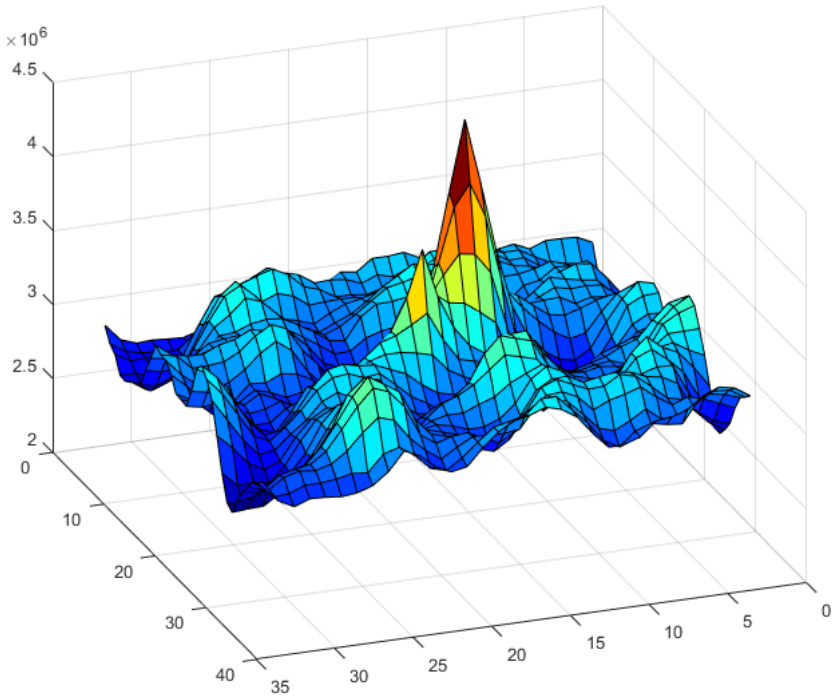

Figure 5.2.7: Cross-correlation map of the image pair in figure 5.2.8. Compared to the figure 5.2.5, we have a clear peak value of the correlation function after filtering the mean intensity.

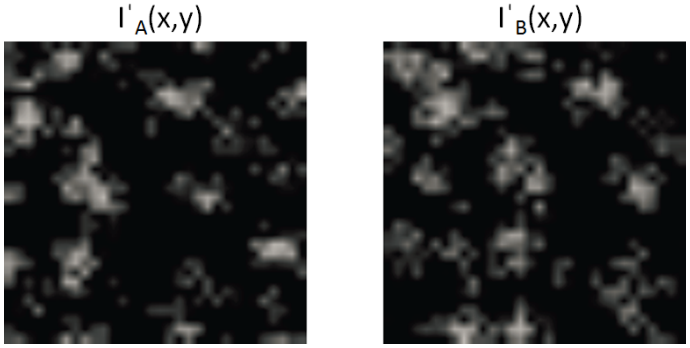

Figure 5.2.8: The same image pair of figure 5.2.6, after removing the mean intensity. The image pair will be left with only fluctuating intensity distributions, I'_A and I'_B.

5.2.3 Processing

This main section contains the cross-correlation algorithm, peak detection and subpixel accuracy. One image pair is correlated and as a result, the peak value of the correlation function is found. Then some interpolation methods are applied in order to find the position of the peak with subpixel accuracy.

Ensemble fast Fourier transform cross-correlation

A direct calculation of the auto-correlation function by the estimation of the equation (5.1.1) is extraordinary costly. Therefore, it is calculated by a 2-dimensional fast Fourier transform (FFT) of the intensity distribution (Prasad, 2000a),

$$\begin{aligned} R(s_x) &= I(x) \star I(x) \ , \\ &= I(x) * I(-x) \end{aligned} \tag{5.2.6}$$

where, $\star$ is the correlation operation, $*$ is the convolution operation [1]. Utilizing the convolution theorem we get,

$$\begin{aligned} F\{R(s_x)\} &= F\{I(x)\} \cdot F^*\{I(x)\} \ , \\ &= |F\{I(x)\}|^2, \end{aligned} \tag{5.2.7}$$

where F represents the Fourier transform and F^* is the conjugate of F. Consequently we get,

$$R(s_x) = F^{-1}\{F\{|I(x)\}|^2\} \ . \tag{5.2.8}$$

In case of the cross-correlation function, if we apply the same theory to the equation (5.1.2) we obtain,

$$R(s_x) = F^{-1}\{F\{I_1(x)\} \cdot F^*\{I_2(x)\}\} \ . \tag{5.2.9}$$

Peak detection

In figure 5.2.9 we see the intensity distribution of two distinct images of particles. Initial and final particle images are distinguished into distinct frames in accordance with the double-frame / single-pulse technique. The arrow demonstrates the displacement vector. The cross-correlation of the both intensity distributions is as in the figure 5.2.9.c. Clearly just one peak value of the correlation function is generated. Owing to the temporal sequence of the images, no directional uncertainty exists (Prasad, 2000a).

Subpixel accuracy

Since the image fields are separated by pixels, the cross-correlation field consists of integer pixel values. Therefore the peak value of the correlation function will be measured to an integer value with an ambiguity of $\pm 1/2$ pixels. This value might seem negligible but considering an interrogation window size of 32×32 pixels and maximum particle shifts of $1/3$ of the interrogation window size, the ambiguity of a maximum particle shift of 10 pixels will be about %5. As the vorticity and strain rates are evaluated from the velocity fields, the ambiguities of them might reach to a value of %10. This amount of ambiguity is not admissible (Dabiri, 2006). Therefore, some kind of interpolation methods are applied in order to achieve a subpixel accuracy. Figure 5.2.10 depicts the problem mentioned above. The peak value of the correlation function is found on an integer pixel value.

[1] Fourier transform of a convolution is defined as the point-wise multiplication of Fourier transforms. If $F\{f\}$, $F\{g\}$ are the Fourier transforms of f and g respectively,
$F\{f * g\} = F\{f\} \cdot F\{g\}$.
It is also true that,
$F\{f \cdot g\} = F\{f\} * F\{g\}$.
If we apply the inverse Fourier transform,
$f * g = F^{-1}\{F\{f\} \cdot F\{g\}\}$ and
$f \cdot g = F^{-1}\{F\{f\} * F\{g\}\}$.

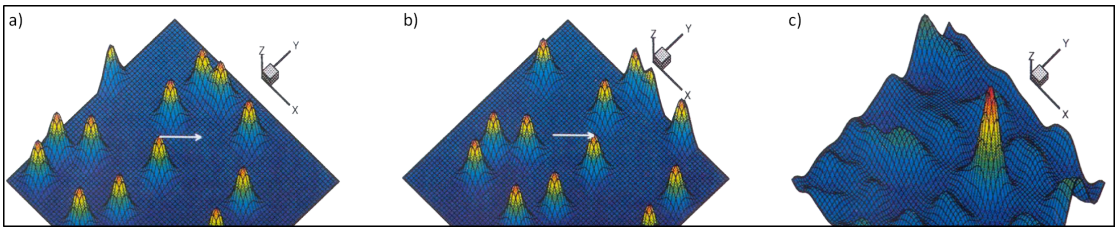

Figure 5.2.9: Peak detection of a cross-correlation process. a) Initial positions of the particles, b) final positions of the particles. The white arrow demonstrates the displacement vector. c) Cross-correlation map of the two images. Peak value of the correlation function is generated (Prasad, 2000a).

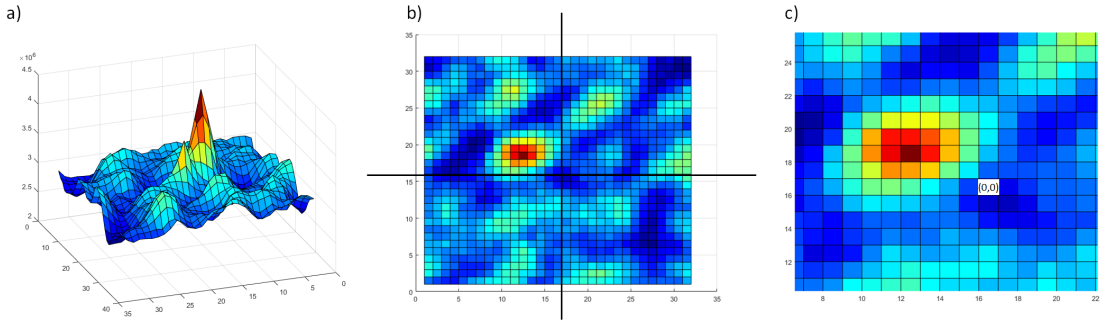

Figure 5.2.10: Depiction of peak value of a correlation function. a) Cross-correlation map in 3D, b) top view of the cross-correlation map. c) A zoom of the cross-correlation map. Peak value of the corelation function is found at $dx = -4$ and $dy = 2$.

The aim of the interpolation methods is to find the location of the peak value of correlation function on a subpixel value. As in the figure 5.2.11, if we fit the intensity values obtained in the cross-correlation map onto a curve, actual peak location may be found on a subpixel location. Without any interpolation peak was detected on $dx = -4, dy = 2$ (figure 5.2.11.a). With the interpolation peak location in the x-direction was found at $dx = -4.1$ (figure 5.2.11.b), and in the y-direction at $dy = 1.9$ (figure 5.2.11.c).

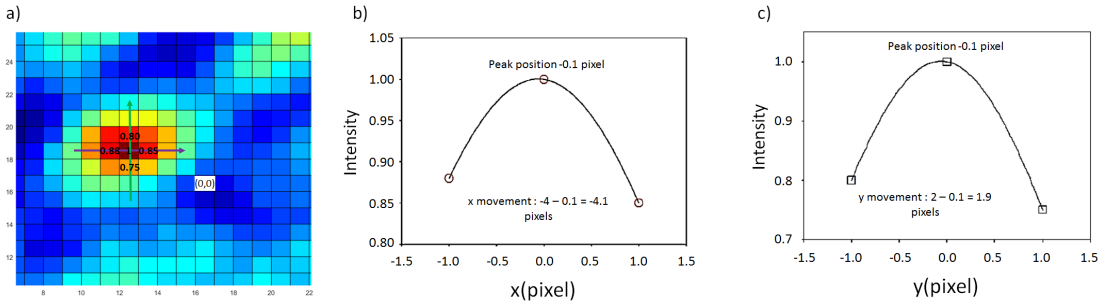

Figure 5.2.11: Depiction of a subpixel accuracy method. a) Cross-correlation map without any interpolation. The numbers on the map are the intensity levels of the pixels. Purple arrow indicates the horizontal direction, green arrow indicates the vertical direction. b) Horizontal profile of the intensity levels. By fitting them onto a curve, one achieves an accurate position of the peak in the horizontal direction. c) Vertical profile of the intensity levels. By fitting them onto a curve, one achieves an accurate position of the peak in the vertical direction.

Interpolation functions used in PIV algorithms are given in table 5.2. Peak centroid method necessitates the correlation field to be thresholded to specify the location of the correlation peak (Alexander and Ng, 1991). But the peak centroid method severely biasses the displacement estimations towards integer pixel values, and causes peak locking on the data obtained (Westerweel et al., 1996; Westerweel, 1997). Nevertheless, there exist other interpolation methods (parabolic

and Gaussian) to detect the location of the peak with subpixel accuracy. When the intensity distributions of the particles approximated by Gaussian interpolation, the correlation also outcomes in a Gaussian intensity distribution. Consequently this method is a better approximation method than the parabolic interpolation. This consequence was demonstrated by calibration experiments (Lourenco and Krothapalli, 1995). In addition, the influence of peak locking is diminished.

Curve fitting function	Three point estimator
Peak centroid	$x_0 = \frac{R_{(i+1,j)} - R_{(i-1,j)}}{R_{(i-1,j)} + R_{(i,j)} + R_{(i+1,j)}}$
$f(x) = \frac{1^{\text{st}} \text{ order moment}}{2^{\text{nd}} \text{ order moment}}$	$y_0 = \frac{R_{(i,j+1)} - R_{(i,j-1)}}{R_{(i,j-1)} + R_{(i,j)} + R_{(i,j+1)}}$
Parabolic	$x_0 = \frac{R_{(i-1,j)} - R_{(i+1,j)}}{2R_{(i-1,j)} - 4R_{(i,j)} + 2R_{(i+1,j)}}$
$f(x) = A(x_0 - x)^2 + B(x_0 - x) + C$	$y_0 = \frac{R_{(i,j-1)} - R_{(i,j+1)}}{2R_{(i,j-1)} - 4R_{(i,j)} + 2R_{(i,j+1)}}$
Gaussian	$x_0 = \frac{\ln R_{(i-1,j)} - \ln R_{(i+1,j)}}{2 \ln R_{(i-1,j)} - 4 \ln R_{(i,j)} + 2 \ln R_{(i+1,j)}}$
$f(x) = A \exp\left[\frac{-(x_0 - x)^2}{B}\right]$	$y_0 = \frac{\ln R_{(i,j-1)} - \ln R_{(i,j+1)}}{2 \ln R_{(i,j-1)} - 4 \ln R_{(i,j)} + 2 \ln R_{(i,j+1)}}$

Table 5.2: Three point estimators used in peak detection with subpixel accuracy. R indicates the value of the correlation function, sub-indices i, j refer to the location of the peak in the correlation map; x_0, y_0 refer to the new coordinates of the peak with subpixel accuracy (Dabiri, 2006).

5.2.4 Output

The last main section of a PIV algorithm includes the visualization of the displacement field and saving the data on a hard drive.

Plot of vector map

In subsection 5.2.2, we have mentioned that each interrogation window at $t = t_0$ was correlated with its equivalent window at $t = t_0 + dt$ as in the figure 5.2.3. The peak value of the correlation function was determined for each interrogation window separately by the FFT algorithm and consequently only one displacement vector for each interrogation window was computed by the computer. Figure 5.2.12 shows the computed displacement vectors on a PIV analysis. The vector field and the time delay dt between the two subsequent images (as in the figure 5.2.2) give an information about the velocity field of the flow.

Save output

During a PIV experiment, many image pairs are obtained by the cameras. Those images are then transfered to the computer in order to analyse them. The temporal resolution of the PIV system will determine the number of the image pairs obtained per time unit. To acquire a statistical data of the flow field, the computed displacement vector field of each image pair must be saved onto the hard drive of the computer.

5.3 Commented code

In the previous section we have given a typical flowchart of a PIV analysis and then we have explained each step in details. In this section by following the same order as in the flowchart

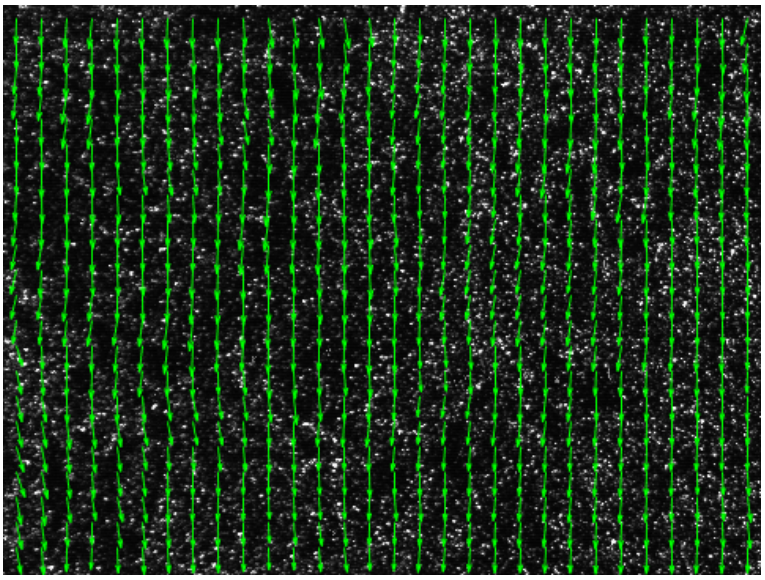

Figure 5.2.12: The displacement vector field obtained by a PIV analysis. Each vector was computed by the cross-correlation of its corresponding interrogation window.

(figure 5.2.1), we will show an example of a PIV algorithm written in Matlab.

5.3.1 Parameters of the algortihm

```
%% Parameters of the algortihm
int_x=32; %interrogation window size in x direction
int_y=32; %interrogation window size in y direction
overlap_x=0.5; %overlap ratio in x direction
overlap_y=0.5; %overlap ratio in y direction
upper_limit=1; %the number of image pair
```

We have chosen an interrogation window size of 32×32 pixels with %50 overlap.

5.3.2 Data information

```
[X,~]=imread(file); %read image
[height,width]=size(X); %height and width of the image
file1=strcat(pathname,filenameroot,num2str(1),fileext); %position of image_1
file2=strcat(pathname,filenameroot,num2str(2),fileext); %position of image_2
[X1,map]=imread(file1); %read image_1
[X2,~]=imread(file2); %read image_2
```

The first line is the command to read the images. The third line gives us the values of height and width of the chosen image. In the lines 4 and 5 we define the image pairs to be analyzed. In the lines 6 and 7 we obtain the intensity distribution of the images in order to correlate them.

5.3.3 Ensemble Fast Fourier Transform cross-correlation

```
%% Procedure : Ensemble FFT-CC
i=1;
j=0;

for m=1:int_x*overlap_x:width %array of int_windows in x-direction
    j=1+j;
    k=0;
    for n=1:int_y*overlap_y:height %array of int_windows in y-direction
        k=k+1;
        if ((m+int_x-1)<=width) && ((n+int_y-1)<=height)
            fftX1=fft2(double(X1(n:n+int_y-1,m:m+int_x-1))); %FFT image_1
            fftX2=conj(fft2(double(X2(n:n+int_y-1,m:m+int_x-1)))); %FFT image_2
            R{i,k,j}=real(ifftshift(ifft2(fftX1.*fftX2))); %cross-corr.
            jj=j;
```

```
15                kk=k;
16            end
17        end
18    end
```

The variables j, k refers to the sequence of the interrogation windows. i is associated to the number of image pairs considered. j indicates the sequence of interrogation windows in the horizontal direction, k indicates the sequence of interrogation windows in the vertical direction. The computations in the lines 4 and 7 give us the number of the interrogation windows in horizontal and vertical directions. The lines 10 and 11 are the Fast Fourier Transforms of the intensity distributions of the image pair. The line 12 is the cross-correlation of the image pair.

5.3.4 Peak detection and interpolation

```
%% Procedure : Peak Detection
count=0;
i=1;
for m=1:jj
    for n=1:kk
        count=count+1;
        [Ix,dx]=max(max(R{i,n,m})); %max. peak in x-direction
        [Iy,dy]=max(max(transpose(R{i,n,m}))); %max. peak in y-direction
        dx=-(dx-int_x/2-1); %distance from orijin in x-direction
        dy=-(dy-int_y/2-1); %distance from orijin in y-direction

        %% Interpolation procedure
        mta=R{i,n,m};
        [iy,ix] = find(ismember(mta, max(max(mta))));

        %% Three point Gaussian peak fit
        dx=dx-0.5*(...
            log(mta(iy,ix-1))-log(mta(iy,ix+1)))/...
            (log(mta(iy,ix-1))-2*log(mta(iy,ix))+log(mta(iy,ix+1)));
        dy=dy-0.5*(...
            log(mta(iy-1,ix))-log(mta(iy+1,ix)))/...
            (log(mta(iy-1,ix))-2*log(mta(iy,ix))+log(mta(iy+1,ix)));
    end
end
```

Here we create a loop in order to find the peak value of the correlation function. The maximum value of the correlation function in x and y coordinates was computed in the lines 7 and 8. Then the interpolation procedure was applied in order to obtain the peak value with a subpixel accuracy. The interpolation was made according to the Gaussian peak fit in this case. The interpolation methods were given in the table 5.2. Later, the coordinates of the peak were found in the x and y directions within the lines 31 and 32. Than the displacements according to the origin, dx and dy were computed in the lines 33 and 34.

```
        %% Parabolic peak fit
        dx=dx-0.5*(...
            (mta(iy,ix-1))-(mta(iy,ix+1)))/...
            ((mta(iy,ix-1))-2*(mta(iy,ix))+(mta(iy,ix+1)));
        dy=dy-0.5*(...
            (mta(iy-1,ix))-(mta(iy+1,ix)))/...
            ((mta(iy-1,ix))-2*(mta(iy,ix))+(mta(iy+1,ix)));
```

In order to apply the parabolic peak fit method, we should replace the code for the Gaussian peak fit with the above-mentioned code. The code for the peak centroid method is given below.

```
         %% Peak centroid
          dx=dx-(-mta(iy,ix-1)+mta(iy,ix+1))/...
                (mta(iy,ix-1)+mta(iy,ix)+mta(iy,ix+1));
          dy=dy-(-mta(iy-1,ix)+mta(iy+1,ix))/...
                (mta(iy-1,ix)+mta(iy,ix)+mta(iy+1,ix));
```

5.4 Application to 2D case

In the previous section we have explained the necessary codes of a PIV algorithm. Now we will make a comparison of the results obtained from direct numerical solution (DNS) of a public

archive. The displacement vector field obtained from the present PIV algorithm is given in figure 5.2.12. In order to estimate the difference in the two flow fields, we plot some data obtained from the codes and DNS. Initially we use no interpolation during the first comparisons. We want to compare the displacement in the x-direction (figure 5.4.1.a). The results indicate that, we have no subpixel accuracy in our algorithm. The detected peak values of the correlation function were only found at integer pixel values. In this case, computed displacement disparity obtained from the codes and DNS in the x-direction was $D_x = 154.79$. Second, we applied the peak centroid in order to achive subpixel accuracy (figure 5.4.1.b). In this case the peak values of the correlation functions was found at the subpixel values but we had deviations from the results obtained by DNS (figure 5.4.1.b). Computed disparity was $D_x = 74.70$. Third, we applied the parabolic interpolation (figure 5.4.1.c). We still had some deviations from the results obtained by DNS. The computed disparity in the x-direction was $D_x = 19.84$. At last, we applied the Gaussian interpolation in our codes (figure 5.4.1.c). As we have discussed in the subsection 5.2.3, Gaussian gave better results compared to the parabolic interpolation. In this case, the computed disparity in the x-direction was $D_x = 0.0005$.

The values of disparities were computed as the following,

$$\begin{aligned} D_x &= \sum_{i=1}^{N} \left| \bar{dx} - dx \right|_i \ , \\ D_y &= \sum_{i=1}^{N} \left| \bar{dy} - dy \right|_i \end{aligned} \tag{5.4.1}$$

where i indicates the sequence of the interrogation windows, $i = 1, 2, 3, ..., N$, in our case $N = 660$, dx and dy indicate the displacements obtained from our code in the x and y directions respectively, $\bar{dx}$ and $\bar{dy}$ indicate the DNS results.

In the table 5.3, error values obtained from different interpolation methods were summarized. The errors were computed by the following expressions,

$$\begin{aligned} \varepsilon_x &= D_x/N \ , \\ \varepsilon_y &= D_y/N \end{aligned} \tag{5.4.2}$$

where, N is the total number of the interrogation windows.

Interpolation method	ε_x [pixel]	ε_y [pixel]
No interpolation	0.23	0.21
Peak centroid	0.11	0.07
Parabolic	0.03	0.04
Gaussian	0.00079	0.00047

Table 5.3: Errors computed from different interpolation methods. The unit of errors are pixels per interrogation window. ε_x and ε_y indicate the errors in x and y directions respectively. Apparently, Gaussian interpolation gives the least amount of error.

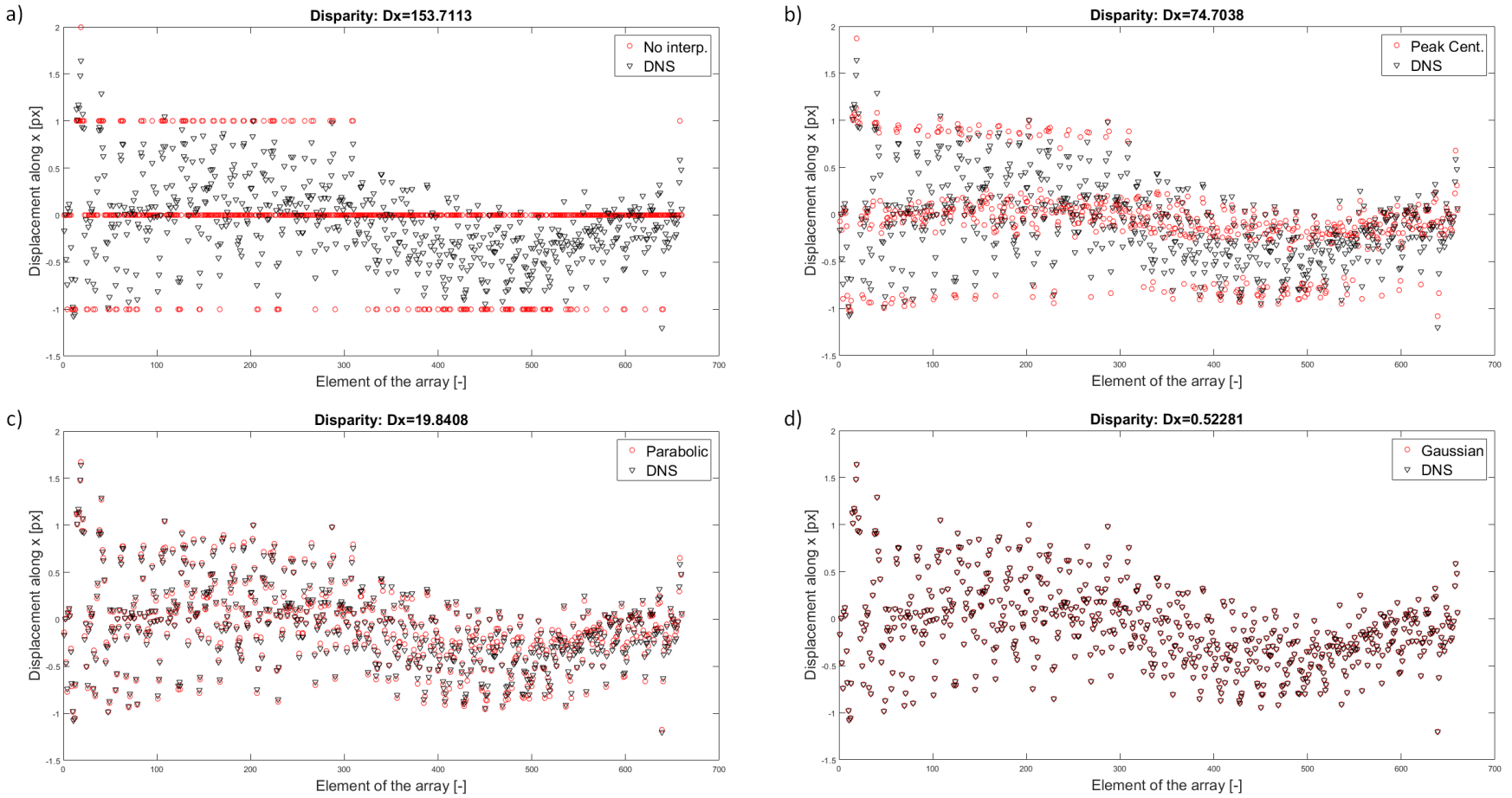

Figure 5.4.1: Displacements in the x-direction. Red circles indicate the results obtained from our code and black triangles indicate the DNS result. a) No interpolation, disparity = 154.79 pixels. b) Peak centroid, disparity = 74.70 pixels. c) Parabolic interpolation, disparity = 19.84 pixels. d) Gaussian interpolation, disparity = 0.0005 pixels.

5.5 PIV algorithms for 3D velocimetry

In the previous sections, PIV analyzing algorithms for 2-dimensional case were considered. Here a brief discussion about PIV algorithms in the instance 3-dimensional domain will be given. Three dimensional analysis of velocimetry methods are possible with PIV and PTV (refer section 1.2 for general properties of PTV) techniques. Output data of PIV and PTV methods are velocity field of fluid and particle trajectories respectively. Figure 5.5.1 represents a flowchart of 3-dimensional velocimetry analyses. 3D PIV/PTV analyzing algorithms first reconstruct the images obtained from cameras in a 3-dimensional virtual environment. Then the velocity fields are obtained by motion analysis.

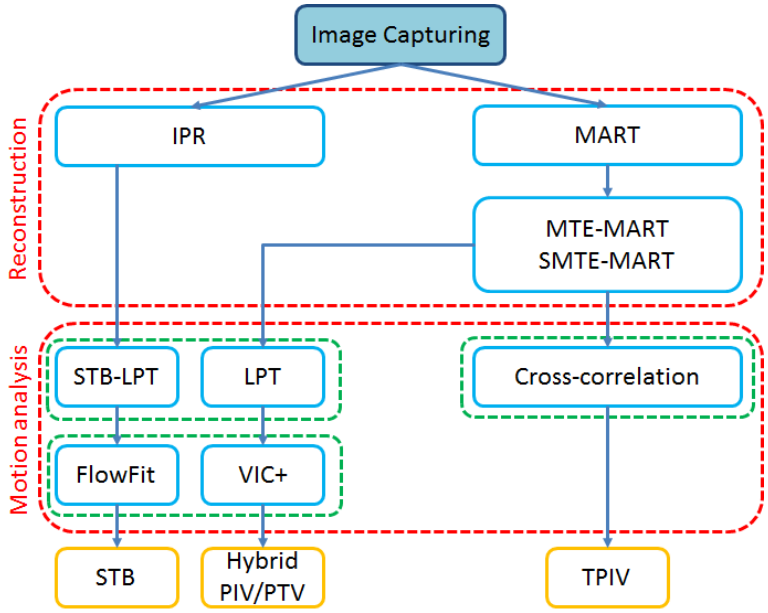

Figure 5.5.1: Flowchart of reconstruction and motion algorithms for 3D velocimetry. IPR and MART reconstruction methods are used in PTV and PIV algorithms respectively.

5.5.1 Reconstruction

A 3D-PIV technique uses different simultaneous perspectives of the illuminated particles and reconstructs them 3-dimensionally by tracking light intensity distributions of the images by means of optical tomography. The method is consequently named tomographic particle image velocimetry (tomographic-PIV). The reconstruction is exerted with the MART (Multiplicative Algebraic Reconstruction Technique) algorithm, providing a 3-dimensional array of light intensity discretized over voxels (Elsinga et al., 2006). The main systematic error of TPIV systems is reported to be the appearance of ghost particles in the reconstruction section of the algorithm.

The generation of ghost particles, which can be considered as reconstruction noise, is shown in figure 5.5.2 for a setup with 2 cameras. Two particles are contained in the detection volume, which are seen by the first camera throughout the lines of sight LOS1 and LOS2 and by the second camera throughout the lines LOS3 and LOS4 resulting in the recorded images I_{cam1} and I_{cam2}. In a real measurement, those images are utilized for the reconstruction of the particle distribution in the detection volume. Reconstructions of particles can be appeared at the intersection points of a lines of sight of both cameras. The intersection points, in this case, result in three possible solutions during the particle reconstruction process (figure 5.5.2.b). Beginning from an initially uniform intensity distribution, MART reconstruction algorithm generates an intensity field identical to the 4-particle solution (figure 5.5.2.b right), where the particles have equal intensity. But only two of them are the real particles (Elsinga et al., 2011).

The motion-tracking-enhanced MART (MTE-MART) is an extension of MART, which increases the accuracy of TPIV by reducing the number of ghost particles by means of the combined utilization of a short sequence of non-simultaneous recordings. The main disadvantage of the

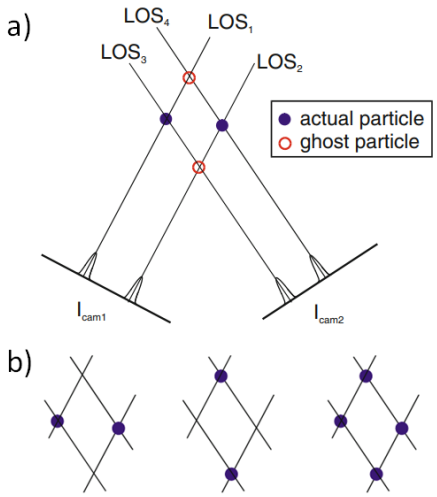

Figure 5.5.2: A representation of the ghost particle issue. a) Formation of ghost particles in a 2-camera setup. b) Possible reconstruction solutions to the 2-particle-2-camera problem (Elsinga et al., 2011).

MTE-MART technique is its computational cost. For huge number of images containing time-resolved sequences, MTE-MART is very costly and is hardly employed even for flows with dense seeding. A recent application is suggested for TPIV technique, that extremely diminishes the computational efforts of MTE-MART, probably beneath of usual MART. The method is a sequential algorithm that generates a time marching evaluation of the intensity field depending on an improved estimation, which is established upon the object reconstructed at the preceding time instant. This method turns out to be effective after a number of snapshots (mainly 5–10). The method is called sequential MTE-MART (SMTE) and it is suitable for time-resolved applications. The computational effort degradation due to SMTE simply rises from the fewer MART iterations necessary for each time instant. Furthermore, this technique provides high reconstruction quality and better velocity field measurement accuracy compared to MART and MTE-MART methods (Lynch and Scarano, 2015).

Apart from MART reconstruction methods, IPR (iterative particle reconstruction triangulation) method is used in PTV applications, if especially the analysis of discrete particle positions are desired. This method provides a reliable reconstruction of particles by reducing the computational costs significantly. The method is utilized by the Shake-the-Box (STB) Lagrangian particle tracking technique, which provides precise tracking of particles at the same seeding density levels used in TPIV, by increasing temporal consistency of particle trajectories to acquire a precise estimation of particle positions. STB can also be named 4D-PTV. STB has the advantages of fast computing time and suppressed number of ghost particles (Schneiders, 2017).

5.5.2 Motion analysis

After the reconstruction of a TPIV algorithm, tomogram pairs are then analyzed by 3D cross-correlation technique with an iterative multigrid volume deformation technique, providing the three-component velocity vector distribution over the measurement volume (Elsinga et al., 2006).

In case of STB, dense velocity information at chaotically propagated 3-dimensional positions of particles in a turbulent flow allows the utilization of a velocity and acceleration interpolation scheme onto an Eulerian grid. The interpolation algorithm is named FlowFit. The estimation of time resolved image data of Shake-the-Box and FlowFit yields the 3-components of Lagrangian velocity and acceleration data of the flow field together with the all components of the gradient tensor (Schneiders, 2017).

Another velocimetric approach is the hybrid PIV/PTV method, which combines the benefits of the two techniques: the robustness of PIV and the spatial resolution of PTV. The technique is a hybrid algorithm that begins by statistical estimation of the displacement of a tracer (PIV) and additionally refines the resolution of measurement with the tracking of individual particles (PTV) (Stitou and Riethmuller, 2001). The velocity field is obtained by means of VIC+ tech-

nique in this case. It utilizes a set of data for intense velocity interpolation comprised of the instantaneous velocity and material derivative measurements acquired from Lagrangian particle tracking velocimetry (Schneiders, 2017).

6. Protocol

In this section, the rules for lab safety, experimental setup, calibration and optimization of the set-up will be discussed in order to run the experiment properly.

6.1 Lab safety

Only the class 4 type lasers are used in PIV applications. Reflected or diffusely reflected laser beams of class 4 lasers may hazard eye. Eye, skin and fire hazard are foreseen in direct beam. Therefore the lab safety rules are very crucial.

1. Check up laser safety requisite before the laser operation and guarantee that the safety instructions were accomplished.
2. Make sure that the laser safety instruments were provided. Each co-worker must use laser safety googles to hinder the laser radiance to make an eye contact.
3. Others must be informed when the laser is operating. Therefore an indication of a warning sign out of the lab is mandatory.
4. The doors of the lab must be locked from inside before the laser operation begins.
5. Hang safety curtains to to block out all the laser light reaching from the test section to the lab environment.
6. Co-workers must remove their watches and jewelry before the operation.
7. The instruments must be so installed that the path of the laser beam must be out of the way. It is safer to make adjustments in this way.
8. Laser operation must be performed by considering the instructions in the laser manual.
9. Keep your eye level out of the plane of the laser beam!

6.2 Experimental setup

Appropriate instruments to run a PIV experiment must be set-up properly. Therefore the following rules must be applied for the determination and arrangement of the instruments.

1. Locate the laser and install the light sheet optics.
    1.1. The height of the light sheet must be greater than the region of interest.
2. Determine the lens.
    2.1. Compute the magnification of the lens by using the equation (4.3.2).
    2.2. Compute the operation distance of the lens by equation (3.4.1).
    2.3. Consider the optimization procedures indicated by Prasad (2000a) and compute the required f-number and depth of field by using the equations (3.4.2) and (3.4.6) respectively.
3. Arrange the cameras.

3.1. The cameras must have at least 1 megapixel resolution at 3 kHz.

3.2. Mount the lenses to the cameras and locate them on the computed operation distance.

3.3. The cameras must be connected to the computer and to the trigger. A PIV software program (e.g. LaVision DaVis) must be installed in the computer.

6.3 Calibration

Calibration maintains a mapping between the object plane and image plane. In order to operate the cameras and run the experiment properly, calibration rules must be satisfied.

1. Use a calibration target (e.g. a checkerboard grid), which covers the whole region of interest.
2. Locate the calibration target into the region of interest.
3. Specify a reference coordinate system in the region of interest. Reference coordinate system should overlap with the coordinate system determined for the test section.
4. Overlap the origin of the calibration target with the origin of the region of interest by regulating the height of the platform.
5. Fill the test section with water.
6. Illuminate the region of interest with the laser during the calibration process.
7. Adjust the cameras to the continuous shot mode in the PIV software program.
8. Make it sure that each camera is covering the region of interest by adjusting the width and height of the camera view.
9. Adjust the positions of the cameras until getting sharp images of the calibration target.
10. Turn off the continuous shot mode and turn off the laser.

6.4 Optimization of the set-up

Before running the experiment, some additional adjustments maybe requiered. Trigger system, particle focusing, light scattering properties of the particles, particle concentrations must be optimized.

1. Define the frame rate in the PIV software program.
2. Check if the trigger is sending the right frequency signal to the laser.
3. Adjust the cameras to the continuous shot mode, turn on the laser and seed the flow.
4. Make sure that particles in the flow are in focus by adjusting the focusing rod of the lenses if necessary.
5. Check that the cameras are not saturated by the intensity of the light scattered from the particles. Regulate the laser current if necessary. Ragulating the laser current can alter the location of the focal point. Repeat the calibration steps if necessary.
6. Check that the particles are not travelling more than 8 pixels in the consecutive images (Lu and Sick, 2013). If the particles are travelling more than 8 pixels, decrease the frequency of the laser.
7. The concentration of the seeding particles should not exceed 8-10 particles per an interrogation window size of 32×32 pixels (Lu and Sick, 2013).

7. Conclusion

Behaviours of particles in a turbulent flow is a complex phenomenon. In order to investigate their motion and dynamics and obtain statistical information, an experimental design with a turbulent channel flow is considered. PIV technique as a non-intrusive measurement method was chosen owing to its high spatial and temporal resolution properties. In this work, the experimental setup required to investigate the above mentioned configuration was designed.

The test section will be located at the end of the channel, where the turbulence is already developed. The wall thickness of the optically transparent test-section is considered to be approximately 10 mm. One fact by optimizing the wall thickness of the test section is, that alteration in thickness makes sense only within the range of nanometers. Increasing the wall thickness of the test section within the range of milimeters will not alter the transmission of light seriously but it will increase the rate of refrection, which is not desirable. Furthermore, plexiglas is considered to be the material of the transparent test section owing to its strength and mounting properties. The diameter of the tracer particles should be small enough in order to follow the streamlines of the flow faithfully. Therefore, tracers with 20 μm is adequate for the experimental conditions. A high-power, high-speed Nd: YAG laser with 1 kHz frequency and four CMOS cameras (1 MP resolution, 3 kHz frequency) are desirable in case of TPIV. Throughout the pulse duration of the laser, a particle should not travel more than one diameter. Therefore the pulse duration should be less than $0.299\mu s$. The region of interest isapproximately $(6 \times 6 \times 1.5cm^3)$. Therefore, lenses with $f = 50$ mm and $f^{\#} = 11$ is sufficient in order to obtain the desired depth of field. In case of SPIV, two CMOS cameras (1 MP resolution, 3 kHz frequency) and two lenses with $f = 50$ mm and $f^{\#} = 2.8$ are sufficient to focus on the particles. Water filled prisms are required for minimizing the refraction rate. Instead of the Scheimplug condition, cameras should be rotated to keep the region of interes in focus, in order to reduce the alterations in magnification. For different sized particles, lens optimization procedures must be reconsidered. The particle image diameter has a lower limit, which is determined by the particle size, the pixel size of the camera sensor, the f-number of the imaging system, and optical aberrations. In order to obtain results with the best possible spatial resolution and dynamic spatial range by means of correlation methods, following considerations must be satisfied:

1. use the smallest possible working distance (by taking perspective errors into account),
2. select a high-quality objective lens with low f-number,
3. use a camera with small pixel size and large sensor,
4. acquire a sufficient amount of PIV recordings for single-pixel or sum-of-correlation evaluation.

Phase discrimination between different phases shall be done by the digital mask technique. A "single frame / multi exposure" PIV technique is considerable in order not to obtain any ambiguity in the direction of the displacement vectors.

Different possible configurations have been considered with respect to the PIV setup. SPIV, DSPIV, TPIV methods are suitable for our case. In case of low velocity gradients, the results obtained from SPIV technique will be accurate. In case of high velocity gradients, DSPIV or TPIV shall be used. Depending on the measurement accuracy, DSPIV is one step ahead but high costs, experimental efforts and the size of the detection volume make TPIV considerable. DSPIV and TIP are both sophisticated PIV techniques. Therefore, an experimental progress with the following sequential order is suggested:

1. Begin with a planar-PIV and get comfortable with PIV analyses,

2. change setup to SPIV and obtain statistical data with 3-velocity components,

3. change setup to TPIV and obtain information from an illuminated volume.

An algorithm to find the flow field starting from a pair of images has been developed. Four main steps are followed in a PIV analysis. Those are: input data, settings and preprocessing, processing, output. In the input section, one must select at least one pair of images in order to begin the algorithm. In the settings and preprocessing, interrogation window size and overlap ratio is determined and filtering is applied for removing the mean intensity values. In the processing section, cross-correlation of the fluctuating intensity values is performed and peak value of the correlation function is computed. Mainly the Gaussian interpolation method is applied in order to obtain subpixel accuracy. In the output section, displacement vector field is monitored. In case of 3D velocimetry analyses, the algorithms are more complex. MART method is applied for the particle reconstruction for TPIV technique. The efficiency of the MART algorithm is increased by SMET-MART. 3-dimensional cross-correlation is performed for the motion analysis. PTV techniques utilize IPR method for the particle reconstruction. STB is a 3-dimensional PTV technique, which tracks the Lagrangian trajectories of particles and extracts the 3-components of velocity and acceleration fields with the complete tensor gradients. Hybrid PIV/PTV technique combines the benefits of the robustness of PIV and the spatial resolution of PTV. The velocity field, in this case, is obtained by means of VIC+ technique.

Finally, general guidelines have been provided to fulfill safety. When performing the experiments, some rules must be followed mainly for safety and calibration issues. In PIV experiments class 4 type lasers are used. Reflected or diffusely reflected laser beams of class 4 lasers may hazard eye. Eye, skin and fire hazard are foreseen in direct beam. The calibration and optimization rules must also be satisfied in order to operate the cameras and run the experiment properly.

A. Hydrodynamic entry length

The governing equation for the hydrodynamic entry length to obtain fully-developed turbulence is given by Tongpun et al. (2014) as,

$$\frac{L_h}{D} \approx 4.4(Re)^{1/6} \tag{A.0.1}$$

For noncircular conduits, the hydraulic diameter can be used instead of the conduit diameter and can be calculated by equation as expressed in table A.1.

Geometry	Hydraulic diameter
Circular tube	$D_H = \frac{4 \cdot \frac{\pi D^2}{4}}{\pi D} = D$
Annulus	$D_H = \frac{4 \cdot \frac{\pi\left(D_{out}^2 - D_{in}^2\right)}{4}}{\pi(D_{out}+D_{in})} = D_{out} - D_{in}$
Square duct	$D_H = \frac{4a^2}{4a} = a$
Rectangular duct (fully filled)	$D_H = \frac{4ab}{2(a+b)} = \frac{2ab}{a+b}$
Channel of water or partially filled rectangular duct	$D_H = \frac{4ab}{2a+b}$

Table A.1: Conduit geometries and their hydraulic diameters.

B. Solutions of the newtonian viscous-flow equations

Solutions of the newtonian viscous flow equations were widely discussed in White (1974). Just important points for our case were here denoted.

Continuity and momentum equations for incompressible newtonian flow with neglected gravity and constant transport characteristics shall be inscribed as:

$$div\ \mathbf{V} = 0\ , \tag{B.0.1}$$

$$\rho\frac{D\mathbf{V}}{Dt} = -\boldsymbol{\nabla}\hat{p} + \mu\boldsymbol{\nabla}^2\mathbf{V}\ . \tag{B.0.2}$$

Here, Φ is the dissipation function and $\hat{p}$ denotes the total hydrostatic pressure.

B.1 Poiseuille flow through ducts

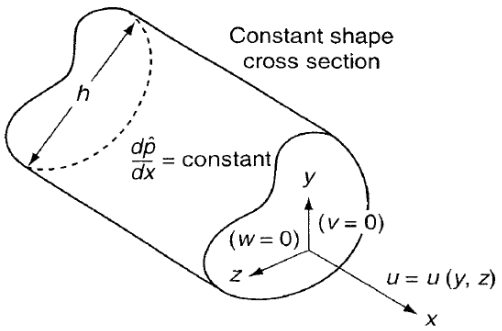

Figure B.1.1: An illustration of a fully developed duct flow in cartesian coordinate (White, 1974).

Due to fully developed duct flow, continuity and momentum equations for an incompressible flow degrade to

$$\frac{\partial\mu}{\partial x} = 0 \tag{B.1.1}$$

$$\begin{aligned} 0 &= -\frac{\partial\hat{p}}{\partial x} + \mu\left(\frac{\partial^2 u}{\partial y^2} + \frac{\partial^2 u}{\partial z^2}\right) \\ 0 &= -\frac{\partial\hat{p}}{\partial y} = -\frac{\partial\hat{p}}{\partial z}\ . \end{aligned} \tag{B.1.2}$$

Those equations point out the total pressure $\hat{p}$ is only dependent on x for the fully developed flow. Moreover, since u doesn't alter with x, it tracks from the equation of x-momentum, so the gradient $d\hat{p}/dx$ has to be a negative constant number. The fundamental equation of a fully developed duct flow is given as

$$\frac{\partial^2 u}{\partial y^2} + \frac{\partial^2 u}{\partial z^2} = \frac{1}{\mu}\frac{d\hat{p}}{dx} = const \tag{B.1.3}$$

issue only to the no slip condition $u_w = 0$ everywhere on the duct surface. The appropriate scaling of the equation (B.1.3) might contain μ, $d\hat{p}/dx$ and some typical duct with h. Therefore the dimensionless factors are

$$\begin{aligned} y^* &= \frac{y}{h} \\ z^* &= \frac{z}{h} \\ u^* &= \frac{\mu u}{h^2(-d\hat{p}/dx)} \end{aligned} \tag{B.1.4}$$

the negative pressure gradient is necessary to make u^* a positive number. In terms of those factors, equation (B.1.3) will become

$$\boldsymbol{\nabla}^{*2}(u^*) = -1 \tag{B.1.5}$$

issue to $u^* = 0$ at each point on the boundary of the cross section of the duct.

B.2 The circular pipe: Hagen-Poiseuille flow

Circular pipe is probably our most well-known viscous flow, primarily examined by Hagen and Poiseuille. The single variant is $r^* = r/r_0$, where r_0 is the radius of the pipe. The Laplacian operator degrades to

$$\boldsymbol{\nabla}^2 = \frac{1}{r}\frac{d}{dr}\left(r\frac{d}{dr}\right) \tag{B.2.1}$$

the solution of equation (B.1.5) is

$$u^* = -\frac{1}{4}{r^*}^2 + C_1 \ln r^* + C_2 \ . \tag{B.2.2}$$

On physical grounds the velocity can not be infinite on the center line, we deny the logarithmic term and regulate $C_1 = 0$. The no slip condition is provided by regulating $C_2 = +1/4$. Therefore the pipe flow solution is

$$u = \frac{-d\hat{p}/dx}{4\mu}(r_0^2 - r^2) \ . \tag{B.2.3}$$

Total volume flow rate Q is of concern, as specified for a duct by

$$Q = \int_A u \ dA \ . \tag{B.2.4}$$

Here, the component of area is $2\pi r \ dr$ for the case of pipe. The integration grants

$$Q_{pipe} = \frac{\pi r_0^4}{8\mu}\left(-\frac{d\hat{p}}{dx}\right) \ . \tag{B.2.5}$$

The mean velocity is specified by $\bar{u} = Q/A$ and grants

$$\bar{u} = \frac{r_0^2(-d\hat{p}/dx)}{8\mu} = \frac{1}{2}u_{max} \ . \tag{B.2.6}$$

At last, the wall shear stress is fix and is defined by

$$\tau_w = \mu\left(-\frac{du}{dr}\right)_w = \frac{1}{2}r_0\left(-\frac{d\hat{p}}{dx}\right) = \frac{4\mu\bar{u}}{r_0} \ . \tag{B.2.7}$$

Even τ_w is proportional to the mean velocity of the laminar flow, it is conventional, expecting turbulent flow, to make wall shear dimensionless with the *dynamic pressure* of the pipe, $\rho\bar{u}^2/2$, in comparison with

$$C_f = \frac{\tau}{\frac{1}{2}\rho U^2} = \frac{\mu}{\rho U h} = \frac{1}{Re_h} \ . \tag{B.2.8}$$

Therefore the Reynolds number $Re_h = \rho U h/\mu$ emerges spontaneously if the shear stress is dimensionless.

Two diverse friction factor depictions are generally used in the literature:

$$\begin{aligned} \lambda &= \frac{8\tau_w}{\rho \bar{u}^2} \ , \\ C_f &= \frac{2\tau_w}{\rho \bar{u}^2} = \frac{1}{4}\lambda \ . \end{aligned} \tag{B.2.9}$$

They are respectively named "*Darcy friction factor*" and "*Fanning friction factor*", or "*skin friction coefficient*". One obtains the usual equationss by substituting into equations (B.2.9),

$$\begin{aligned} \lambda &= \frac{64}{Re_D} \ , \\ C_f &= \frac{16}{Re_D} \ . \end{aligned} \tag{B.2.10}$$

C. The scales of turbulent motion

The scales of turbulent motion were vastly discussed in Pope (2001). Here we make a review of the subject and summarize them by giving the order of magnitude relationships of the scales of turbulent motions at the end of the chapter.

Turbulent behaviors inside a flow emerge over a broad range of time and length scales. For instance, think of the development of a cumulus cloud. The large scale of the cloud shall be in the order of kilometers and can expand or proceed over long time periods. Inside the cloud, mixture of dry exterior air and humid air inside the cloud can emerge over scales in the order of millimeters. For the case of down to earth applications think of a boiler. Large eddies carry oxidizer and fuel along the combustion chamber, whilst mixing the chemical reaction at last happen at the small scales with short time scales confront to the motions in large scales. This assortment in time and length scales is a significant feature of turbulent flows, and a feature which is partly liable for the trouble met in the theoretical and numerical analysis for turbulent flows. We take a time to debate some of the properties consequential with the time and length scales of turbulence.

We have previously seen that scaling laws are a major tool to define turbulence. Most of what we inform and deduce about turbulence is dependent on the order of magnitude predict that trace from sensible applications of dimensional analysis and scaling laws. Specifying the convenient scalings utilizing scale analysis throughout with a comprehension of how varied times and lenghts scale has very practical applications.

C.1 Turbulent length scales

Initially we think of the range of eddy sizes (length scales) that we shall expect to come upon in turbulent flows. The size of the largest eddies in the flow is L, the smallest eddies are η. As already debated, the largest eddies in the flow counted for the most of the momentum and energy transport. The size of those eddies is just limited by the boundaries of the flow. We will mention L as the *integral* length scale. The size of the smallest scales of the flow will be settled by viscosity. We have previously debated the opinion that as we come close to even smaller length scales, the influences of viscosity become more significant. The smallest length scales present in a turbulent flow are the ones where kinetic energy is dissipated into heat. In case of flows with very high Reynolds numbers, the viscous forces are so minor in accordance with the inertial forces. Smaller scale motions are essentially created till the influences of viscosity become major and energy is dissipated.

In case of a statistically steady turbulent flow, the energy dissipated at the small scales must equal the energy provided by the large scales. From the debates directing to Kolmogorov's first similarity hypothesis, the only factors affecting the attitude of the small scale motions are the whole kinetic energy generation rate and the viscosity. The dissipation rate is not dependent of viscosity, *but the scales at which this energy is dissipated depends on both the dissipation rate and viscosity.*

To reach at an evaluation for the scales at which the energy is dissipated one must establish a length scale bonded with the viscosity and dissipation rate. The dimension of dissipation rate per unit mass (ϵ) is (m^2/s^3) and the dimension of viscosity, ν is (m^2/s). The length scale composed from those terms is:

$$\eta = \left(\frac{\nu^3}{\epsilon}\right)^{1/4} . \tag{C.1.1}$$

This length scale named as *Kolmogorov* length scale and it is the smallest hydrodynamic scale in turbulent flows.

To tie up this length scale with the largest length scales, we need an evaluation of the dissipation rate with an expression of the large scale flow properties. The rate of dissipation is equal to the rate of kinetic energy generation. Therefore one needs to acquire an approach to the rate where kinetic energy is provided to the small scales. The kinetic energy inside a flow is proportionally related to U^2. The large eddy turnover time can be predicted as L/U. It is sensible to suppose that the rate of kinetic energy supply is bonded with the inverse of the time scale. The dissipation rate shall be computed by the relation

$$\epsilon \sim \frac{UU}{L/U} \sim \frac{U^3}{L} \ . \tag{C.1.2}$$

for ϵ relation (C.1.1) becomes:

$$\eta = \left(\frac{\nu^3 L}{U^3}\right)^{1/4} \ . \tag{C.1.3}$$

One is able to grasp from relations (C.1.2) and (C.1.3) that the dissipation is not dependent on the viscosity. Viscosity is major on determining dissipation at a length scale. That provides an estimation for the ratio of the largest to the smallest length scales inside a flow:

$$\frac{L}{\eta} \sim \left(\frac{UL}{\nu}\right)^{3/4} = Re^{3/4} \ . \tag{C.1.4}$$

Here, *Re* is the Reynolds number dependent on the large scale flow properties. We anticipate that the dissociation of the smallest and largest length scales rises when the Reynolds number rises. This is a broadly used relationship.

Other length scale frequently met in turbulence is the *Taylor* microscale. Taylor microscale doesn't possess the easy comprehension of physical importance as the integral length or Kolmogorov scales but ensures a suitable evaluation for the fluctuating strain rate field. Taylor microscale, λ is given as

$$\left(\frac{\partial u'}{\partial x}\right)^2 = \frac{u'^2}{\lambda^2} \ . \tag{C.1.5}$$

u' is the rms of the fluctuating velocity field.

The Taylor microscale is bonded with the fluctuations of turbulence. Therefore it is occasionally named as *turbulence length scale*. A turbulence Reynolds number can be calculated dependent on the rms velocity fluctuations and the Taylor microscale:

$$Re_\lambda = \frac{u'\lambda}{\nu} \ . \tag{C.1.6}$$

Taylor microscale, λ, has a historical importance. It is the length scale derived initially to define turbulence.

C.2 Time scales

We define the "large eddy turnover" time as

$$\tau_L = \frac{L}{U} \ . \tag{C.2.1}$$

With the data we have previously introduced, we shall compose a time scale for small eddies by using the dissipation and the viscosity:

$$\tau_\eta = \left(\frac{\nu}{\epsilon}\right)^{1/2} \ . \tag{C.2.2}$$

With our former estimation of the dissipation rate we get

$$\tau_\eta = \frac{\nu L}{U^3} \ . \tag{C.2.3}$$

And he ratio of the timescales is:

$$\frac{\tau_L}{\tau_\eta} = \left(\frac{UL}{\nu}\right)^{1/2} = Re_L^{1/2} \ . \tag{C.2.4}$$

The structures in large scales are noticed to possess even larger time scales than the smallest energy dissipating eddies. The magnitude of the dissociation amongst length and time scales increases, when the Reynolds number also increases.

We should pay attention to the characterization of the large eddy turnover time in details and how it depends on a couple of physical methods. The eddy turnover time of a size l eddy (τ_l) shall be dependent on the time it favors to the size of the eddy to bias the inertial range (t_l). From dimensional analysis we obtain

$$\frac{dl}{dt} \sim -\frac{l}{t_l} \tag{C.2.5}$$

where the typical time scale of a size l eddy shall be bonded with the large eddy turnover time, τ_L handling Kolmogorov scales feasible to the inertial range:

$$t_l \sim \left(\frac{l}{L}\right)^{2/3} \tau_L \ . \tag{C.2.6}$$

We substitude t_l into the equation (C.2.5) and integrate between the integral and Kolmogorov scales. ν grants the time it acquires an integral scale eddy to be degraded to the Kolmogorov scale:

$$\frac{t_L}{\tau_L} = 1 - \left(\frac{\eta}{L}\right)^{2/3} = 1 - Re^{-1/2} \tag{C.2.7}$$

where the ultimate equivalence is acquired utilizing the intercourse $L/\eta \sim Re^{3/4}$ in case of an inertial range turbulence. Regarding the equation (C.2.7) the large eddy turnover time is the time scale for traversing the inertial range of an eddy for flows with high Reynolds number. Equation (C.2.7) portrays the Reynolds number dependency of the process, that disappears for flows with high Reynolds number.

Scale	Equation
Kolmogorov microscale (length scale)	$\eta = \left(\frac{\nu^3}{\epsilon}\right)^{1/4}$
Kolmogorov velocity scale	$v_\eta = (\nu\epsilon)^{1/4}$
Kolmogorov time scale	$\tau_\eta = \left(\frac{\nu}{\epsilon}\right)^{1/2}$

Table C.1: Summary table of the Kolmogorov scales. Those values represent respectively the smallest hydrodynamic length, velocity and time scales in turbulent flows.

C.3 Friction Reynolds number

Friction Reynolds number, is defined as

$$Re_\tau = \frac{u_\tau D}{\nu} \ . \tag{C.3.1}$$

It is the Reynolds number bonded to the friction velocity, u_τ, and on a convenient dimension (diameter of pipe D for empirical data, width of the half-channel for numerical data). Friction velocity is given as

$$u_\tau = \sqrt{\frac{\tau_w}{\rho}} \ . \tag{C.3.2}$$

Here, τ_w is the mean shear stress at the wall, and ρ is density of fluid (Dearing et al., 2013).

Friction velocity, also named as *shear velocity*, is a form by which a shear stress can be rewritten in units of velocity. It is beneficial as a method in fluid mechanics to crosscheck actual velocities, like the velocity of a flow in a stream, to a velocity that bounds up with shear between flow layers.

Shear velocity is used to define shear-involved motion in bustling fluids. It is used for describing:

- Dispersion and diffusion and of particles, tracers, and pollutants in fluid flows
- The velocity profile close to the flow boundary (Law of the wall)
- Sediment transport inside a channel

Shear velocity is also useful for considering the dispersion and shear rate in a flow. Shear velocity scales to the rates of bedload sediment transport and dispersion. One common rule is that the shear velocity is amongst 5% to 10% of the mean flow velocity (Schlichting et al., 1955). When calculating the friction velocity inside a channel, we can consider the channel as a pipe with its relevant hydraulic diameter (see table A.1). We define a pipe with its diameter D and length L (see figure C.3.1).

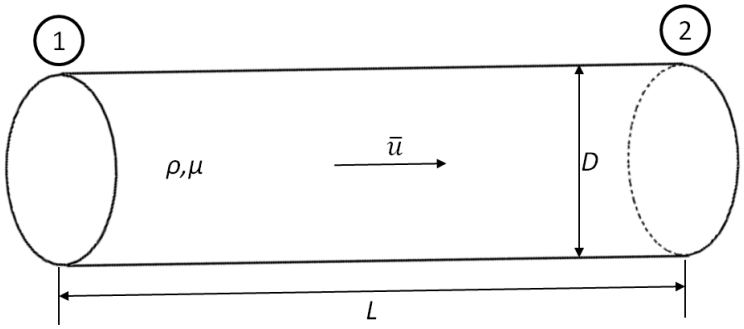

Figure C.3.1: A sketch of a pipe with a diameter D and length L. ρ and μ are respectively the density and the dynamic viscosity of the fluid inside the pipe. $\bar{u}$ is the mean velocity of the flow. The direction of the mean velocity indicates the mean direction of the flow.

By introducing p_1 and p_2 as the pressure values respectively at the inlet and outlet of the pipe, we shall formulate the balance of forces as in the following:

$$p_1 \frac{\pi D^2}{4} = p_2 \frac{\pi D^2}{4} + \tau_w \pi D L \ . \tag{C.3.3}$$

By arranging the terms above, we obtain the pressure difference between the inlet and outlet of the pipe

$$\Delta p = p_1 - p_2 = \frac{4\tau_w}{D} L \ . \tag{C.3.4}$$

The pressure drop Δp inside a pipe and the friction factor f for turbulent flows are given as,

$$\Delta p = \frac{1}{2} \rho \bar{u}^2 f \frac{L}{D} \ , \tag{C.3.5}$$

$$f = 0.079 Re^{-1/4} \ . \tag{C.3.6}$$

From the equality between the equations (C.3.4) and (C.3.5) we get,

$$\tau_w = \frac{\rho \bar{u}^2 f}{8} \ . \tag{C.3.7}$$

By substituting equation (C.3.7) into (C.3.2) we get,

$$u_\tau = 0.099 \ \bar{u} \ Re^{-1/8} \tag{C.3.8}$$

and from the substitution of (C.3.8) into (C.3.1) we obtain the friction Reynolds number:

$$Re_\tau = \frac{0.099\ \bar{u}\ Re^{-1/8}\ D}{\nu}\ . \tag{C.3.9}$$

C.4 Order of magnitude relationships

Taylor microscale is given as the following by a relation with turbulence kinetic energy:

$$\lambda \approx \sqrt{10\nu\frac{k}{\epsilon}} \tag{C.4.1}$$

where $k \sim u^2$ and $\epsilon \sim u^3/l$. Following relations can be easily derived by substituting the given expressions into the equations.

- $\frac{\lambda}{l} \sim Re^{-1/2} \sim Re_\lambda^{-1}$
- $\frac{\eta}{l} \sim Re^{-\frac{3}{4}} \sim Re_\lambda^{-\frac{3}{2}}$
- $\frac{\eta}{\lambda} \sim Re^{-\frac{1}{4}} \sim Re_\lambda^{-\frac{1}{2}}$
- $\frac{v_\eta}{u} \sim Re^{-1/4} \sim Re_\lambda^{-1/2}$
- $\frac{\tau_\eta u}{l} \sim Re^{-1/2} \sim Re_\lambda^{-1}$

Bibliography

Adrian, R. J. (1991). Particle-imaging techniques for experimental fluid mechanics. *Annual review of fluid mechanics*, 23(1):261–304.

Alexander, B. F. and Ng, K. C. (1991). Elimination of systematic error in subpixel accuracy centroid estimation [also letter 34 (11) 3347-3348 (nov1995)]. *Optical Engineering*, 30(9):1320–1332.

Amir (2017). *Diafragma atau Aperture*. `https://amirhomephotography.com/2017/08/06/diafragma-aperture-lensa-dan-ruang-ketajaman/` [Accessed: 25.03.2018].

Arroyo, M. P. and Hinsch, K. D. (2007). Recent developments of PIV towards 3D measurements. In *Particle Image Velocimetry*, pages 127–154. Springer.

Balachandar, S. and Eaton, J. K. (2010). Turbulent dispersed multiphase flow. *Annual Review of Fluid Mechanics*, 42:111–133.

Bastiaans, R. J. (2000). *Cross-correlation PIV; theory, implementation and accuracy*. Eindhoven University of Technology, Faculty of Mechanical Engineering.

Boillot, A. and Prasad, A. (1996). Optimization procedure for pulse separation in cross-correlation PIV. *Experiments in fluids*, 21(2):87–93.

Bordoloi, A. D. and Variano, E. (2017). Rotational kinematics of large cylindrical particles in turbulence. *Journal of Fluid Mechanics*, 815:199–222.

Born, M. and Wolf, E. (1970). Principles of optics.

Cleaver, J. and Yates, B. (1973). Mechanism of detachment of colloidal particles from a flat substrate in a turbulent flow. *Journal of Colloid and Interface Science*, 44(3):464–474.

Cole, B. C., Marcus, G. G., Parsa, S., Kramel, S., Ni, R., and Voth, G. A. (2016). Methods for measuring the orientation and rotation rate of 3D-printed particles in turbulence. *JoVE (Journal of Visualized Experiments)*, 35(112):e53599–e53599.

Dabiri, D. (2006). Cross-correlation Digital Particle Image Velocimetry — A review. *Turbulencia. ABCM, Curitiba*, pages 155–199.

Dawkins, R. (1976). The selfish gene. *Oxford university press*.

Dawkins, R. (2006). The god delusion. *Black Swan*.

Dearing, S. S., Campolo, M., Capone, A., and Soldati, A. (2013). Phase discrimination and object fitting to measure fibers distribution and orientation in turbulent pipe flows. *Experiments in fluids*, 54(1):1419.

Elghobashi, S. (1994). On predicting particle-laden turbulent flows. *Applied scientific research*, 52(4):309–329.

Elsinga, G., Westerweel, J., Scarano, F., and Novara, M. (2011). On the velocity of ghost particles and the bias errors in tomographic-piv. *Experiments in fluids*, 50(4):825–838.

Elsinga, G. E., Scarano, F., Wieneke, B., and van Oudheusden, B. W. (2006). Tomographic particle image velocimetry. *Experiments in fluids*, 41(6):933–947.

Elsinga, G. E., Wieneke, B., Scarano, F., and Schröder, A. (2007). Tomographic 3D-PIV and applications. In *Particle Image Velocimetry*, pages 103–125. Springer.

Erni, P., Cramer, C., Marti, I., Windhab, E. J., and Fischer, P. (2009). Continuous flow structuring of anisotropic biopolymer particles. *Advances in colloid and interface science*, 150(1):16–26.

Ganapathisubramani, B., Longmire, E. K., Marusic, I., and Pothos, S. (2005). Dual-plane PIV technique to determine the complete velocity gradient tensor in a turbulent boundary layer. *Experiments in Fluids*, 39(2):222–231.

Gauthier, C. (2017). *Shutter speed, aperture and ISO*. `http://cgauthier.ca/en/2017/06/12/reciprocity/` [Accessed: 25.03.2018].

Gauthier, V. and Riethmuller, M. (1988). Application of particle image displacement velocimetry (pidv) to complex flows: measurements of the third component. In *In its Particle Image Displacement Velocimetry 44 p (SEE N89-17179 09-34)*.

Geisler, R., Schröder, A., and Kompenhans, J. (2014). Investigation of unsteady flow fields for flow control research by means of Particle Image Velocimetry. *Journal of Flow Control, Measurement & Visualization*, 2(02):42.

Gui, L. and Merzkirch, W. (1996). Phase-separation of PIV measurements in two-phase flow by applying a digital mask technique. *ERCOFTAC Bull*, 30:45–48.

Gürlek, C. (2017). Kare kesitli engellerle donatılmış kanal akışının piv yöntemiyle deneysel olarak incelenmesi. *Fen Bilimleri Dergisi (CFD)*, 38(2).

Hetsroni, G. and Rozenblit, R. (1994). Heat transfer to a liquid—solid mixture in a flume. *International Journal of Multiphase Flow*, 20(4):671–689.

Heymsfield, A. J. (1977). Precipitation development in stratiform ice clouds: A microphysical and dynamical study. *Journal of the Atmospheric Sciences*, 34(2):367–381.

Hinsch, K. D. and Hinrichs, H. (1996). Three-dimensional particle velocimetry. In *Three-Dimensional Velocity and Vorticity Measuring and Image Analysis Techniques*, pages 129–152. Springer.

Hoseini, A. A., Lundell, F., and Andersson, H. I. (2015). Finite-length effects on dynamical behavior of rod-like particles in wall-bounded turbulent flow. *International Journal of Multiphase Flow*, 76:13–21.

Hoseini, A. A., Zavareh, Z., Lundell, F., and Anderson, H. I. (2014). Rod-like particles matching algorithm based on som neural network in dispersed two-phase flow measurements. *Experiments in fluids*, 55(4):1705.

Jahanmiri, M. (2011). Particle image velocimetry: Fundamentals and its applications. Technical report, Chalmers University of Technology.

Junior, J. (2017). *Composition and Motion of Stars*. `https://jjcastronomy.wordpress.com/2017/04/28/composition-and-motion-of-stars/` [Accessed: 25.03.2018].

Kaftori, D., Hetsroni, G., and Banerjee, S. (1994a). Funnel-shaped vortical structures in wall turbulence. *Physics of Fluids*, 6(9):3035–3050.

Kaftori, D., Hetsroni, G., and Banerjee, S. (1994b). Funnel-shaped vortices-large scale dominant structures in bounded turbulent shear flows. *ASME-PUBLICATIONS-FED*, 188:13–13.

Kaftori, D., Hetsroni, G., and Banerjee, S. (1995a). Particle behavior in the turbulent boundary layer. i. motion, deposition, and entrainment. *Physics of Fluids*, 7(5):1095–1106.

Kaftori, D., Hetsroni, G., and Banerjee, S. (1995b). Particle behavior in the turbulent boundary layer. ii. velocity and distribution profiles. *Physics of Fluids*, 7(5):1107–1121.

Kaftori, D., Hetsroni, G., and Banerjee, S. (1998). The effect of particles on wall turbulence. *International Journal of Multiphase Flow*, 24(3):359–386.

Kaku, M. (1995). *Hyperspace: A scientific odyssey through parallel universes, time warps, and the tenth dimension*. OUP Oxford.

Liberzon, A., Gurka, R., and Hetsroni, G. (2004). XPIV - Multi-plane Stereoscopic Particle Image Velocimetry. *Experiments in Fluids*, 36(2):355–362.

Lindken, R. and Merzkirch, W. (2002). A novel piv technique for measurements in multiphase flows and its application to two-phase bubbly flows. *Experiments in fluids*, 33(6):814–825.

Litwiller, D. (2001). Cmos vs. ccd: Facts and fiction. *Photonics Spectra, January*.

Lourenco, L. and Krothapalli, A. (1995). On the accuracy of velocity and vorticity measurements with piv. *Experiments in fluids*, 18(6):421–428.

Lu, L. and Sick, V. (2013). High-speed particle image velocimetry near surfaces. *Journal of visualized experiments: JoVE*, 53(76).

Lundell, F., Söderberg, L. D., and Alfredsson, P. H. (2011). Fluid mechanics of papermaking. *Annual Review of Fluid Mechanics*, 43:195–217.

Lynch, K. and Scarano, F. (2015). An efficient and accurate approach to mte-mart for time-resolved tomographic piv. *Experiments in Fluids*, 56(3):66.

Maas, H., Gruen, A., and Papantoniou, D. (1993). Particle tracking velocimetry in three-dimensional flows. *Experiments in Fluids*, 15(2):133–146.

Maheo, P. M. (1999). *Free-surface turbulent shear flows*. PhD thesis, California Institute of Technology.

Merzkirch, W., Gui, L., Hilgers, S., Lindken, R., and Wagner, T. (1997). PIV in multiphase flow. In *Proc. International Workshop on PIV-Fukui*, volume 97, pages 165–171.

Michaelis, D. and Wieneke, B. (2008). Comparison between tomographic PIV and stereo PIV. In *Proceedings of the 14th International Symposium on Applications of Laser Techniques to Fluid Mechanics. Lisbon, Portugal*. Citeseer.

Moffet, R. C. and Prather, K. A. (2009). In-situ measurements of the mixing state and optical properties of soot with implications for radiative forcing estimates. *Proceedings of the National Academy of Sciences*, 106(29):11872–11877.

Mullin, J. A. and Dahm, W. J. (2005). Dual-plane stereo particle image velocimetry (DSPIV) for measuring velocity gradient fields at intermediate and small scales of turbulent flows. *Experiments in fluids*, 38(2):185–196.

Omidvarborna, H., Kumar, A., and Kim, D.-S. (2015). Recent studies on soot modeling for diesel combustion. *Renewable and Sustainable Energy Reviews*, 48:635–647.

Pajser (2017). *How to make your low light photos better*. `http://http://en.miui.com/thread-631470-1-1.html` [Accessed: 25.03.2018].

Pedinotti, S., Mariotti, G., and Banerjee, S. (1992). Direct numerical simulation of particle behaviour in the wall region of turbulent flows in horizontal channels. *International journal of multiphase flow*, 18(6):927–941.

Pedley, T. and Kessler, J. (1992). Hydrodynamic phenomena in suspensions of swimming microorganisms. *Annual Review of Fluid Mechanics*, 24(1):313–358.

Pope, S. B. (2001). Turbulent flows.

Pothos, S., Troolin, D., Lai, W., and Menon, R. (2009). V3V-volumetric three-component velocimetry for 3d flow measurements main principle, theory and applications. *Revista Termotehnica*, 2:2009.

Prasad, A. K. (2000a). Particle image velocimetry. *Current Science-Bangalore*, 79(1):51–60.

Prasad, A. K. (2000b). Stereoscopic particle image velocimetry. *Experiments in fluids*, 29(2):103–116.

Raffel, M., Willert, C. E., Kompenhans, J., et al. (2007). *Particle image velocimetry: a practical guide*. Springer Science & Business Media.

Rashidi, M., Hetsroni, G., and Banerjee, S. (1990). Particle-turbulence interaction in a boundary layer. *International Journal of Multiphase Flow*, 16(6):935–949.

Sabban, L., Cohen, A., and van Hout, R. (2017). Temporally resolved measurements of heavy, rigid fibre translation and rotation in nearly homogeneous isotropic turbulence. *Journal of Fluid Mechanics*, 814:42–68.

Sabban, L. and van Hout, R. (2011). Measurements of pollen grain dispersal in still air and stationary, near homogeneous, isotropic turbulence. *Journal of Aerosol Science*, 42(12):867–882.

Scarano, F. (2012). Tomographic PIV: principles and practice. *Measurement Science and Technology*, 24(1):012001.

Schäfer, L. and Schröder, W. (2011). Comparison of holographic and tomographic particle-image velocimetry turbulent channel flow measurements. In *Journal of Physics: Conference Series*, volume 318, page 022019. IOP Publishing.

Schlichting, H., Gersten, K., Krause, E., and Oertel, H. (1955). *Boundary-layer theory*, volume 7. Springer.

Schneiders, J. (2017). Bridging piv spatial and temporal resolution using governing equations and development of the coaxial volumetric velocimeter. *Experiments in Fluids*.

Schroeder, A. and Willert, C. E. (2008). *Particle Image Velocimetry: new developments and recent applications*, volume 112. Springer Science & Business Media.

Shariati, M. R., Bibeau, E., Salcudean, M., and Gartshore, I. (2000). Numerical and experimental models of flow in the converging section of a headbox. In *TAPPI Papermakers Conference, Vancouver, Canada*.

Stitou, A. and Riethmuller, M. (2001). Extension of piv to super resolution using ptv. *Measurement Science and Technology*, 12(9):1398.

Subratachak (2018). *Positions of the sun, the earth and the moon*. `https://subratachak.wordpress.com/page/2/` [Accessed: 25.03.2018].

Sumer, B. M. and Oguz, B. (1978). Particle motions near the bottom in turbulent flow in an open channel. *Journal of Fluid Mechanics*, 86(1):109–127.

Tongpun, P., Bumrungthaichaichan, E., and Wattananusorn, S. (2014). Investigation of entrance length in circular and noncircular conduits by computational fluid dynamics simulation. *Songklanakarin Journal of Science and Technology*, 36(4):471–475.

Van Hout, R. (2011). Time-resolved piv measurements of the interaction of polystyrene beads with near-wall-coherent structures in a turbulent channel flow. *International Journal of Multiphase Flow*, 37(4):346–357.

Voth, G. A. and Soldati, A. (2017). Anisotropic particles in turbulence. *Annual Review of Fluid Mechanics*, 49:249–276.

Wernet, M. P. (2017). Comparison of Tomo-PIV versus dual plane PIV on a synthetic jet flow. *Nasa*.

Westerweel, J. (1997). Fundamentals of Digital Particle Image Velocimetry. *Measurement science and technology*, 8(12):1379.

Westerweel, J., Draad, A., Van der Hoeven, J. T., and Van Oord, J. (1996). Measurement of fully-developed turbulent pipe flow with digital particle image velocimetry. *Experiments in Fluids*, 20(3):165–177.

White, F. (1974). Viscous fluid flow, 640 pp.

Wibowo, O. A. (2016). *Foto Bokeh dan 4 Faktor Penting Membuat Foto Bokeh Berkualitas*. http://www.pricebook.co.id/article/tips_tricks/2016/02/09/3595/foto-bokeh-dan-4-faktor-penting-membuat-foto-bokeh-berkualitas [Accessed: 25.03.2018].

Yunus, A. C. and Cimbala, J. M. (2006). Fluid mechanics fundamentals and applications. *International Edition, McGraw Hill Publication*, 185201.